1 2025-04-16 19:48:45

TOWARDS ELECTRIC FIELD AND ATOM NUMBER UPGRADES FOR A HIGHER SENSITIVITY SEARCH FOR THE ATOMIC ELECTRIC DIPOLE MOMENT OF RADIUM-225

By

Gordon Arrowsmith-Kron

A DISSERTATION

Submitted to
Michigan State University
in partial fulfillment of the requirements
for the degree of

Physics — Doctor of Philosophy

2025

ABSTRACT

The discovery of a permanent non-zero Electric Dipole Moments (EDMs) would be a clean signature of a new source of Charge-Parity(CP) violation in the universe. Radium-225 is an ideal candidate for these searches, due to nuclear octopole deformation. Previous measurements of the EDM of the Radium-225 atom were able to achieve a sensitivity on the order of $10^{-23}\mathrm{e}\cdot\mathrm{cm}$. The next generation of this experiment aims to achieve sensitivity of $10^{-26}\mathrm{e}\cdot\mathrm{cm}$, which in the global picture would set new limits on various CP violating sources. Crucial to this sensitivity enhancement is an upgrade to the high voltage used to couple the EDM to an external E field. By achieving higher voltages with better understanding of reversibility, statistical sensitivity can be increased ans systematic uncertainty reduced. In addition, the Isotope Harvesting program at the Facility for Rare Isotope Beam (FRIB) will once again enable Radium-225 to be procured for the experiment. To ensure optimal harvesting efficiency, the study of various techniques to create a beam of atomic Radium will be necessary. For this reason, an atomic beam fluorescence apparatus has been built at FRIB.

ACKNOWLEDGMENTS

First and foremost, I would like to thank my advisor Jaideep Singh, who has patiently and helpfully guided me in my journey through graduate school. I would like to thank all the other graduate students I have worked with in Spinlab, including Aiden Boyer, Nicholas Nusgart, Karina Martirosova, Yousuf Alishan, Himanshi, Erin White, Roy Ready, and Ben Loseth. I would also like to thank everyone I worked with at Argonne National Laboratory, such as Kevin Bailey, Matt Dietrich, Thomas O'Connor, Peter Mueller, Donald Booth, Michael Bishof, and Tenzin Rabga. I would like to thank other friends of mine that I have had here at Michigan State University, such as Kellen McGee and Hank Thurston. Let me also take this time to thank my friends from home in New York City, such as Mark, Ness, Anik, Austin, Max Price, Max Drogin, and Josh. Finally, I would like to thank my incredibly supportive family, including Joan, Charley, Edmund, Billy, Anne, David, Richard, Deborah, Virginia, Steve, Jenny, and Charley Croft.

TABLE OF CONTENTS

LIST OF TABLES

LIST OF FIGURES

Chapter 1. Introduction

This thesis documents ongoing efforts to improve the sensitivity of the Radium-225 EDM experiment, to further constrain the upper limit of various sources of Charge-Parity (CP) violation. Radium-225 has an octopole deformation in its nucleus that gives it a large nuclear Schiff moment, enhancing its sensitivity to sources of CP violation. This experiment utilizes laser cooling and trapping to perform a spin precession measurement in the presence of a static electric field, which a non-zero atomic EDM would be able to couple to. By reversing the direction of the electric field and looking for a phase shift in the spin precession, an EDM can be searched for. Care must be taken to ensure these electric fields are perfectly reversible, to reduce systematic uncertainties. Also crucial to this experiment is a reliable, steady supply of Radium-225, which is a rare isotope with a half life of only 14 days. Previous sources, since the initial data runs ending in 2015, have shifted priorities away from fundamental symmetries measurements. The isotope harvesting program at FRIB will, once operational, make up for this shortfall. Questions remain, however, as to the efficiency with which an atomic beam can be created from isotopes harvested from the FRIB beam dump. The upgrades currently underway for the Radium EDM experiment include a new optical cycling scheme to laser cool and trap atoms, as well as plans to dress the excited states of the spin precession measurement to allow for a cleaner signal. In addition, higher electric fields with improved reversibility are planned, as well as studying the efficiency with which beams of atomic Radium can be created. The HV upgrade requires the design and construction of a new apparatus at Michigan State University (MSU) to facilitate higher voltages. It also requires atomic theory calculations to quantify the various systematic effects that arise in

atoms trapped in an Optical Dipole Trap (ODT). In addition, the beam efficiency studies requires an Atomic Beam Fluorescence (ABF) setup to be built at MSU, and then tested with laser spectroscopy of metallic Calcium to measure its sensitivity. This thesis is organized into 7 further chapters. Chapter 2 details the theory of CP violation and EDMs, and gives an overview on the reasons for measuring them, and what kinds of mediums can be used. Chapter 3 talks about the reasons for using Radium-225 specifically, and details the Radium EDM experiment overall. Chapter 4 reports on efforts to utilize Radium-223 as a temporary substitute. Chapter 5 details ongoing efforts to quantify the systematic effects that occur in EDM measurements done on atoms subject to static E fields that are held in an ODT. Chapter 6 describes the progress on upgrading the HV apparatus at MSU. Chapter 7 details the assembly and testing of the ABF apparatus to be used for efficiency studies. Chapter 8 overall describes the work done by the author, and details future work needed to be done.

Chapter 2. Background & Motivation

2.1 Baryon Asymmetry of Universe

2.1.1 Discovery of the Cosmic Microwave Background

One of the greatest measurements in human history was achieved essentially by accident. A.A. Penzias and R.W. Wilson, two radioastronomers, were trying to reduce the background noise seen from their radio telescope at the Crawford Hill Laboratory in Holmdel, New Jersey. This noise was "isotropic, unpolarized, and free from seasonal variations,"[7] and was significantly higher than what was expected from ohmic losses and atmospheric absorption. The paper they published was along side another paper [8] that interpreted the results from the noise as coming from Cosmic Microwave Background (CMB) radiation, which predicted a CMB temperature of 3.5 K. This measurement, which remarkably was able to make a measurement relating to the entire Universe from a single telescope, became the subject of much research. Interestingly, the CMB was found to be anisotropic - its background temperature changes slightly depending on place in the sky it is measured at. This change in temperature throughout the sky can be mapped, and used to discover things about the universe, such as the relative lack of antimatter compared to matter.

2.1.2 Baryon Asymmetry

The asymmetry between the matter and antimatter seen in the universe can be characterized by the predictably-named Baryon Asymmetry Parameter. This is given by

$$\eta = \frac{\eta_B - \eta_{\bar{B}}}{\eta_\gamma} \tag{2.1}$$

where η_B is the Baryon density, $\eta_{\bar{B}}$ is the Antibaryon density, and η_γ is the relic photon density. It can be experimentally determined from two sources.[9] The first is from Big Bang Nucleosynthesis (BBN). After the Big Bang, simple nuclei began to form as the universe cooled. η_B can be derived by measuring the abundances of these nuclei, such as ^{7}Li, or ^{3}He. Observed abundances of Deuterium give the most precise determination of η_B. This is because the only significant source of Deuterium in the universe that exists is that which is left over from the Big Bang, so no other deuterium has been created in stellar processes. The current deuterium mass fraction in BBN stands at $B/H|_p = (25.47 \pm 0.29) \times 10^{-6}$ which corresponds to a derived η value of

$$\eta = (6.040 \pm 0.118) \times 10^{-10} \tag{2.2}$$

There is another way of extracting the η parameter, however, coming directly from anisotropy in the CMB.

Based on measurements of the CMB, there is observed to be a baryon density parameter of $\Omega_b h^2 = .02237 \pm .00015$, which corresponds to a parameter of [10]

$$\eta = (6.104 \pm .058) \times 10^{-10} \tag{2.3}$$

which is well in agreement with the observation from BBN. This means that, having measured this parameter with two completely different types of observations, the observed baryon asymmetry parameter is well fixed, though observations in BBN with lithium remain

in tension with this value. The question remains of how this asymmetry came to be, and why there is something rather than nothing. Either the universe started out with an initial asymetry between matter and antimatter, or matter and antimatter were initially in equal amounts but the evolution of the universe overall favored matter over antimatter. This is known as Baryogenesis.

2.1.3 Sakharov Conditions

In 1967, Sakharov proposed three criteria necessary for Baryogenesis. The three conditions are the presence of:

1. Baryon number violating interactions
2. C and CP violating interactions
3. Interactions out of thermal equilibrium.

While the Standard Model does satisfy conditions one and three, it does not provide enough CP-violation to sufficiently explain the observed value of η.

2.1.4 Baryon Asymmetry predicted from CP violation

The observed CP-violation within the Standard Model can be generally represented by a phase in the Cabibbo-Kobayashi-Maskawa (CKM) matrix. The CKM matrix is a 3x3 matrix which describes the probability of weak interaction between different quark flavors. The 9 elements of the CKM matrix can be described by the sines and cosines of 3 mixing angles θ, and a CP-violating phase δ. Calculations can be done to predict the baryon asymmetry that results from this CP-violating phase of the CKM matrix. One such calculation [11] gives

Figure 2.1: Diagram of a Parity Transformation

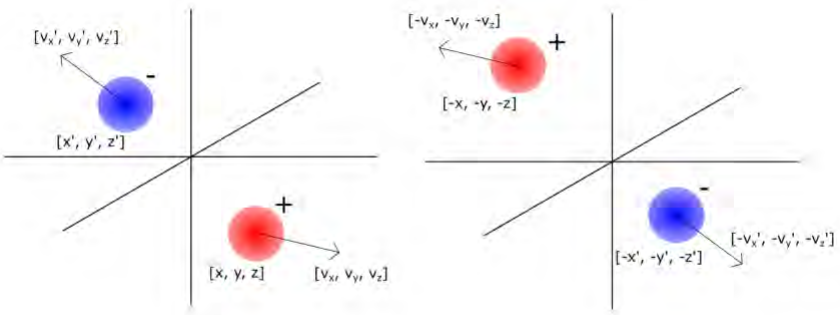

$$\eta \approx 10^{-27}$$

This means that there is a 17 order of magnitude difference between the observed η and the one predicted by current sources of CP violation. This implies there may be other sources of CP violation yet to be discovered. A brief overview of various symmetries shall now be given.

2.1.5 List of Discrete Symmetries

Physical parameters can be described by their behavior under discreet transformations. The three main transformations are now described.

2.1.5.1 Parity

A Parity transformation (P) is a spatial inversion. It occurs through the interchange of coordinates $[x, y, z] \rightarrow [-x, -y, -z]$, or in spherical coordinates $[r, \theta, \phi] \rightarrow [r, \pi - \theta, \phi + \pi]$

It was believed that the laws of physics remained the same under this transformation.

Figure 2.2: Diagram of a Charge Conjugation Transformation

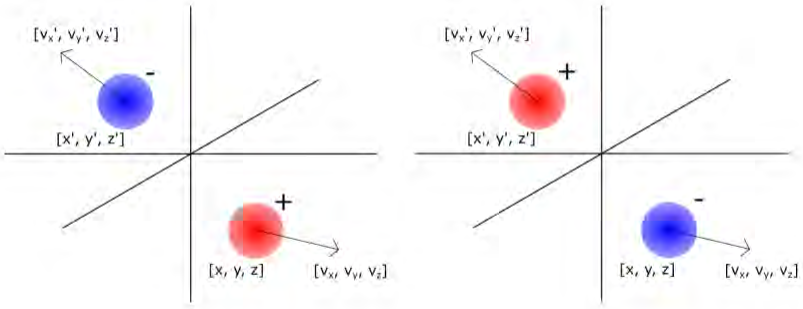

This was experimentally shown to be false by the Madame Wu experiment, which will be discussed in the next section.

2.1.5.2 Charge

A Charge conjugation (C) occurs when matter is exchanged for anti-matter. This causes charges to go like $Q \rightarrow -Q$, but it also affects other quantities, such as baryon number and lepton number.

2.1.5.3 Time

A time-reversal transformation (T) occurs when the arrow of time is reversed: $t \rightarrow -t$.

The behavior of various physical quantities under these transformations is given below. Note that "Even" indicates that a quantity remains the same, and "Odd" indicates that a quantity is inverted:

2.1.5.4 Charge Parity

A Charge-Parity transformation (CP) is the application of charge conjugation and parity transformation. After parity symmetry was shown to be broken in weak interactions, it was

Figure 2.3: Diagram of a Time Reversal Transformation

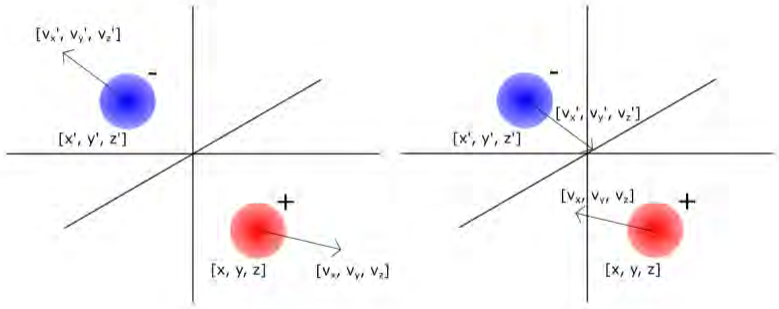

Table 2.1: Various Physical Quantities under Discreet Transformation

Quantity	C	P	T
Charge	Odd	Even	Even
Position	Even	Odd	Even
Time	Even	Even	Odd

believed that Charge-Parity symmetry was always conserved [12]. This was also shown to be false [13].

2.1.5.5 Charge Parity Time

A Charge-Parity-Time transformation (CPT) is the application of all three transformations. It is currently believed that it is always symmetric, though efforts are also ongoing in an attempt to find violations.

2.1.5.6 Lorentz Invariance

When doing calculations in special relativity, events can be presented as a contravariant 4-vector $a^\mu = [ct, x, y, z]$ or as a covariant 4-vector $b_\mu = g_{\mu\nu}b^\nu = [ct', -x', -y', -z']$. In this system, the value $a^\mu b_\mu = c^2tt' - xx' - yy' - zz'$ is invariant under transformation of

both vectors a and b by the Lorentz transformation. This is known as Lorentz invariance. Critically, du to this invariance, Lorentz scalars remain the same in all reference frames.

2.2 Violations of Discrete Symmetries

2.2.1 P violation

In 1956, T.D. Lee and C.N.Yang [14] called into question whether the weak interaction did indeed preserve parity, as had been presumed. This question resulted in a famous experiment conducted by C.S. Wu and her collaborators at the National Bureau of Standards [15]. In this experiment, a ^{60}Co beta decay source was polarized, and the beta decay angular distribution measured twice, at two different anti-parallel polarization directions. Gamma radiation was used to monitor the degree of polarization. A clear asymmetry was seen between the two polarizations, cleanly showing a non-conservation of P-symmetry. Afterwards, an experiment measuring the polarization of muons decayed from pions was done by measuring the electron distribution from the muon decay[16].From here, Landau [12] proposed that space could remain isotropic even with parity non-conservation, so long as CP-symmetry held. It was then thought that CP-symmetry was conserved in weak interactions as well.

2.2.2 CP violation

An experiment studying the decay of Kaons in 1964 [13] revealed a decay path which is only possible through CP violation. This showed that CP symmetry is not a conserved quantity in the Universe, though it is only violated in the weak interaction as far as is currently known. CPT symmetry is still assumed to be conserved, as no violation has yet been found.

A signature of T violation is thus a signature of CP violation as well.

2.3 Electric Dipole Moments as Signatures of New Physics

Sources of CP violation can be looked for in a variety of ways. One very clean signature of CP violation is the existence of an Electric dipole Moment, or EDM.

2.3.1 Definition of EDM

When looking at a distribution of charges from far away, it becomes convenient to write their distribution in a multipole expansion. This is done by writing their voltage V in a form like

$$V(\mathbf{r}) = V_{\text{mon}}(\mathbf{r}) + V_{\text{dip}}(\mathbf{r}) + V_{\text{quad}}(\mathbf{r}) + ... \tag{2.4}$$

where the dependence on $r = \|\mathbf{r}\|$ goes like:

$$V(\mathbf{r}) = \frac{1}{r} f_{\text{mon}}(\theta, \phi) + \frac{1}{r^2} f_{\text{dip}}(\theta, \phi) + \frac{1}{r^3} f_{\text{quad}}(\theta, \phi) \tag{2.5}$$

The function $V_{\text{mon}}(\mathbf{r})$ is the monopole moment, and is simply

$$V_{\text{mon}}(\mathbf{r}) = \frac{1}{r} \frac{1}{4\pi\epsilon_0} \int_{V'} \rho(r') dV' = \frac{Q_{total}}{4\pi\epsilon_0 r} \tag{2.6}$$

which is just the potential given by a point charge, whose charge is equal to the total of the charge distribution.

The next term to come is given by

$$V_{\text{dip}}(\mathbf{r}) = \frac{\hat{\mathbf{r}}}{4\pi\epsilon_0 r^2} \cdot \int_{V'} \rho(r')\mathbf{r}' dV' \tag{2.7}$$

The quantity

$$\mathbf{d} = \int_{V'} \rho(r')\mathbf{r}' dV' \tag{2.8}$$

is known as the "Electric Dipole Moment," or EDM. As can be seen, the strength of the potential of the EDM vanishes faster as $\|\mathbf{r}\| \to \text{inf}$ than the monopole moment, but slower than higher order approximations, such as the quadrupole or octupole moments. EDMS are useful for fundamental symmetry searches, as they are a very clean signature of CP violation.

2.3.2 Why do EDMs Violate Symmetry

The existence of a non-zero permanent EDM is a signature of CP violation, as can be seen through the Wigner-Eckart theorem. The energy interaction due to the interaction between a non-zero Electric and Magnetic dipole moment and an external E and B field is

$$H = -\mu \cdot \mathbf{B} - \mathbf{d} \cdot \mathbf{E} \tag{2.9}$$

The Wigner-Eckart theorem tells us that μ and $\mathbf{d}$ must be parallel to the spin. Thus,

$$H = -\mu \left(\frac{\mathbf{S} \cdot \mathbf{B}}{|\mathbf{S}|} \right) - d \left(\frac{\mathbf{S} \cdot \mathbf{E}}{|\mathbf{S}|} \right) \tag{2.10}$$

Now, look at the symmetries of each component:

Under a T transformation of the Hamiltonian, it becomes

Table 2.2: Transformations of Relevant Quantities

Value	P Transformation	C Transformation	T Transformation
$\mathbf{S}$	Even	Even	Odd
$\mathbf{E}$	Odd	Odd	Even
$\mathbf{B}$	Even	Odd	Odd
$\mathbf{S} \cdot \mathbf{B}$	Even	Odd	Even
$\mathbf{S} \cdot \mathbf{E}$	Odd	Odd	Odd

$$H = -\mu \left(\frac{\mathbf{S} \cdot \mathbf{B}}{|\mathbf{S}|} \right) + d \left(\frac{\mathbf{S} \cdot \mathbf{E}}{|\mathbf{S}|} \right) \tag{2.11}$$

So, while the magnetic term remains the same, the electric term changes signs. This means that, should $d \neq 0$, the Hamiltonian will be different under T transformation. Through the CPT symmetry, this implies CP violation as well.

2.3.3 Definition of Nuclear Schiff Moment

According to the Schiff Theorem[17], when approximating a nucleus as a point particle, and assuming non-relativistic motion, a non-zero nuclear EDM will cause a screening effect in the surrounding electrons that completely screens the nuclear EDM. However, the nucleus also has what is called a Schiff moment, and this will induce an atomic EDM in the surrounding atom. An excellent derivation of this can be given by [18] and [19]:

Consider an electrostatic potential of the form

$$\phi(\mathbf{R}) = \int \frac{e\rho(\mathbf{r})}{|\mathbf{R} - \mathbf{r}|} d^3r + \frac{1}{Z}(\mathbf{d} \cdot \nabla) \int \frac{\rho(\mathbf{r})}{|\mathbf{R} - \mathbf{r}|} d^3r \tag{2.12}$$

This potential represents the nuclear electrostatic potential with the effects of electron screening included. Here, $e\rho(\mathbf{r})$ is the nuclear charge density, and $d = e \int \rho(\mathbf{r}) \mathbf{r} d^3r$ is the

nuclear EDM.

The quantity $\frac{1}{|\mathbf{R}-\mathbf{r}|}$ can be expanded like

$$\frac{1}{|\mathbf{R}-\mathbf{r}|} = \sum_l \frac{r_<^l}{r_>^{l+1}} P_l(\cos(\theta)) \tag{2.13}$$

where P_l are the Legendre polynomials, θ is the angle between $\mathbf{r}$ and $\mathbf{R}$, and $r_<$ and $r_>$ correspond to the minimum and maximum of the quantities $\mathbf{R}$, $\mathbf{r}$ respectively. The first P and T violating expansion terms from each term in the original potential are:

$$\phi^{(1)}(\mathbf{R}) = e \int \frac{\rho(\mathbf{r}) r_<}{r_>^2} \cos(\theta) + \frac{1}{Z}(\mathbf{d}\cdot\nabla) \int \frac{\rho(\mathbf{r})}{r_>} d^3r \tag{2.14}$$

which corresponds to the l = 1 expansion of the first term, and the l = 0 expansion of the second term. This can then be simplified to

$$\phi^{(1)}(\mathbf{R}) = \frac{e}{R^2}\int_0^R \rho(\mathbf{r}) r\cos(\theta) d^3r + eR\int_R^\infty \frac{\rho(\mathbf{r})\cos(\theta)}{r^2} d^3r + \frac{\mathbf{d}\cdot\hat{\mathbf{r}}}{ZR^2}\int_0^R \rho(\mathbf{r}) d^3r \tag{2.15}$$

and then be written as

$$\phi^{(1)}(\mathbf{R}) = \frac{e\mathbf{R}}{R^3}\cdot\int_0^R \mathbf{r}\rho(\mathbf{r}) d^3r + e\mathbf{R}\cdot\int_R^\infty \frac{\mathbf{r}}{r^3}\rho(\mathbf{r}) d^3r - \frac{e\langle\mathbf{r}\rangle\cdot R}{ZR^3}\int_0^R \rho(\mathbf{r}) d^3r \tag{2.16}$$

Now consider the case where $\mathbf{R}\to\infty$. The first term becomes

$$\frac{e\mathbf{R}}{R^3}\cdot\int_0^\infty \mathbf{r}\rho(\mathbf{r}) d^3r = \frac{e\mathbf{R}\cdot\langle\mathbf{r}\rangle}{R^3} \tag{2.17}$$

and the third term becomes

$$\frac{e\langle \mathbf{r} \rangle \cdot R}{ZR^3} \int_0^\infty \rho(\mathbf{r}) d^3r = \frac{Ze\langle \mathbf{r} \rangle \cdot \mathbf{R}}{ZR^3} = \frac{e\langle \mathbf{r} \rangle \cdot \mathbf{R}}{R^3} \tag{2.18}$$

So these terms cancel.

Thus,

$$\frac{e\mathbf{R}}{R^3} \cdot \int_0^R \mathbf{r}\rho(\mathbf{r}) d^3r - \frac{e\langle \mathbf{r} \rangle \cdot R}{ZR^3} \int_0^R \rho(\mathbf{r}) d^3r = \frac{e\mathbf{R}}{R^3} \cdot \int_0^R \mathbf{r}\rho(\mathbf{r}) d^3r - \frac{e\langle \mathbf{r} \rangle \cdot R}{ZR^3} \int_0^R \rho(\mathbf{r}) d^3r + 0$$

$$= \frac{e\mathbf{R}}{R^3} \cdot \int_0^R \mathbf{r}\rho(\mathbf{r}) d^3r - \frac{e\langle \mathbf{r} \rangle \cdot R}{ZR^3} \int_0^R \rho(\mathbf{r}) d^3r + \frac{e\langle \mathbf{r} \rangle \cdot R}{ZR^3} \int_0^\infty \rho(\mathbf{r}) d^3r - \frac{e\mathbf{R}}{R^3} \cdot \int_0^\infty \mathbf{r}\rho(\mathbf{r}) d^3r$$

$$= -\left(\frac{e\mathbf{R}}{R^3} \cdot \int_0^\infty \mathbf{r}\rho(\mathbf{r}) d^3r - \frac{e\mathbf{R}}{R^3} \cdot \int_0^R \mathbf{r}\rho(\mathbf{r}) d^3r \right) + \left(\frac{e\langle \mathbf{r} \rangle \cdot R}{ZR^3} \int_0^\infty \rho(\mathbf{r}) d^3r - \frac{e\langle \mathbf{r} \rangle \cdot R}{ZR^3} \int_0^R \rho(\mathbf{r}) d^3r \right)$$

$$= -\frac{e\mathbf{R}}{R^3} \cdot \int_R^\infty \mathbf{r}\rho(\mathbf{r}) d^3r + \frac{e\langle \mathbf{r} \rangle \cdot R}{ZR^3} \int_R^\infty \rho(\mathbf{r}) d^3r \tag{2.19}$$

So, the potential can be written as:

$$\phi^{(1)}(\mathbf{R}) = e\mathbf{R} \cdot \left[\int_R^\infty \left(\frac{\langle \mathbf{r} \rangle}{ZR^3} - \frac{\mathbf{r}}{R^3} + \frac{\mathbf{r}}{r^3} \right) \rho(\mathbf{r}) d^3r \right] \tag{2.20}$$

From here, consider a generic wavefunction of an electron:

$$\psi = \begin{bmatrix} f(R) \\ -i(\sigma \cdot \hat{\mathbf{R}})g(R) \end{bmatrix} \Omega_{jlm} = h(R)\Omega_{jlm} \tag{2.21}$$

where f(R) and g(R) are radially dependent functions, and Ω_{jlm} is a spherical spinor. The potential $\phi^{(1)}(\mathbf{R})$ is both odd in parity, and close to the nucleus. The only orbital wavefunctions that have a significant presence near the nucleus are l = 0 and 1. Since this potential is odd in parity, the only relevant matrix element to resolve is that between s and p:

$$\langle s| - e\phi^{(1)}(\mathbf{R})|p\rangle$$

When wrote out in length, this looks like:

$$\langle s| - e\phi^{(1)}(\mathbf{R})|p\rangle$$

$$= -e^2 \int_0^\infty \int_0^{2\pi} \int_0^\pi \psi_s^\dagger \mathbf{R} \cdot \left[\int_R^\infty \left(\frac{\langle \mathbf{r} \rangle}{ZR^3} - \frac{\mathbf{r}}{R^3} + \frac{\mathbf{r}}{r^3} \right) \rho(\mathbf{r}) d^3r \right] \psi_p R^2 \cos(\theta_R) d\theta_R d\phi_R dR$$

$$= -e^2 \int_0^\infty \int_0^{2\pi} \int_0^\pi \psi_s^\dagger \frac{\mathbf{R}}{R} \cdot \left[\int_R^\infty \left(\frac{\langle \mathbf{r} \rangle}{Z} - \mathbf{r} + \frac{R^3 \mathbf{r}}{r^3} \right) \rho(\mathbf{r}) d^3r \right] \psi_p \cos(\theta_R) d\theta_R d\phi_R dR$$

$$= -e^2 \int_0^{2\pi} \int_0^\pi \Omega_s^\dagger \hat{\mathbf{R}} \Omega_p \cos(\theta_R) d\theta_R d\phi_R \cdot \int_0^\infty \int_R^\infty h_s^\dagger(R) \left(\frac{\langle \mathbf{r} \rangle}{Z} - \mathbf{r} + \frac{R^3}{r^3} \mathbf{r} \right) \rho(\mathbf{r}) h_p(R) d^3r dR \tag{2.22}$$

Now, define

$$U_{sp} = h_s^\dagger(R) h_p(R) = f_s(R) f_p(R) + g_s(R) g_p(R) \tag{2.23}$$

and

$$\langle s|\hat{\mathbf{R}}|p\rangle = \int_0^{2\pi} \int_0^{\pi} \Omega_s^\dagger \hat{\mathbf{R}} \Omega_p \sin(\theta_R) d\theta_R d\phi_R \tag{2.24}$$

Then, this can be written as

$$\begin{aligned}
\langle s| - e\phi^{(1)}(\mathbf{R})|p\rangle &= -e^2 \langle s|\hat{\mathbf{R}}|p\rangle \cdot \int_0^\infty \int_R^\infty h_s^\dagger(R) \left(\frac{\langle \mathbf{r} \rangle}{Z} - \mathbf{r} + \frac{R^3}{r^3}\mathbf{r} \right) \rho(\mathbf{r}) h_p(R) d^3 r dR \\
&= -e^2 \langle s|\hat{\mathbf{R}}|p\rangle \cdot \int_0^\infty \int_0^r h_s^\dagger(R) \left(\frac{\langle \mathbf{r} \rangle}{Z} - \mathbf{r} + \frac{R^3}{r^3}\mathbf{r} \right) \rho(\mathbf{r}) h_p(R) dR d^3 r \\
&= -e^2 \langle s|\hat{\mathbf{R}}|p\rangle \cdot \int_0^\infty \left[\left(\frac{\langle \mathbf{r} \rangle}{Z} - \mathbf{r} \right) \int_0^r U_{sp}(R) dR + \frac{\mathbf{r}}{r^3} \int_0^r U_{sp}(R) R^3 dR \right] \rho(\mathbf{r}) d^3 r
\end{aligned} \tag{2.25}$$

The quantity $U_{sp}(R)$ can be expressed as

$$U_{sp}(R) = \sum_{k=1}^{\infty} b_k R^k \tag{2.26}$$

Plugging this in, this gives

$$\langle s| - e\phi^{(1)}(\mathbf{R})|p\rangle = -e^2 \langle s|\hat{\mathbf{R}}|p\rangle \cdot \sum_{k=1}^{\infty} \frac{b_k}{k+1} \left[\frac{\langle \mathbf{r} \rangle}{Z} \langle r^{k+1} \rangle - \frac{3}{k+4} \langle \mathbf{r} r^{k+1} \rangle \right] \tag{2.27}$$

When considering only k = 1, this equation becomes

$$\langle s| - e\phi^{(1)}|p\rangle = -\frac{e^2 b_1}{2}\langle s|\hat{\mathbf{R}}|p\rangle \cdot \left[\frac{1}{Z}\langle \mathbf{r}\rangle\langle r^2\rangle - \frac{3}{5}\langle \mathbf{r}r^2\rangle\right] \tag{2.28}$$

This can then be written as

$$\langle s| - e\phi^{(1)}|p\rangle = 4\pi e\mathbf{S}\cdot(\nabla\psi_s^\dagger\psi_p)_{R\to 0} \tag{2.29}$$

where

$$\mathbf{S} = \frac{e}{10}\left[\langle r^2\mathbf{r}\rangle - \frac{5}{3Z}\langle r^2\rangle\langle \mathbf{r}\rangle\right] = S\frac{\mathbf{I}}{I} \tag{2.30}$$

is known as the Schiff moment. Note that this divides the potential into two sections: The Schiff moment, which is nuclear dependent, and the electronic wavefunctions ψ_s and ψ_p, which are electron dependent. This quantity is capable of coupling states of different parity, much like the electric dipole transition coupling necessary for an atomic EDM to be induced. Thus, an atomic EDM can be written in the expression:

$$\mathbf{d}_{atom} = -2e\sum_k \frac{\langle i|\mathbf{r}|k\rangle\langle k| - e\phi^{(1)}|i\rangle}{E_i - E_k} = -2e\sum_k \frac{\langle i|\mathbf{r}|k\rangle 4\pi\mathbf{S}\cdot(\nabla\psi_k^\dagger\psi_i)_{R\to 0}}{E_i - E_k} \tag{2.31}$$

Now, $\nabla\psi_k^\dagger\psi_i$ can be approximated

$$\nabla\psi_k^\dagger\psi_i \approx Z^2\alpha^2 \tag{2.32}$$

where α is the fine structure constant, and Z is the proton count. It can now be written

$$\mathbf{d}_{atom} = -2e \sum_k \frac{\langle i|\mathbf{r}|k\rangle 4\pi S Z^2 \alpha^2}{E_i - E_k} \tag{2.33}$$

This gives an enhancement factor to EDM searches for heavy nuclei, since the sensitivity goes like Z^2. For octupole deformed nuclei, there is an additional enhancement factor intrinsic to the Schiff moment, which will be discussed later.

2.4 State of the Art in Hadronic CP Violation

Precision EDM searches in different types of systems probe different sectors from which new physics might arise. The most precise atomic EDM search constraining new physics in the hadronic sector is the measurement of Hg-199. This experiment gives an upper limit 95% confidence interval of d_{Hg} at [1]

$$d_{Hg} < 7.4 \times 10^{-30} e \cdot cm$$

The experiment consisted of two vapor cells of Hg-199, with a charged plate in between the gas cells, creating an electric field of equal strength in each of the cells, but in opposite directions.

A magnetic field is also applied to the cells, to cause the Larmor precession for the phase shift measurement. More detail on the precise workings of an EDM experiment will be given later. Because the vapor cells use the same electrode plate, and the spin precession frequency is done at the same time, there is a great reduction in the uncertainty due to magnetic field instability. This gives the experiment a great deal of precision. However, the Hg-199 atom does not have an octupole deformation, and its leading systematic is due to

Figure 2.4: Diagram of the Hg-199 EDM Experimental Setup. a): A Cross Section View of the Vapor Cells. b): A Cross Section View of the Apparatus as a Whole. Taken from [1]

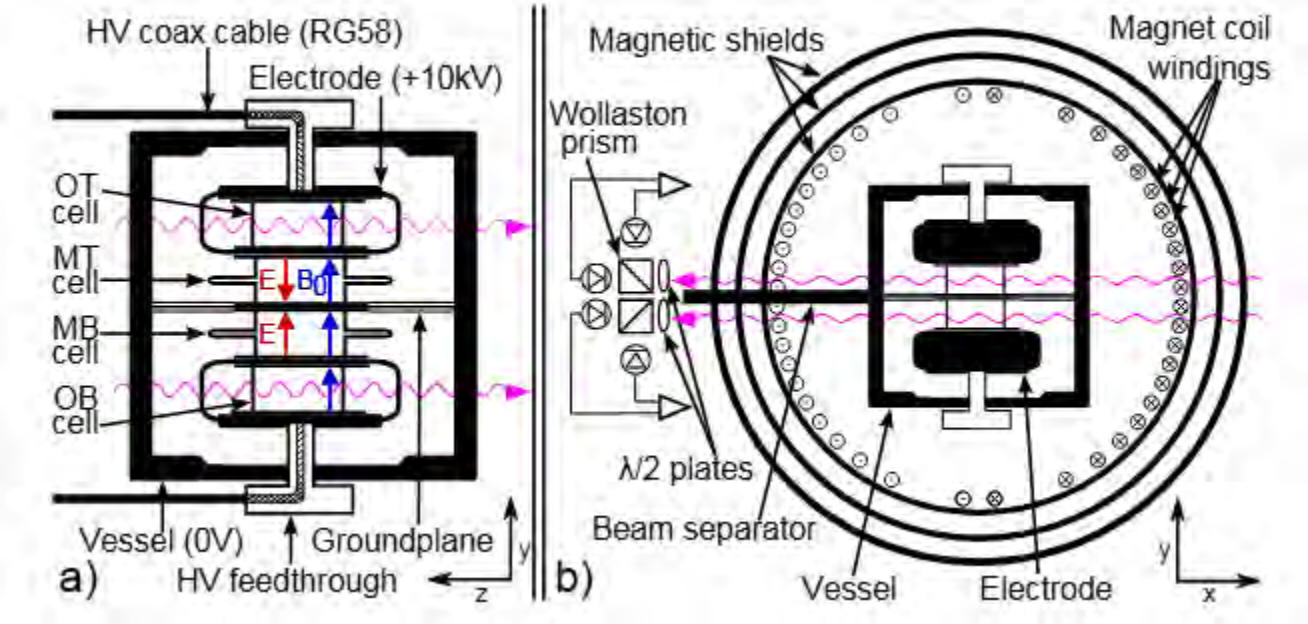

a magnetic field gradient in the axial direction of its vapor cells, which is seen due to the motion of the particles. With any shift in position of the cells due to HV, this would create a false EDM signature. The experiment ran with 4 different configurations, with the B field running in either direction, and the E field both parallel and antiparallel to the B field in order to characterize this systematic effect. This would come to be understood to be the dominant systematic effect, which is difficult to reduce. This experiment, though 30 years old and remarkable in its sensitivity, is likely reaching the maximum of its potential.

2.4.1 Connection between EDMs and new physics

By performing EDM searches on a wide variety of systems, different sectors of physics where CP violation can arise are probed. Diamagnetic systems, such as Hg-199, Ra-225, or Xe-129, probe spin dependent electron-nucleus coupling, as well as nucleon-nucleon interactions.

Table 2.3: Current Best Limits on CP Violating Sources

Parameter	Best Sensitivity	Source
d_e	¡ 2.1×10^{-29}e · cm (global)	[21], [22]
C_S	¡ 1.9×10^{-9} (global)	[21], [22]
C_T	1.2×10^{-7} (single source)	[1]
g_π^0	2.3×10^{-12} (single source)	[1]
g_π^1	1.2×10^{-12} (single source)	[1]
d_p	2.0×10^{-25}e · cm (single source)	[1]
d_n	¡ 1.8×10^{-26}e · cm (single source)	[23]

Paramagnetic systems, such as Fr or Cs, on the other hand, look for nuclear spin independent electron-nucleus coupling, as well as for the electron EDM. An EDM can be expressed as linear combination of CP violating factors from various sources [20]:

$$d_{atom} = \alpha_{d_e} d_e + \alpha_{C_S} C_s + \alpha_{C_T} C_T + \alpha_{d_n} d_n + \alpha_{d_p} d_p + \alpha_{g_\pi^0} g_\pi^0 + \alpha_{g_\pi^1} g_\pi^1 \tag{2.34}$$

where d_e is the electron EDM, C_S is a CP violating spin-independent electron-nucleus interaction, C_T is a spin-dependent electron-nucleus interaction, g_π^0 and g_π^1 are pion-nucleon couplings for isospin 0 and 1, d_p is the proton EDM, and d_n is the neutron EDM. The parameters α_{d_e}, α_{C_S}, α_{C_T}, $\alpha_{g_\pi^0}$, $\alpha_{g_\pi^1}$, α_{d_p}, and α_{d_n} are various coupling constants that can be determined by nuclear, molecular, or atomic structure calculations.

2.5 Current Status of Other EDM searches

At the moment, there are multiple experiments searching for new physics by trying to find new sources of CP violation. Among these are EDM searches, searching for non-zero signatures in a variety of systems, such as quarks, nuclei, atoms, and molecules.

2.5.1 Neutron EDM searches

There is a world wide effort to search for the EDM of the neutron. For example, at Los Alamos, there is an EDM experiment being performed on ultracold neutrons (UCN) known as the nEDM experiment. The purpose of this experiment is to measure the EDM of the neutron to a target precision of $d_n \leq 2 \times 10^{-27} e \cdot cm$ after 5 years of running. The experiment uses a typical EDM measurement cycle: load the neutrons into a trap, let the neutrons precess under an E field, and then measure the spin direction of the neutrons in their final state, looking for any change in phase shift under a reversal of the E field. Tests have been performed measuring the count rate of neutrons under different neutron holding times, and different applied magnetic fields. They can have a UCN yield of 60,000 neutrons with a 180s holding time, which should be sufficient to achieve their precision target in the allotted time [24]. Currently, the best nEDM measurement sits at $|d_n| \leq 1.8 \times 10^{-26} e \cdot cm$ performed by the PSI facility center for Muon and Neutron Sciences [23]. This experiment utilized the PSI UCN source to provide neutrons into a spin precession chamber, with a spin flipper able to choose the direction of spin for the incoming neutrons. The neutrons precess in the chamber for 180 seconds, with an applied E field of 11 kV/cm. They are then let out of the chamber, an fall a system of two neutron detectors each with a spin flipper, one of which will be on. The neutron detectors then count the number of spin up and spin down neutrons, and measure the asymmetry between them. An average of 11400 neutrons were counted per cycle.

Figure 2.5: Diagram of the nEDM Setup at PSI

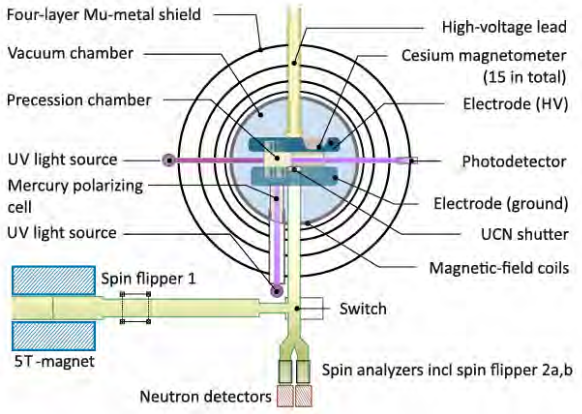

2.5.2 Electron EDM searches

Electron EDMs are searched for in Paramagnetic atoms and molecules. The ACME experiment at Harvard used a beam of ThO to measure the EDM of the electron, and set a limit of

$$d_e < 1.1 \times 10^{-29} e \cdot cm$$

.

in 2018 [22]. This experiment was performed on a moving beam of atoms, which were polarized, and allowed to precess over a length of 20 cm, or 1 ms. Then, the orientation of spin was read out by measuring the intensity of scattered light from an excited transition dependent on the spin orientation. The electric field applied was either 80 or 140 V/cm, and the experiment was run over 350 hours. The leading systematic error proved to be imperfections in electric field reversibility.

Another experiment was done in 2022 on HfF ions[21]. In this experiment, HfF is created and formed into a beam, where it is ionized and then trapped, and an EDM experiment

performed on it. The result was a 90% confidence interval upper bound of

$$d_e < 4.1 \times 10^{-30} e \cdot cm$$

which is in agreement with the ThO result.

2.5.3 Yb-171 and Ra-225

In China, an EDM experiment has been performed on Yb-171, yielding a result with a 95% confidence interval at

$$d_{Yb_{171}} < 1.5 \times 10^{-26} e \cdot cm$$

This experiment was nearly identical to the Radium-225 experiment with the limit at

$$d_{Ra_{225}} < 1.4 \times 10^{-23} \mathrm{e} \cdot \mathrm{cm}$$

When considering the enhancement factor in Ra-225 due to its octopole deformation, both of these experiments set roughly the same limit on sensitivity to new physics. The Yb-171 experiment utilizes a novel Quantum-Non-Demolition technique [25], that dresses the excited states used for the shadow imaging that is done to perform the final spin measurement. With this technique, they were able to achieve a spin detection efficiency of 50%, far above what the most recent run of the RaEDM experiment was able to achieve [26]. This upgrade is readily applicable for use in the RaEDM experiment, and work is being done to implement it into the next data run. More information on the Radium-225 experiment is in a later chapter.

2.5.4 Xe-129

An experiment searching for the EDM of the Xe-129 atom was done, giving it a limit at $\|d_A(Xe-129)\| < 8.3 \times 10^{-28} e \cdot cm$. This experiment utilizes a He-3 co-magnetometer, whose spin precession is measured simultaneously, and used to give a precise measurement of the B field where the atoms are trapped. This is technique is hoped to be used one day in the RaEDM experiment, as well as the Yb-171 experiment [27].

2.5.5 Tl-205

In 1991, an experiment was performed on the ^{205}TlF molecule to try to find its Nuclear Schiff Moment. This experiment used a jet source of the atoms, which passed through an E field. The experiment yielded a measurement of the molecular EDM of ^{205}TlF at $(-1.7 \pm 2.9) \times 10^{-23} e \cdot cm$[28]. At the Cold molecule Nuclear Time-Reversal EXperiment (CeNTREX) underway at Argonne National Laboratory, efforts are underway to perform an experiment on TlF again [29], first with a beam experiment, and then utilizing laser cooling and trapping. The experiment seeks to measure a CP violating energy shift with a sensitivity of 45 nHz.

2.5.6 Nuclear Magnetic Quadrupole Moments

Other CP-violating moments for nuclei exist. In addition to the Electric Dipole Moment, the Magnetic Quadrupole Moment also violates T and CP symmetry. It is the magnetic analogue to the electric quadropole moment; in that the magnetic field of a localized current can be approximated from far away as the sum of magnetic dipole, quadrupole, etc. moments. A proposed experiment [30] plans to measure the nuclear Magnetic Quadupole Moment in

^{173}Yb in an optical latice. It hopes to achieve a sensitivity of $\delta M \leq 3.7 \times 10^{-8} \mu_N fm$

2.5.7 Note about molecules

Molecules have a large internal field, which gives a great enhancement in the effective electric field for a small electric field applied. This gives them an advantage over single atoms, as can be seen in such experiments as CeNTREX or ACME, which only needed an applied electric field on the order of E $100V/cm$, 3 orders of magnitude less than the fields needed for the $Ra-225$ experiment. In Thorium Oxide, for instance, an applied electric field of 10 V/cm provides an effective E field for the electron EDM of 80 GV/cm[31].Different types of experiments are being proposed, such as experiments with atomic beams, laser cooled and trapped molecules, and molecules implanted in solids. The main issue with such experiments comes from the fact that laser cooling and trapping molecules is very difficult, since the additional vibrational and rotational states in molecules makes the optical cycling scheme needed for laser cooling very complex.

Chapter 3. The Radium EDM Laser Trap Experiment

The Radium-225 EDM experiment ongoing at ANL and MSU aims to improve the sensitivity to CP violating factors in the hadronic sector in its next sensitivity upgrade. Even a single order of magnitude improvement of sensitivity would set new CP violation source limits in the global picture. Radium-225 is an idea isotope for this, due to its octopole deformation.

3.1 Octopole Deformed Nuclei

A nucleus is defined by the number of protons and neutrons it has. For certain nuclei, sponteanteous symmetry breaking results in a distortion of the overall shape of the nucleus from being spherically symmetric. Of particular interest are octopole deformed nuclei, which can be described as "pear shaped"[32]. This gives its shape an asymmetry under parity, giving it both a large nuclear schiff moment and small parity doublet.

3.1.1 Definition of Octopole Deformation

The general shape of an axially symmetric nucleus, and its deformation from being a perfect sphere, can be put in terms of spherical harmonics[33]:

$$R(\theta, \phi) = R_0(1 + \sum_{\lambda=2} \beta_\lambda Y_{\lambda 0}(\theta, \phi))$$

where $Y_{\lambda\mu}$ are the spherical harmonics and β_λ are various coefficients used to describe

Figure 3.1: Diagram of Various Nuclear Deformations. Taken from [2]

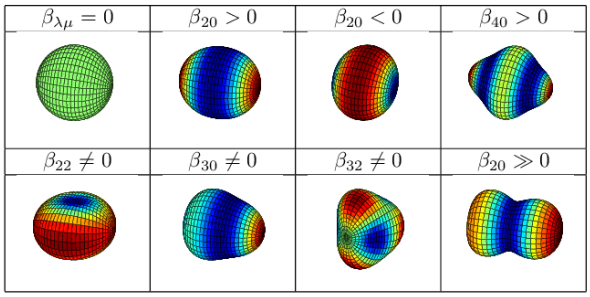

the nuclear distribution. The first non-zero moments start with $\lambda = 2$, which indicates a quadrupole deformation. Octopole deformations are the deformations associated with $\lambda = 3$.

3.1.2 Enhanced Sensitivity to Symmetry Violation

The Schiff moment for a nucleus can be described by

$$S = \langle \Psi_0 | \hat{S}_z | \Psi_0 \rangle = \sum_{i \neq 0} \frac{\langle \Psi_0 | \hat{S}_z | \Psi_i \rangle \langle \Psi_i | \hat{V_{PT}} | \Psi_0 \rangle}{E_0 - E_i}$$

where S is the lab frame Schiff moment, $\langle \Psi_0 | \hat{S}_z | \Psi_i \rangle$ is the intrinsic Schiff moment using nuclear wavefunctions, and $\langle \Psi_i | \hat{V_{PT}} | \Psi_0 \rangle$ is a time and parity violating matrix element where new physics occurs. An octopole deformed nucleus has a parity doublet in its ground state, due to its shape. This means, for an octopole deformed nuclues, there is a term in this sum with a relatively small denominator in the form of $E_0 - E_i$. Furthermore, the octopole deformation gives an enhancement factor for the value of this $\langle \Psi_0 | \hat{S}_z | \Psi_i \rangle$ as well. Thus, for a given measured value of S, there is a higher sensitivity to the time violating parameter $\hat{V_{PT}}$.

Table 3.1: Theoretically Calculated Coefficients for Schiff Moment Dependnce on Nucleon-Pion Interactions, $S = a_0 g\bar{g}_0 + a_1 g\bar{g}_1$

Element	a_0 (e ·fm^3) (SIII)	a_0 (e ·fm^3) (SLy4)	a_1 (e ·fm^3) (SIII)	a_1 (e ·fm^3) (SLy4)	Source
Ra-225	-1.0	-3.0	7.0	16.9	[34]
Hg-199	.012	.013	.005	-.006	[35]

3.1.3 Candidate Isotopes

Nuclei with odd nuclear spin and an octopole deformation in their nucleus have a ladder of nearly degenerate parity doublet nuclear states. This makes atoms such as Radium-225 very good candidates for EDM experiments, since they have an enhancement in sensitivity to CP violating physics over atoms like Hg-199. Radium 225's status as a rare isotope, due to its mere 14 week half life, unfortunately makes it difficult to measure. Another such candidate nucleus is Pa-229. This isotope may or may not have a parity doublet with an even smaller energy difference - possibly on the order of 10s of eV, as opposed to the Ra-225 55 keV parity doublet. This would give a further enhancement factor to any EDM measurement performed upon it - but its so small it may not even exist, and its half life is only a few days. Experiments are ongoing to determine whether or not it even has this doublet.

Table 3.2: Candidate Isotopes and Sensitivities

Nucleus	$\Delta E(keV)$	$\tau_{1/2}(s)$	Sensitivity	Source
Hg-199	1800	stable	1	[1]
Rn-223	10^2?	10^3	10^2	-
Ra-225	55	10^6	10^3	[36]
Pa-229	$(.06 \pm .05)$?	10^5	10^6	-

3.2 EDM experiments in laser traps

Performing experiments on atoms that are trapped using laser beams has advantages over performing experiments in a vapor cell. Radium has a vapor pressure that is too low to be used in a Vapor Cell, and its 14 day half life poses a significant challenge. For Hg-199, however, a vapor cell is possible, and carries with it the advantage of being able to measure many more atoms in total.

3.2.1 Comparison to Vapor Cells

In a vapor cell, since atoms are moving as a gas, they have a significantly higher velocity than those in a laser trap. In addition, the atoms fill out a much larger volume, at around 5 cm^3, so there can be a spatial variation in the magnetic and electric fields. This spatial variation in the magnetic field is especially important for the Hg-199 experiment[1], as it contributes the most to the systematic uncertainty.

With a laser trap, the atoms are moving much slower, and in a much smaller volume. This means that the atoms have less uncertainty with the spacial variation of the B and E field, and are moving much slower. However, there are drawbacks. Since only laser cooled and trapped atoms can be used, there are are great deal fewer atoms that can be measured at one time. Also, the experimental setup at Argonne can only measure a single configuration at a time - with either the E field and B field parallel, or antiparallel. This means that the B field and E field have to be extremely stable with respect to time - the B field has to be the same, as well as the magnitude of the E field. Some discussion will now be done on the systematics of atoms in laser traps.

3.2.2 Systematics in Laser Traps

3.2.2.1 Magnetic Field Gradients

In the Hg-199 experiment, the relatively large volumes taken up by the vapor cells create sensitivity to any gradient in the magnetic field. Suppose there was a difference in the B field magnitude from one cell to the other: The Larmor precession frequency would be different, causing a false EDM signature! For this reason, two more vapor cells are used, placed above and below the vapor cells used for the measurement, which have no E field applied. The precession in the cells is also measured, and is used as a comagnetometer. The true EDM signature used for the Hg-199 experiment is

$$\eta_B \Delta\omega_{EDM} = \eta_B(\Delta\omega_{MT-MB} - k\Delta\omega_{OT-OB})$$

where ω_{MT-MB} is the frequency shift between the cells with an E field applied, ω_{OT-OB} is the frequency shift between the cells without any E field applied, one on top and one on bottom, k is a fit parameter assigned to the data from each day, and $\eta_B = \frac{\mathbf{B_0}\cdot\hat{y}}{|B_0|}$ is a scaling of the B field to account for any temporal variation in the B field magnitude. Any measurement in which the $\Delta\omega_{OT-OB}$ is dominated is discarded for the purpose of the experiment, but taken into account for quantifying the systematic error due to axial motion. If, when E field is applied, the position of the cells shifts slightly, then there is a shift in frequency dependent on E caused by the magnetic field gradient, giving a false EDM signature. This systematic was quantified at $1.26 \times 10^{-30} e \cdot cm$, the dominant systematic in the measurement.

By reducing the size of the volume the atoms are measured in, the effect of any B field gradient can be greatly reduced. Whereas the atoms in the Hg-199 experiment take up a

volume of $5cm^3$, the atoms in an ODT take up a volume of $100\mu m^3$, greatly reducing any effect due to B field gradient.

3.2.2.2 $\mathbf{E} \times \mathbf{v}$

One of the major advantages in using a laser trap is a reduction in the systematic associated with $\mathbf{E} \times \mathbf{v}$. When a charged particle moves through an electric field, electric field appears in the rest frame of the particle as a magnetic field. This induces a B-field, which acts upon the particle. The formula for this B-field is:

$$\mathbf{B}_{motion} = \frac{c}{\sqrt{c^2 - v^2}}(\frac{\mathbf{v}}{c^2} \times \mathbf{E}) \approx \frac{\mathbf{v}}{c^2} \times \mathbf{E}$$

The trapped atoms inside have a Doppler cooling limit of 9, which corresponds to a root-mean-squared (rms) velocity of $v_D = .022m/s$. This creates a B field of $\|\mathbf{B}_{motion}\| = 1.6 \times 10^{-12}T$. This is an issue, because any change in the B field will create a false EDM signature. Thankfully, since the atoms are oscillating in the trap, the effect of the B field mostly cancels out - the atoms oscillate in, say the x direction with a time-dependent velocity $v_x = v_{xmax}sin(t\omega_{ODT})$, so the time-averaged effect on the EDM signature across a full period $\tau_{ODT} = \frac{2\pi}{\omega_{ODT}}$ is 0.

3.3 Experimental Apparatus

The apparatus used for laser cooling and trapping radium atoms, then transporting them to the area where the experiment is performed, is a relatively small but complex experimental setup. It has been compared to "Getting a whole lot of plates spinning at the same time, then once they all are, using that window to perform an experiment." This section will provide

Figure 3.2: Full Apparatus at Argonne National Laboratory

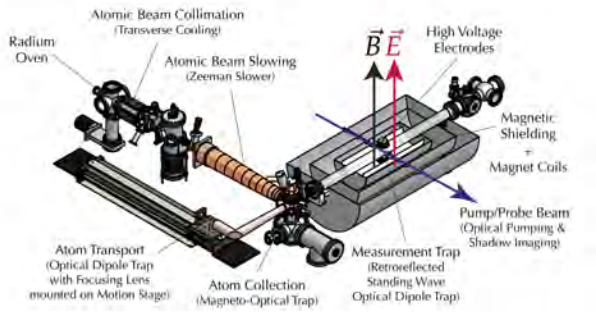

a rundown and explanation of the various parts of the setup. For further information, see [37], [38], [39]

3.3.1 Radium Source/Oven

In order to trap radium, first an atomic beam of neutral Radium must be created. The chemistry to produce this atomic beam is not well understood, but works [40]. The Radium, be it the most abundant Ra-226 isotope to calibrate or rare Ra-225 to measure, arrives to Argonne National Laboratory in the form of Radium Nitrate. This chemical is deposited onto a piece of aluminum foil, and allowed to dry, along with a small amount of metallic barium. Once dry, this foil is then placed inside a titanium crucible, and sealed in a transport container, from which it is the job of a graduate student to transport the container down the hallway from the radiation preparatory lab to the lab containing the experimental apparatus. Once there, the crucible is installed in a vacuum oven. This oven consists of a filament, woven through pieces of ceramic to surround the crucible, and cause it to heat up through thermal radiation. A cooling jacket surrounds the filament, through which chilled water is pumped through, to keep the rest of the apparatus cool. To make sure there is no danger of the chiller failing while the oven is on, causing pressure to build up in the cooling jacket from steam,

a temperature sensor and a flow sensor are connected on the same coolant lines. The oven that provides current to the filament is powered by a power line with an interlock that trips if the flow stops or the temperature gets too high. This way, if the coolant stops flowing, power is automatically cut to the filament. Once the oven is loaded, to get an initial atomic beam of atoms out, the oven must be "cracked". The current through the oven filament, and thus the temperature, is slowly increased. The increase has to be gradual, because the oven is exposed to air during the loading process. This means that, even after pumping down afterwards, the sides of the oven still outgas, so care has to be taken the pressure of the oven doesn't get to high at any one time. While the oven is being warmed up, a fluorescence scan measurement is done, to see if the atoms are beginning to crack. Once a fluorescence signal is visible from the beam, the crack is complete, and the oven temperature is quickly turned down, so as not to waste any radium. After this, a beam of neutral Radium can be produced at a temperature lower than that used to crack, and trapping can begin.

Table 3.3: Typical Values for Oven Loads

Isotope	Typical Cracking Temperature (C)	Typical Activity (Ci)
Ra-226	500	3 μCi
Ra-225	500	10 mCi
Ra-223	500	10 mCi

3.3.2 Transverse Cooling

The first component encountered by atoms leaving the oven is the Transverse cooling. This is an element designed to focus the atoms into a more colinear beam by laser cooling them in the two directions perpendicular to the atomic beamline.

As the atoms emerge from the oven, they do not necessarily emerge perfectly in the z

Figure 3.3: Diagram of Transverse Cooling

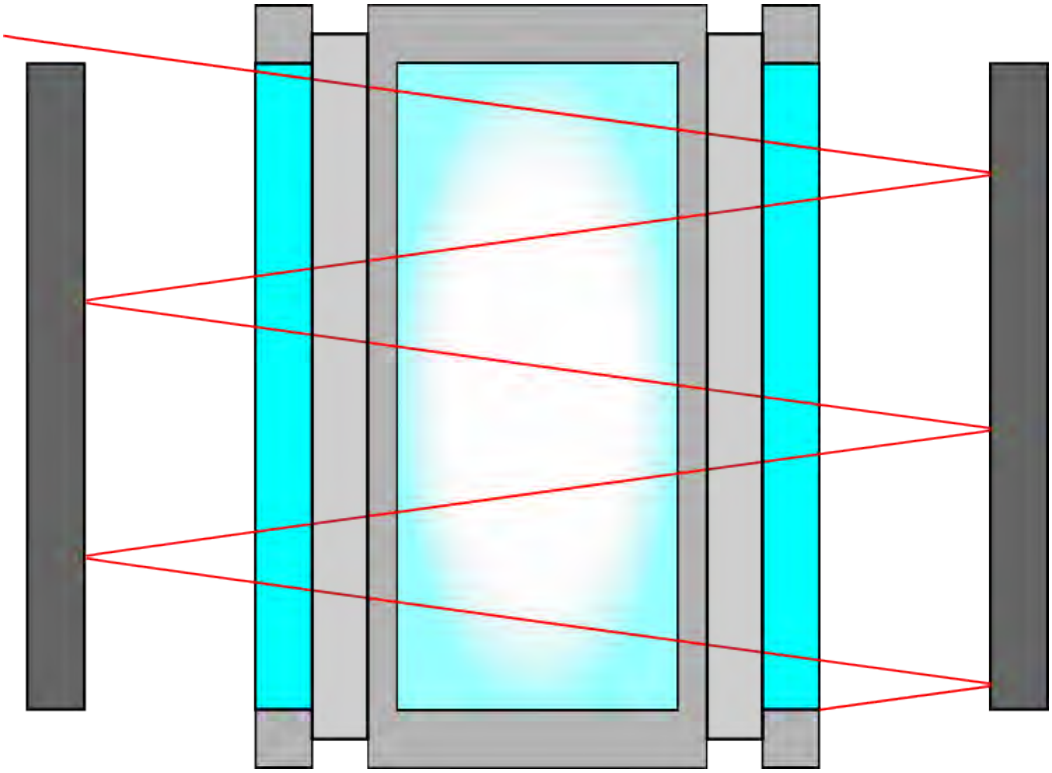

direction; they have a small transverse velocity as well:

$$\mathbf{v} = v_z\hat{z} + v_x\hat{x} + v_y\hat{y} \tag{3.1}$$

In order to reduce v_x and v_y, laser cooling is utilized. When an atom is met with a beam of light, it will absorb photons at a rate R_{scatt} dependent on the light frequency and its own atomic transitions, given by[41]:

$$R_{scatt} = \frac{\Gamma}{2}\frac{\frac{\Omega^2}{2}}{\delta^2 + \frac{\Omega^2}{2} + \frac{\Gamma^2}{4}} \tag{3.2}$$

where Γ is the natural linewidth of the transition, and equal to $\Gamma = \frac{1}{\tau}$ where τ is the average lifetime of the state. Ω is a quantity known as the Rabi frequency, and $\delta = \omega - \omega_0$

is the detuning of the frequency of the light from the frequency of the transition. The Rabi frequency can be determined by the formula

$$\frac{I}{I_{sat}} = \frac{2\Omega^2}{\Gamma^2} \tag{3.3}$$

where I is the laser intensity, and I_{sat} is the saturation intensity equal to

$$\frac{\pi}{3}\frac{hc}{\lambda^3\tau}$$

. For every photon absorbed by the atom, the atom receives a change in momentum equal to

$$p_\gamma = c\hbar\omega \tag{3.4}$$

When the atom decays from its excited state back to its ground state, it emits a photon in a random direction. Thus, over many photon scatterings, the total change in momentum averages out to zero. Combined with the scattering rate, this means that the total change in momentum per second, or force, on each atom is given by

$$F = p_\gamma R_{scatt} \tag{3.5}$$

Needless to say, in order to focus the beam, atoms on the right should only absorb light going to the left, and vice versa. This is done by taking advantage of the Doppler shift of the atoms in the atomic beam. When an atom with a non-zero transverse direction encouters a beam of light, the frequency seen by the atom changes by a factor $\Delta\omega = \frac{\omega_{lab}}{c}v$, where ω_{lab} is the laser frequency from the laboratory frame, and v is the velocity of the atom. Thus,

by detuning the laser slightly from the normal transition, only atoms going to the right will be on resonance with the light going to the left, and vice versa.

3.3.3 Zeeman Slower

As the atoms progress down the atomic beamline, they have to be slowed down enough to be able to be trapped. This is done through laser fluorescence. When an atom meets a beam of light with a frequency on resonance with an atomic transition, it will absorb the light, and reach its excited state. When it absorbs the light, it absorbs the momentum of a photon as well, When the atom decays from its excited state back to its ground state, the atom will emit a photon in an isotropic direction. The time-averaged effect of the photons emitted is therefore zero. Thus, the atom receives a net slowing effect from the laser. There is, however, one problem: as the velocity of the atoms is slowed, there is a Doppler shift in the frequency of the laser that the atoms see, as a function of the speed of the atoms traveling against the laser. This means, as the atoms slow down, they become off-resonance with the frequency of the laser. The solution to this is to apply a tapered magnetic field, which uses the Zeeman effect to shift the energy levels of the atoms slightly. This way, the atomic transition is always on resonance with the laser frequency seen by the atoms, allowing them to be slowed.

The change in the laser frequency seen by the atoms as a function of their z velocity is $\Delta\omega = \frac{\omega_{lab}}{c} v_z$. The desired slowing should give the function v_z of

$$v_z(z) = v_0\sqrt{1 - \frac{z}{L_0}} \tag{3.6}$$

where v_0 is the maximum initial velocity, and L_0 is the length of the Zeeman slower. Since

the primary 3P1 transition has an average lifetime of 420 ns, each "kick" from a photon can be assumed to take up 420 ns. This lifetime thus limits the maximum speed of an atom that can be slowed in a given distance.

3.3.3.1 Optical Cycling

A diagram of the optical transitions is shown below.

Figure 3.4: Various Transitions Used for Optical Cycling

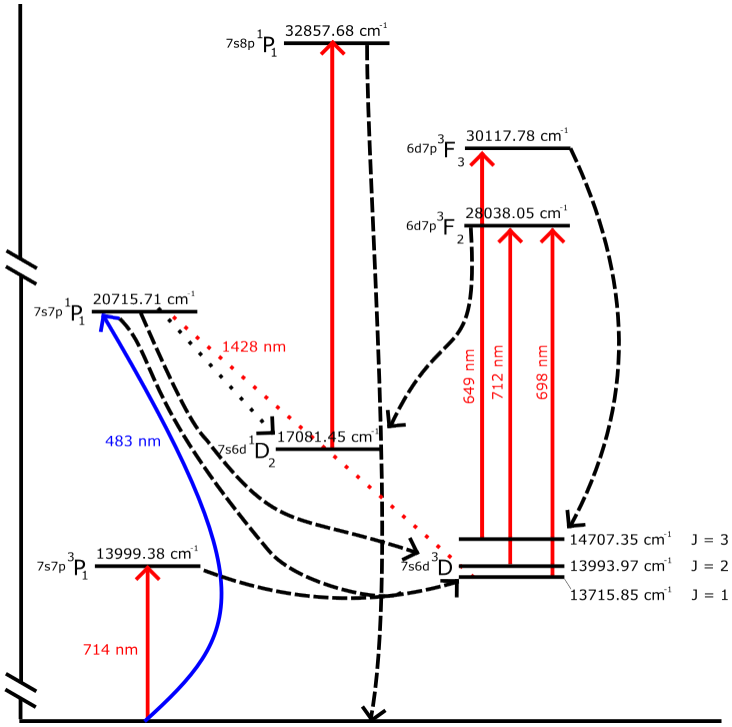

The primary transition is the 714 nm transition, which is created by a Lighthosue Photonics SPROUT pump laser driving a SirAH Mattisse Ti:Sapph laser. The laser is able to output roughly 1.5 W of power of 714 nm light, which is used in various parts of the experiment, from the transverse cooling to slowing to the MOT trapping. The 3P1 state has an average lifetime of 420 ns. The Zeeman slower is 90 cm long. This means that the Zeeman slower is only capable of slowing atoms moving up to 60 m/s, which is less than 1% of the

Figure 3.5: Concept Diagram of MOT

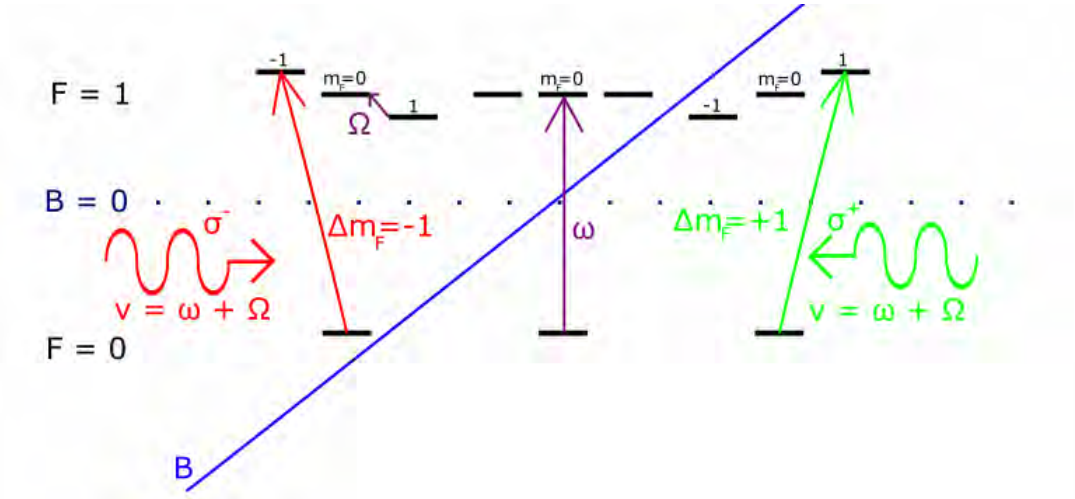

atoms coming out of the oven. Furthermore, due to the branching ratio to the relatively long lived 3D1 state, the vast majority of atoms will at some point end up in the 3D1 state, where they no longer are able to be cooled. This necessitates the use of a repump laser. The 1428 nm Repump laser is beat locked to another laser locked to a cavity, though it doesn't need to be locked to still trap atoms, just in the right place. The purpose of the repump is to transfer atoms out of the dark 3D1 state to the 1P1 state, which decays usually to the 1S0 state, thus keeping the atoms in the cycle, allowing them to still be slowed.

3.3.4 MOT

Once the atoms are sufficiently slowed down, they are trapped by a 3-dimensional Magnetic Optical Trap, or MOT.

The MOT uses a gradient B field and the Zeeman effect to split the energy levels of the m_F substates. Then two laser beams, each with an opposite circular polarization, are overlapped inside. The frequencies of the laser beams are detuned away from the frequency of the primary transition, corresponding to the Zeeman splitting at a certain displacement

from the center. On the right, the B field causes the $m_f = 1$ state to now be resonant with both lasers. However, because the change in sublevel $\Delta m_F = 1$, only the light being shone from the right can be absorbed by the atom. So, if the atom is on the right side, it can only absorb light moving to the left. This means it only absorbs the momentum of the light moving it to the left, causing it to recieve a "kick" back to the center of the trap. The same goes for the left side; the B field gradient causes the $m_F = -1$ sublevel to be on resonance with the laser, but only negatively polarized light can be absorbed, so it can only receive a "kick" to the right when it is on the left.

There is a slight detuning for all the laser components, depending on where they are going on the apparatus. A table for typical AOM values is shown here:

Table 3.4: Typical Values for Frequencies

AOM	Frequency (MHz)
Probe	81 MHz
Slower	77.7 MHz
ULE Offset	79.7 MHz

Figure 3.6: Setup of AOMs at Argonne National Laboratory

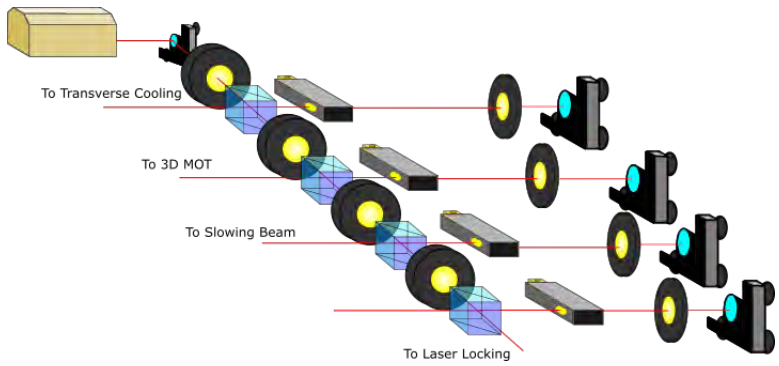

3.3.5 ODT

Once the atoms are trapped in the MOT, they have to be transported to in between a pair of electrodes and magentic coils to perform the EDM measurement. The science chamber is magnetically shielded, in order to stop ambient magnetic fields from affecting the EDM measurement. The transport is performed using an optical dipole trap, or ODT, which is referred to as a Bus ODT. A 100 W laser at 1550 nm is focused by a lens on a translation stage that has its focal point focused on the 3D MOT. Once the atoms are moved to the ODT, the translation stage has its lens physically moved to translate the atoms down to the scientific measurement area. Here, the EDM measurement is performed.

3.3.6 Electric Fields

Inside the measurement chamber, a pair of electrodes apply a strong electric field, either parallel or antiparallel to the applied magnetic field. These electrodes have been carefully conditioned to be able to accept very high electric fields, without discharge [**?**]. In the 2015 data run, the electric field applied to the atoms was $\pm$67kV/cm. With new electrodes, and a new HV apparatus, we hope to reach E-field magnitudes of up to 300kV/cm.

3.3.7 Magnetic Fields

The magnetic field created for the spin precession measurement is created by a cos θ coil. The B field was specifically chosen to give a deliberately chosen to give the Larmor Spin precession a specific frequency, with a field strength of 2.6μT. This causes the atoms to precess due to the B field with a period of $34.7 \pm .03$ms[36]. Note that the actual EDM measurement measures a relative phase shift, not an absolute frequency, so the uncertainty

in our spin precession frequency does not limit our EDM measurement. The actual method of spin detection will be discussed now.

Figure 3.7: Conceptual Diagram of Spin Precession Measurement

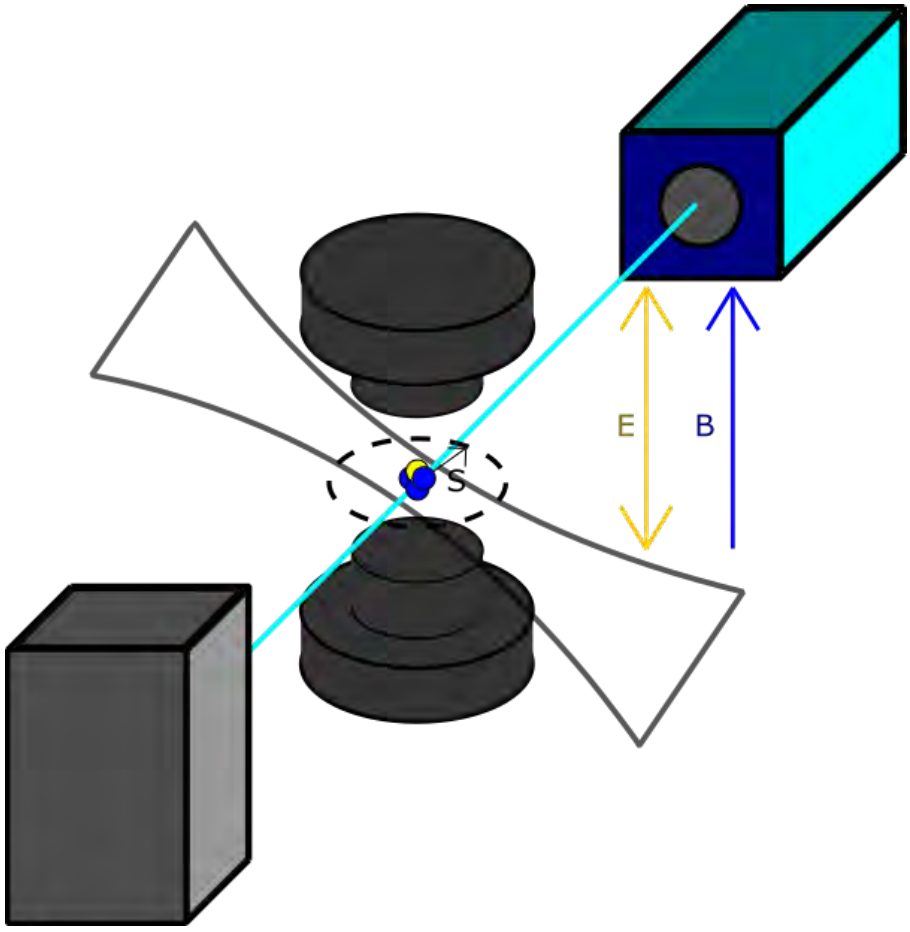

3.3.8 Spin Detection

When the atoms are translated over by the ODT in the Z direction, they are then held in another 10W 1550 nm ODT in the X direction. This holds the atoms in place for the measurement. In order to perform the measurement, a laser resonant with the $^1P_1$ transition excites the atoms, so that all of them are spin polarized in the x direction. Then the laser is turned off and the E field is turned on, so that the atoms precess over 20 seconds, plus

an extra phase shift of a few ms. Then, a shadow imaging measurement is made. The polarized laser is pulsed again, and depending on the phase of the atoms as the precess in the Y direction, a certain percentage of the atoms in the trap absorb light, and the other percentage doesn't. By looking at the loss of light intensity in the shadow created, the phase of the spin precession versus time can be traced out with many measurements. Every load of atoms has 5 intensity measurements taken of it[36]:

Figure 3.8: Spin Precession Measurement Cycle

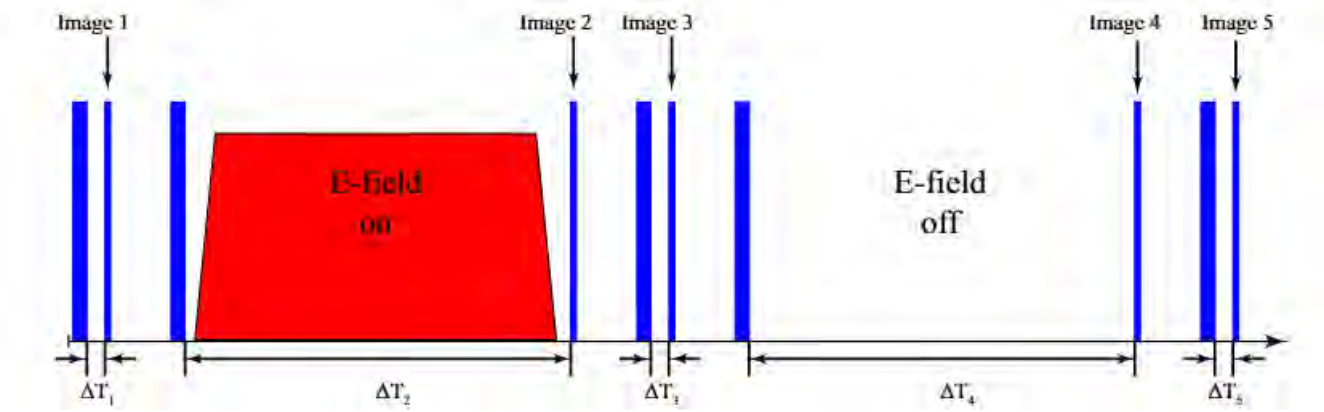

one right after the atoms are polarized, to use to normalize the specific load for its given amount of atoms, then the spin precession measurement with the E field on, another normalization measurement, a spin precession measurement with the E field off (to account for systematic effects), and a final spin normalization measurement.

3.4 2015 EDM run

The RaEDM experiment has had two data runs. The first run took place in 2014, and established a 95% confidence interval of

$$|d(^{225}\mathrm{Ra})| < 5.0 \times 10^{-22} e \cdot cm \tag{3.7}$$

This was followed the next year, with a run that utilized a Titanium Sublimation pump to allow for longer spin precession time. This run established a 95% confidence interval of

$$|d(^{225}\mathrm{Ra})| < 1.4 \times 10^{-23} e \cdot cm \tag{3.8}$$

The systematic and statistical uncertainties had to be very well accounted for such a sensitive experiment, and will be discussed here.

3.4.1 Statistical Sensitivity

The general formula for the statistical standard quantum limit is given by:

$$\delta d = \frac{\hbar}{E\sqrt{NT\tau\epsilon}} \tag{3.9}$$

where E is the electric field strength, N is the number of atoms trapped per load cycle, T is the total integration time of the experiment, τ is the spin precession time of the atoms, and ϵ is the efficiency of the spin detection of the measurement. At the moment, this experiment is completely limited statistically for the next few orders of magnitude - Our experiment should become better with simply measuring more atoms. An overview of the statistical uncertainties can be found here:

Table 3.5: Systematic Uncertainties for 2015 RaEDM Data Run

Effect	Current Uncertainty($e \cdot cm$)
E-Squared Effects	1×10^{-25}
B-Field Correlations	1×10^{-25}
Holding ODT Power Correlations	6×10^{-26}
Stark Interference	6×10^{-26}
E-Field Ramping	9×10^{-28}
Blue Laser Power Correlations	7×10^{-28}
Blue Laser Frequency Correlations	4×10^{-28}
$\mathbf{E} \times \mathbf{v}$ effects	4×10^{-28}
Leakage Current	3×10^{-28}
Geometric Phase	3×10^{-31}
Total	2×10^{-25}

3.4.2 E-Squared Effects

The primary systematic effect limiting the systematic of our expreiment are E-squared effects. While the experiment is going on, in addition to spin precessions with the E-field applied, precessions with the E-field off are also taken. The function that is ultimately fit to the sinusoidal curve drawn out by the spin precession is:

$$y_{E=0} = \frac{A}{1+P}[1 - Pcos(\omega \Delta T)] \tag{3.10}$$

and

$$y_{E\neq 0} = \frac{A}{1+P}[1 - Pcos(\omega \Delta T + \theta \pm \frac{\Delta\phi}{2})] \tag{3.11}$$

Where A is the normalization constant, P is the signal contrast, ω is the spin precession time due to magnetic dipole coupling, ΔT is the spin precession time, θ is a phase shift correlated to E-squared effects, and $\Delta\phi$ is the phase shift due to the EDM coupling. The θ

term is there specifically to try to fit for non-zero E-squared effect, and since it depends on the fit, it means this systematic is dependent on the statistical uncertainty of the experiment. As the statistical uncertainty improves, so should this systematic error. There are other methods for reducing this systematic, however. Since the E-squared effect is dependent only on the magnitude of the electric field and not its orientation, if the E-field is the same both parallel and antiparallel, then this effect will cancel out with regards to the phase shift between the parallel and antiparallel measurements. During the 2015 run, the electric fields were verified to be the same, to within 0.7%. Efforts are ongoing to improve the sensitivity with which these E fields can be measured, and will be discussed later.

3.4.3 B-Field Correlations

B-field correlations are the other significant systematic effect in the experiment. Since the signal depends on a shift in the Larmor precession dependent on both B and E field, it is very important that the drift in time in the B field between different polarities, or ΔB, is as small as possible. There are three fluxgates installed in the chamber to monitor the signal, and in future measurements an installed low-pass filter should be able to measure changes on the order of 6 pT for 1s of integration time.

3.4.4 Holding ODT Power Correlations

Atoms trapped in a holding beam experience a Stark shift proportional to the power of the beam trapping them. For the atoms being held in the ODT while precessing, this means that a correlation between E field direction and ODT power can cause a change in the energy levels, resulting in a false EDM signature. A detailed calculation of this energy shift for

Ra-225 is described later in this thesis. This effect is very suppressed, both with the small energy shift calculated, and the fact that the ODT holding beam is greater than 99% linearly polarized. The false EDM signature that arises can be characterized as

$$d_{\text{false}} = \Delta\nu_{m_F=1/2}\frac{h}{2E}\frac{\Delta P}{P_0} \tag{3.12}$$

where $\frac{\Delta P}{P_0}$ is the fractional difference in holding beam power, and $\Delta\nu_{m_F=1/2}$ is the Stark shift caused by the ODT for the $m_F = 1/2$ sublevel. For the 2015 run, there was no observable correlation between $\frac{\Delta P}{P_0}$ and the E field to a 1σ confidence interval of 8×10^{-5}, resulting in a systematic uncertainty of $6 \times 10^{-26} e \cdot cm$.

3.4.5 Stark Interference

In addition to the Stark shift due to the application of the ODT, there is another shift due to the interaction of the application of the ODT with the E field applied. This effect is linear in both E field strength, as well as ODT power. The effect has a form that looks something like

$$\Delta\nu = \nu_1(\hat{b}\cdot\hat{\sigma})(\hat{\epsilon}\cdot\hat{\epsilon_s}) + \nu_2(\hat{b}\cdot\hat{\epsilon_s})(\hat{\epsilon}\cdot\hat{\sigma}) \tag{3.13}$$

where ν_1 and ν_2 are quantities that can be calculated, $\hat{b}$ is the direction of the holding B field, $\hat{\sigma}$ is the spin quantization axis, $\hat{\epsilon}$ is the ODT polarization direction, and $\hat{\epsilon_s}$ is the direction of the static E field. It was measured that $(\hat{b}\cdot\hat{\sigma})(\hat{\epsilon}\cdot\hat{\epsilon_s}) < .03$ and $(\hat{b}\cdot\hat{\epsilon_s})(\hat{\epsilon}\cdot\hat{\sigma}) < .1$ for our experiment to 1σ uncertainty. This gives a 1σ uncertainty of $6 \times 10^{-26} e \cdot cm$ for this effect.

3.4.6 E-Field Ramping

The E-field, while ramping up and down from high voltage, changes in time, which in term induces a B-field. This effect is made sure to cancel out between the ramp up and ramp down, since the ramping is controlled by an arbitrary wave-form generator. The B fields that arise from this can be found with Amperes law. There are two places that they arise:

$$B_{cur} = \frac{\mu_0}{4\pi} \int_C \frac{I\mathbf{dI} \times \mathbf{r}'}{|\mathbf{r}'|^3} \tag{3.14}$$

and $\mathbf{B_{dE/dt}}$, which is such that

$$\int_{\delta\Sigma'} \mathbf{B_{dE/dt}} \cdot \mathbf{dI}' = \mu_0 \epsilon_0 \frac{d}{dt} \int \int_{\Sigma'} \mathbf{E} \cdot \mathbf{dS}' \tag{3.15}$$

Here, $\mathbf{B_{cur}}$ is the B field induced by the current, which leads through the copper leads from the HV supply to the electrodes. Then, $\mathbf{B_{dE/dt}}$ is the B field induced on the edges of the electrodes due to the changing E field flux. We assume a perfectly linear ramp, and assume the placement of the atoms near the edge of the electrodes, where the B field is strongest. The resulting false EDM signature looks something like

$$\Delta\phi_{\text{false}} = 2\pi t_0 \Delta\nu_{\text{false}} = 2\pi t_0 4\mu |B_{ind}| sin(\theta_{EB})/h \tag{3.16}$$

where t_0 is the duration of the ramp, B_0 is the sum of B_{cur} and $B_{dE/dt}$, and This calculation results in a 1σ systematic error of 9×10^{-28}.

3.4.7 Blue Laser Frequency Correlations

Any correlation between a frequency shift in the blue imaging laser and the E field orientation can create a false EDM signal. These arise from the fact that a shift in the frequency will change the amplitude A of the precession curve, which if correlated with the phase shift $\Delta\phi$, can cause a shift in $\Delta\phi$. To quantify this effect, part of the 483 nm laser light is put through a reference cavity, and the power output of the cavity constantly measured in real time with a photodiode. Using this, the fraction of fluctuation in the amplitude over the amplitude itself was recorded at -75 ± 80ppm. Then, the fluctuation in output cavity power amplitude can be used to estimate the fluctuation of the photon scattering amplitude by

$$\Delta A_{\mathrm{Ra}} = \frac{3\sqrt{3}}{8}\frac{\Gamma_{cav}}{\Gamma_{Ra}}\sqrt{\Delta A_{cav}} \tag{3.17}$$

where Γ_{cav} is the cavity Full Width Half Maximum, Γ_{Ra} is the FWHM of the atomic transition, and $|\Delta A_{\mathrm{cav}}| = 75 \pm 80\mathrm{ppm} << 1$.

Then, the false EDM phase shift is given by

$$\Delta\phi_{\mathrm{false}} = \Delta A_{\mathrm{Ra}}\frac{\rho_{A,\Delta\phi}}{\rho_{A,A}} \tag{3.18}$$

where $\rho_{A,\Delta\phi}$ is the covariance of A and $\Delta\phi$ and $\rho_{A,A}$ is the variance of A. Also, since the atoms are detected 390 ms after the E field is ramped down, with a 1/e time of 160 ms, the E field is reduced to 0.09 of its initial value, so any effect has an additional 0.09 suppression factor. This all gives a final systematic uncertainty of $4 \times 10^{-28} e \cdot cm$ for this effect.

3.4.8 Blue Laser Power Correlations

The signal used to fit for the EDM effect $\Delta\phi$ is a shadow imaging measurement, and is proportional to the power of the laser light used for the atomic scattering. Thus, any correlation between the power of the laser beam and the electric field E can create a false EDM effect. By comparing the backgrounds of adjacent measurements of parallel and antiparallel fields, this uncertainty can be quantified. The comparison yields a 1σ uncertainty in the correlated power functions to 0.2%. Then, using a similar analysis as for the Blue Laser Frequency Correlations, a systematic uncertainty of $7 \times 10^{-28} e \cdot cm$.

3.4.9 $\mathbf{E} \times \mathbf{v}$ effects

As atoms travel with a velocity $\mathbf{v}$ inside the ODT, the static E field applied also appears as a B field, calculated by

$$\mathbf{B_{motion}} = \gamma(\frac{\mathbf{v}}{c^2} \times \mathbf{E}) \tag{3.19}$$

where $\gamma = 1$, for the non-relativistic motion of our atoms. The Doppler cooling limit of our trap is 9μK, which corresponds to an root-mean-squared velocity of $v_D = 0.022 m/s$. Since the atoms travel inside the trap with harmonic motion, they oscillate back and forth in each direction with some period τ_{trap}. Over the course of a single period, the effect is cancelled out. Assuming the maximum amount of non-canceled-out B field, the resulting false EDM signature can be quantified by

$$d_{\text{false}} = \frac{\mu|\mathbf{B_{motion}}|}{E} \frac{\tau_{\text{trap}}}{2\tau} sin(\theta_{EB}) \tag{3.20}$$

where τ_{trap} is the period of the harmonic motion of the atoms in the ODT trap, τ is the spin precession time, and θ_{EB} is the angle between the ODT and the applied B field. The trap frequency was given to be $\omega_{trap,x} = 2\pi \times 4.25 rad/s$, with $\tau_{trap} = 2\pi/\omega_{trap}$. This gives a 1σ uncertainty of $4 \times 10^{-28} e \cdot cm$ for this systematic effect.

3.4.10 Discharge and Leakage Current

When electrons are discharged between the electrodes of our experiment, this creates current, which in turn creates a B field, which can lead to a false EDM signature. It should be noted that this discharge current changes its direction whether or not the E field is parallel or antiparallel, and thus the induced B field as well, so this can be especially problematic. There are two primary sources of stray current: leakage current leaking through the macor holder which holds the electrodes, and current caused by discharges between the electrodes. The most problematic of these comes from the discharges, since it would be possible for a discharge to happen right through the atoms, which would accelerate due to the applied static E field. This can be modeled with the electrons as an infinite wire, with the the false EDM signature then given by

$$d_{false} = \frac{\mu \mathbf{B_{ind}}}{E} \cdot \hat{B} = \frac{\mu}{E} \frac{\mu_0 I}{2\pi r} sin\theta_{EB} \tag{3.21}$$

where I is the leakage current, r is the distance of closest approach for the electron beam, and θ_{EB} is the angle between the applied E and B fields. The value for θ_{EB} was measured to be $\theta_{EB} < 0.1$rad. The leakage current was consistent with 0, and had a 1σ uppper limit of 2 pA. This resulted in a 1σ uncertainty for this systematic at $3 \times 10^{-28} e \cdot cm$.

The other path is leakage through the Macor holder, which holds the electrodes apart

from each other. The resulting systematic from this leakage current was caluculated using the leakage current of 2 pA, and was caluclated at $9 \times 10^{-29} e \cdot cm$.

3.4.11 Geometric Phase

With any B field gradient, any slight difference in the position of the atoms within the trap mean the atoms can pick up a geometric phase. This experiment uses a thermal cloud, and averages over all types of orbits. The false EDM signal associated with this is taken from [42], and given as

$$d_{false} = \frac{-F\hbar}{2B_{0z}^2 c^2} |v_{xy}|^2 \frac{\delta B_{0z}}{\delta z} \frac{1}{1 - \frac{\omega_r^2}{\omega_0^2}} \tag{3.22}$$

where F = 1/2 is the total spin, $|v_{xy}| = \sqrt{2/3} v_D$ is the rms speed in the x-y plane, B_{0z} is the magnitude of the applied B field, ω_0 is the larmor frequency, and ω_r is the trap frequency. The gradient in B_{0z} was taken at .1% per cm, which was the measured upper limit. There are two different trap frequency for x and y, with $\omega_x = 4$Hz and $\omega_y = 610$Hz. The resulting 1σ value is $7 \times 10^{-30} e \cdot cm$.

3.5 Radium 223 Results

A large portion of my time at Argonne National Laboratory was spent trying to laser cool and trap Radium-223.

3.5.1 Future Work

Everything was set up in the spring of 2022 for another Ra-223 trapping attempt; we were able to trap Ra-226, so we would be able to start trying to trap Ra-223 from the get go. Also, we would be able to fluoresce another level of the hyperfine of Ra-223, which would give us the B coefficient and isotope shift of the 3P1 state for Ra-223. The measurement of the B coefficient for this state would allow for a quantization of the nuclear charge radius of Ra-223; this in turn would allow us to also predict the B coefficient of the 3D1 state. Armed with this knowledge, this would give us an idea of not only where our primary transition laser would have to be, but also where our repump frequency would need to be. Things were looking up for trapping Ra-223; unforutnately, an accident involving the source of Ra-223 at Oak Ridge National Lab prevented any new Radium-223 from being shipped to us for a very long time. Currently, our experiment is switching back to using Ra-225. We intend to create an oven with a source of Th-229, which decays into Ra-225, as a stopgap until we can get Ra-225 on our hands through the beam dump at FRIB.

3.6 Sensitivity Upgrade Strategy

For the next experimental run of Ra-225, a variety of upgrades are being implemented. Once again, the formula for the statistical uncertainty in our measurement looks like

$$\delta d = \frac{\hbar}{E\sqrt{NT\tau\epsilon}} \tag{3.23}$$

where E is the electric field, N is the number of atoms trapped per measurement, T is the total time of the experiment, τ is the spin precession time, and ϵ is the detection efficiency.

In the next experimental run, we intend to increase the spin precession time of τ, as well improve all of the other variables listed.

3.6.1 Improved Trapping Efficiency - Blue Slower

Currently, our experiment is only able to trap atoms moving up to 60 m/s, due to the relatively long lifetime of the 3P1 excited state. This only allows our trap to trap less than 1% of the total atoms out of our oven. We intend to implement a new trapping scheme utilizing the stronger 1P1 transition, which has a much shorter lived lifetime. However, using this transition requries the use of a much more complicated repump scheme. With this scheme implemented, however, we should be able to trap atoms moving up to 300 m/s, which accounts for 63% of the atoms coming out of our oven. This corresponds to an increase of roughly 1 order of magnitude in sensitivity

Figure 3.9: Optical Cycling Scheme Trappping Efficiencies

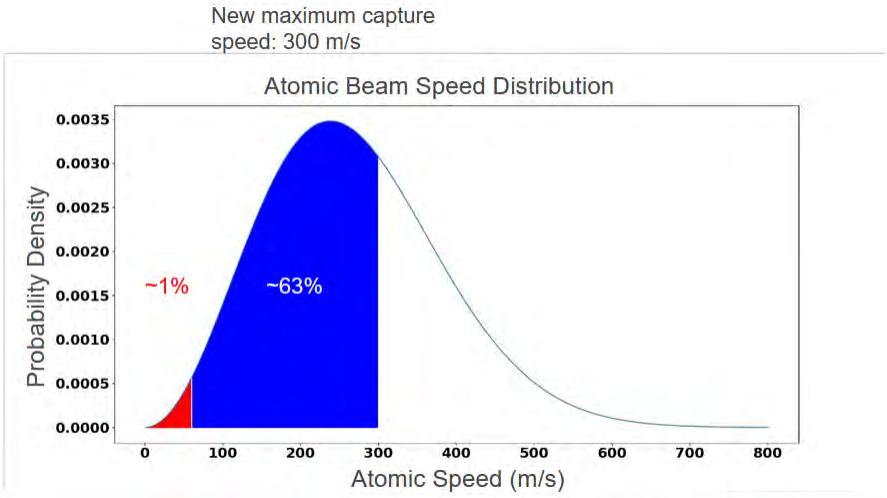

The repumping scheme requires no less than 5 lasers, as opposed to the two required for the red slower transition

Figure 3.10: Blue Slower Optical Cycling Scheme

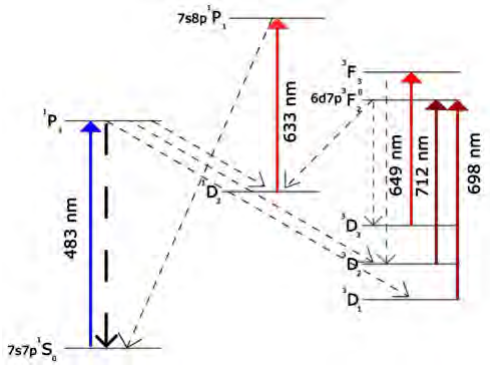

The implementation of this upgrade should improve our parameter N by an additional order of magnitude.

3.6.2 Improved Spin Detection Efficiency - QND

A group in China has demonstrated improved shadow imaging efficiency due to a technique known as Quantum-Non-Demolition, or QND. With our current setup, the Ra-225 atoms we measure are only able to scatter 3 photons on average before they decay from the excited state of the transition to a dark state, where they can no longer be fluoresced. This requires us to take the average of multiple measurements in order to see a clean shadow signal, since relatively few photons are scattered per atom. The QND scheme works by "dressing" the excited states using another laser to make only the desired transition on resonance with our shadow imaging laser. This increases the number of photons scattered per atom from 3 to a few thousand, giving the shadow imaging a much cleaner, clearer signal, and roughly an additional 2 orders of magnitude of sensitivity

3.6.3 Improved Electric Field - HV

Any increase in the applied E field will lead to higher sensitivity to an EDM. In the 2015 run, the applied E field was 65 kV/cm. For the next run, voltages reaching hundreds of kV/cm are planned. Development has been done on a method to treat and condition electrodes to be able to create large electric fields, without any discharges that can create leakage currents. Also in progress is the implementation of a new HV switching scheme. Where as before, a bipolar $\pm$30 kV power supply was used, with the voltage affixed permanently to one of the electrodes, now the intent is to have a unipolar +60 kV power supply, with a series of relays able to switch the high voltage from one electrode to the other, with the other held at ground. This implementation will be discussed more in section 7, and should provide an additional factor of 10 in sensitivity.

3.6.4 New Source of Ra-225 - Isotope Harvesting

The beam dump at the FRIB will allow for the harvesting of rare isotopes created by its beam. This beam dump can be used as a source of Ra-225 for the RaEDM experiment. An apparatus has been built at MSU to measure the efficiency with which a sample of Radium from FRIB could be used to create an atomic beam. These efforts will be discussed further in section 6.

Chapter 4. Radium 223 Trapping Studies

Due to the dearth of Radium-225 available for our experiment, Radium-223 was seen as a potential substitute. This isotope has a similar enhancement factor to Radium-225 in sensitivity for EDM measurements, but adapting to the isotope has proven challenging. The energy levels of certain states have to be identified, specifically for the isotope. Work was done to identify these states.

4.1 Comparison to Ra-225

Radium-223 has a similar octupole deformation to the Radium-225 atom. This makes it a potential substitute, since the experiment is already set up to trap radium. There are issues with the isotope that make it not as ideal as Radium-225, however. To start out with, its half life is only about 11 days, as opposed to the 15 day half life of Radium-225. More importantly, its nulcear spin is 3/2 as opposed to 1/2 for Radium-225. This makes its hyperfine structure much more complicated, and opens it up to additional systematic effects from the tensor shift. Finally, the precise transition frequencies needed to trap the isotope were not known. Effort thus had to be made into finding the necessary transition frequency.

4.2 Energy Level background

While the number of electrons, and thus the electronic structure, mostly stays the same from isotope to isotope, there are shifts and hyperfine splittings in the energy levels that are extremely important to identify to be able to laser cool and trap atoms. This can in fact

become a benefit, as the laser slowing apparatus can be specifically tuned to one specific isotope. There are generally three areas where changes in the spectrum emerge: the isotope shift, the hyperfine A coefficient, and the hyperfine B Coefficient.

4.3 Known Energy Levels

The repumping scheme for the Radium-EDM experiment relies on 2 different transitions: The 714 nm transition from 1S0 to 3P1, and the 1024 nm transition from 3D1 to 1P1. The values of isotope shifts and A and B coefficients were thankfully compiled in 2016[43], and are here presented for Ra-223.

Table 4.1: Isotope Shifts and Hyperfine Coefficients of Ra-223

State	Isotope Shift Relative to Ra-214 (MHz)	A Coefficient (MHz)	B Coefficeint (MHz)
1S0	0	0	0
1P1	-32453(9)	-344.5(0.9)	421.5 (1.6)
3P1	-32934(10)	1202.1(0.6)	-470.2 (1.2)
3D1	?	?	?

So, the 3D1 state in the repumping scheme being unknown for Ra-223 is the issue. In fact, the only known parameters for the shift of this state come from the previous RaEDM run[36]:

Table 4.2: Previously Measured Isotope and A coefficients of the $^3D_1$ For Various Isotopes

Isotope	Isotope Shift (MHz)	A Coefficient (MHz)	B Coefficient (MHz)
Ra-225	540.2	4687.7	N/A

So, there are three values that need to be predicted for the 3D1 state of Radium-223: The Isotope Shift, the A Coefficient, and the B Coefficient.

4.4 Ra-223 Isotope Shift Prediction

There are two physical interactions from which the isotope shift arise: The normal mass shift, the specific mass shift, and the field shift. The normal mass shift is a correction factor due to a shift in the center of mass due to the change of mass in the nucleus, and can be accounted for. The specific mass shift is a factor dependent upon the change in electron configuration, and the field shift is another factor dependent on the electron configuration, though it is also proportional to the nuclear charge radius.

The isotope shift is different for each isotope and transition. The total isotope shift for a given state looks something like

$$\delta\nu_{IS}^{A,A'} = \frac{M - M'}{MM'}(K_{NMS} + K_{SMS}) + F_{FS}\delta\langle r^2\rangle_{MM'} \tag{4.1}$$

where

$$K_{NMS} = m_e\nu_i \tag{4.2}$$

is proportional to the energy of the transition.

4.4.0.1 King Plots

The expression for the isotope shift can be rearranged to something called the King shift for a specific transition i:

$$\Delta\nu_{MM'}^{i,King} = K_{SMS}^i + F_{FS}^i\delta\langle r^2\rangle_{MM'}\frac{MM'}{M - M'} = \delta\nu_{MM'}^i\frac{MM'}{M - M'} - K_{NMS} \tag{4.3}$$

where the normal shift mass parameter K_{NMS} is given by $K_{NMS} = m_e\nu_i$. Thus, the value $\Delta\nu^{i,King}_{MM'}$ can be calculated. Now, consider the King plots for two different transitions:

$$\Delta\nu^{i,King}_{MM'} = K^i_{SMS} + F^i_{FS}\delta\langle r^2\rangle_{MM'}\frac{MM'}{M-M'} \tag{4.4}$$

$$\Delta\nu^{j,King}_{MM'} = K^j_{SMS} + F^j_{FS}\delta\langle r^2\rangle_{MM'}\frac{MM'}{M-M'} \tag{4.5}$$

Between both transitions, the nuclear charge radius doesn't change, and so the equations can be combined into something like

$$\Delta\nu^{j,king}_{M,M'} = \frac{F_j}{F_i}\Delta\nu^{i,king}_{M,M'} + K^i_{SMS}\frac{F_j}{F_i} - K^j_{SMS} \tag{4.6}$$

Notice that the parameters $F_{i,j}$ and $K^{i,j}_{SMS}$ are dependent on the transition only, and not the particular isotope. This means that, if the isotope shift for two specific transitions are known for three specific isotopes, then there are at least 2 different $\Delta\nu^{j,King}_{MM'}$ and $\Delta\nu^{i,King}_{MM'}$, which allows a linear fit to be created, from which the value of $\frac{F_j}{F_i}$ and $K^i_{SMS}\frac{F_j}{F_i} - K^j_{SMS}$ can be calculated. With this information in hand, for another isotope with only one transition's isotope shift known, the other can be calculated. There is one issue: For the 3D1 state, only a single isotope shift, for Ra-225, has ever been measured! This means one further approximation is necessary. For both of the states 1P1 and 3D1 in the 1428 nm repump transition, each has one of the valence electrons in the s-orbital. Generally, in this case, the king plot is dominated by the field shift, since the wavefunction is non-zero at the nucleus. This can be seen in section 6.3 of [**?**], where it is mentioned "The small specific mass shift differences between ionic 4,683Åand atomic 4,825Ålines and also between the

atomic 4,826Åand 7,141Ålines are well within the range usually observed for s, p, s^2, and sp configurations[48]." Thus, the values of K^j_{SMS} and K^i_{SMS} can be approximated to zero, leaving only

$$\Delta\nu^{j,king}_{M,M'} = \frac{F_j}{F_i}\Delta\nu^{i,king}_{M,M'} \tag{4.7}$$

Using the 1P1 and 3D1 states of Radium-225, the field shift ratio can be calculated to be

$$\frac{F_{3D1}}{F_{1P1}} = .2442(.0018)$$

resulting in an isotope shift for the 3D1 state of 223 to be

$$\Delta\nu^{3D1}_{226,223} = 2097(16)MHz$$

So, the Ra-223 isotope 3D1 state is 2102 MHz above the 3D1 state for Ra-226. This value can also be caluclated with the 3P1 state instead of the 1P1 state, which yields $2099(18)MHz$, very much consistent with the previous result.

4.5 Ra-223 $^3D_1$ A Coefficient Prediction

The Hyperfine Splitting of a given state can be described by an A coefficient and a B Coefficient:

$$\Delta E_{hfs} = \frac{A}{2}C + BC(C+1)$$

where

$$C = F(F+1) - I(I+1) - J(J+1)$$

This number can be determined in two different ways. The first is to simply rescale the A Coefficient as it is:

$$\frac{A_1}{A_2} = \frac{\mu_1}{\mu_2}\frac{I_2}{I_1}$$

The computed $A_{3_{D_1}}$ for Ra-223 rescaled from Ra-225 is then:

$$A_{3_{D_1}} = -574 \pm 15.15 MHz$$

The values for this calculation come from [44]:

Table 4.3: Values used for Ra-223 A Coefficient Rescaling

A	I	$\frac{\mu_I}{\mu_N}$	Q_s
223	3/2	.262(5)	1.19(12)
225	1/2	-.713(13)	-

Another way is to utilize Breit-Wills theory[45]. According to this theory, the A coefficient for a state with two valence electrons can be described as a linear combination of two single electron A Coefficients.

4.5.1 Breit Wills Theory

Any perturbation of the Hamiltonian looking like

$$H' = \mathbf{BI} \tag{4.8}$$

where I is the nuclear spin, and B is any purely electronic matrix vector, will give rise to energy splitting like

$$\Delta\omega = \frac{A}{2}(F(F+1) - J(J+1) - I(I+1)) \tag{4.9}$$

where A is given by

$$A = \frac{\mathbf{B} \cdot \mathbf{J}}{J(J+1)} \tag{4.10}$$

For a two-electron configuration, the matrix element for decomposing A into single-electron contributions looks like:

$$(j_1, j_2|\mathbf{BJ}|j_1, j_2) = Q_{12}a_1 + Q_{21}a_2 \tag{4.11}$$

where

$$Q_{ab} = \frac{1}{2}(J(J+1) + j_a(j_a+1) - j_b(j_b+1)) \tag{4.12}$$

The equations for an individual contribution looks like[44] for $L = 0$:

$$a_{ns} = \frac{8\pi}{3}\frac{2\mu_0\mu_B}{4\pi}\frac{\mu_I}{I}|\psi(0)|^2_{ns}F_{1/2}(Z_i)(1-\delta)(1-\epsilon) \tag{4.13}$$

and for $L > 0$:

$$a_{nlj} = \frac{2\mu_0\mu_B}{4\pi}\frac{\mu_I}{I}\frac{l(l+1)}{j(J+1)}\langle r^{-3}\rangle_{nl}F_j(Z_i)(1-\delta)(1-\epsilon) \tag{4.14}$$

where $F_j(Z_i)$ is a relativistic correction factor, $(1-\delta)$ is the relativistic Breit-Rosenthal-Schawlow correction, and $(1-\epsilon)$ is the Bohr-Weisskopt correction. The electronic matrix elements can be described as:

$$|\psi(0)|^2_{ns} = \frac{Z_i Z_0^2}{\pi a_0^3 n^{*3}} \tag{4.15}$$

and

$$\langle r^-3\rangle_{nl} = \frac{Z_i Z_0^2}{a_0^3 n^{*3} l(l+\frac{1}{2})(l+1)} \tag{4.16}$$

Importantly, the only factor that changes between different isotopes is $\frac{\mu_I}{I}$. The isotopes scale like:

$$a_{nlj,N} = a'_{nlj}\frac{\mu_I}{I} \tag{4.17}$$

which means that, if the individual μ_I are known and a_{nlj} is known for any isotope, the a_{nlj} can be found for another isotope. [44] provides calculations for various single electron states for Ra-223:

State	$a_{7s_{1/2}}$	$a_{7p_{1/2}}$	$a_{7p_{3/2}}$
Value(MHz)	2736	371	20.8
Source	[44]	[44]	[44]

So, with the scaling between Ra-223 and Ra-225, we get $a_{7s_{1/2},225} = -22337MHz$. Consider now the $^3D_1$ state of Radium. This state can be decomposed into the sum of its

two electron configuration:

$$2J(J+1)A_{3_{D_1}} = (J(J+1)+j_1(j_1+1)-j_2(j_2+1))a_{7s_{1/2}}+(J(J+1)+j_2(j_2+1)-j_1(j_1+1)a_{6d_{3/2}} \tag{4.18}$$

$$A_{3_{D_1}} = -\frac{1}{4}a_{7s_{1/2}} + \frac{5}{4}a_{6d_{3/2}} \tag{4.19}$$

For the value of

$$A_{3_{D_1}} = 4687.7MHz$$

taken from [46], we can calculate

$$a_{6d_{3/2},225} = -717.24MHz \tag{4.20}$$

Now, rescale to 223:

$$a_{6d_{3/2},223} = a_{6d_{3/2},225}\frac{1/2}{3/2}\frac{\mu_{223}}{\mu_{225}} = 87.85MHz \tag{4.21}$$

So, the predicted $A_{3_{D_1}}$ for Ra-223 is:

$$A_{3_{D_1}} = -574 \pm 19MHz \tag{4.22}$$

Now, move onto the B coefficient

4.6 Ra-223 $^3D_1$ B Coefficient Prediction

Unfortunately, no B coefficient has every been measured of the $^3D_1$ state. This prevents it from being able to be scaled. The best value to use comes from [47], which gives a theoretical calculation for the B Coefficient of the 3D1 state for Ra-223 of $B = 125MHz$. This value is thus used as a starting point. This gives the final predicted values for the Ra-223 3D1 state:

Table 4.4: Estimated Values for the $^3D_1$ State of Radium-223

Isotope Shift (MHz)	A Coefficient (MHz)	B Coefficient (MHz)
2097	-574	125

This gives the potential energy transitions for the Repump frequency:

Table 4.5: Estimated Repump Transition Frequencies

Isotope	Initial State	Final State	Repump Frequency (cm^{-1})	Frequency Shift(MHz)
Ra-226	$^3D_1$ (F = 1)	$^1P_1$ (F = 1)	6999.835	0
Ra-223	$^3D_1$ (F = 5/2)	$^1P_1$ (F = 5/2)	6999.779	-1676
Ra-223	$^3D_1$ (F = 3/2)	$^1P_1$ (F = 5/2)	6999.736	-2955
Ra-223	$^3D_1$ (F = 5/2)	$^1P_1$ (F = 3/2)	6999.790	-1347
Ra-223	$^3D_1$ (F = 3/2)	$^1P_1$ (F = 3/2)	6999.747	-2626

4.7 Ra-223 Beam Fluorescence

In order to get a rough idea of where the primary transition frequency was for Ra-223, a beam fluorescence measurement was done during the initial oven crack. During this period, a very large amount of atomic flux occurs, making it the only time where enough Radium-223 is present to perform a beam spectroscopy measurement upon it. On April 16th, 2021, 2 μCi of Radium-226 and 10 mCi of Radium-223 were loaded into the RaEDM apparatus at

Argonne National Laboratory, under standard loading procedure:

Table 4.6: Oven Load on 04/16/2021

Isotope	Activity (initial)	Number of Atoms (initial)
Ra-226	2 μCi	5.4 $\times 10^{15}$ Atoms
Ra-223	10 mCi	5.1 $\times 10^{14}$ Atoms

So, there was roughly a factor of 10 fewer atoms of Radium-223 than Radium-226 in the oven. The frequency shift in the 3P1 transition between Radium-223 and Radium-226 is 10484.6 MHz. This, remarkably, is extremely close to 7 times the 1497.8 MHz Free-Spectral-Range (FSR) of the 714 nm laser - Thus, by locking the laser to a mode 7 FSRs away, the ULE EOM frequency required would be nearly identical between Ra-226 and Ra-223.

4.7.1 Retro-reflected Beam Spectroscopy Principle

A retro-reflected beam spectroscopy measurement was performed during the oven crack. A principle diagram can be seen below:

Despite the best efforts to ensure that a laser beam is perpendicular to an atomic beam, some small angle will always remain. To account for this, so-called retro-reflection is used. This involves reflecting the laser beam back to its source, using a reflective mirror. By ensuring the reflected laser beam is parallel and with the incoming laser beam, the true fluorescence frequency can be determined. The incoming laser beam, due to relativistic effects, and assuming a small deviation from perpendicularity, sees the atomic transition frequency ω_1 centered at a value:

$$\omega_1 = \omega_0(1 - \frac{v\sin(\theta)}{c}) \tag{4.23}$$

Figure 4.1: Retro-reflected Beam Fluorescence

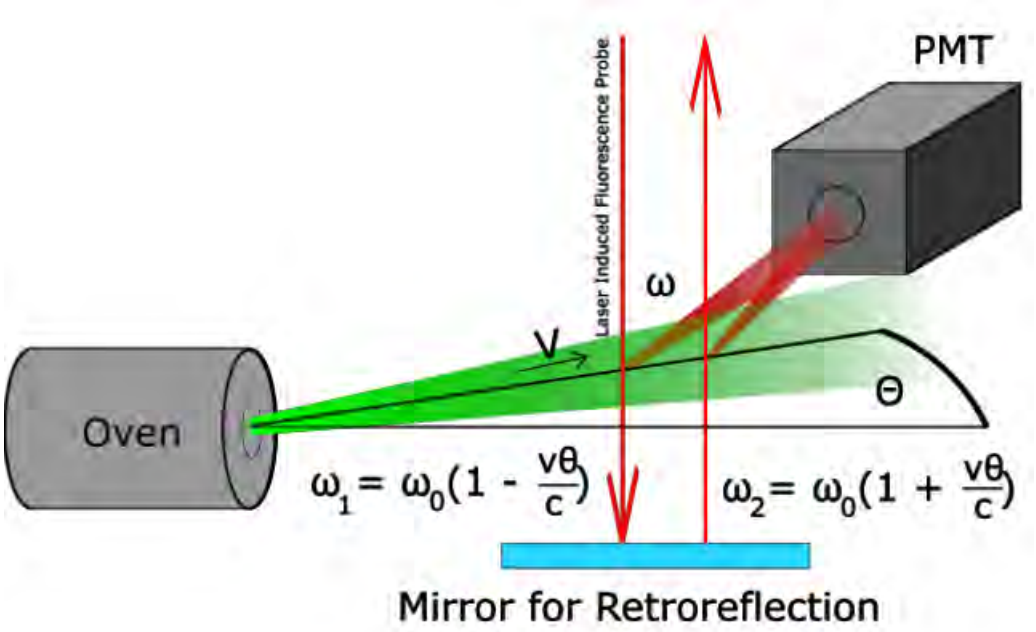

where ω_0 is the true transition frequency, v is the velocity of the incoming atoms, θ is the deviation from perpendicularity between the laser beam and the center of the atomic beam, and c is the speed of light. The atomic transition frequency seen by the reflected beam is then:

$$\omega_2 = \omega_0(1 + \frac{v\sin(\theta)}{c}) \tag{4.24}$$

The fluorescence spectrum then has two peaks to its shape. By taking the midpoint of these two peaks, the true fluorescence value can be determined:

$$\omega_0 = \frac{\omega_1 + \omega_2}{2} \tag{4.25}$$

Figure 4.2: Average of Fluorescence Scans of Radium-226

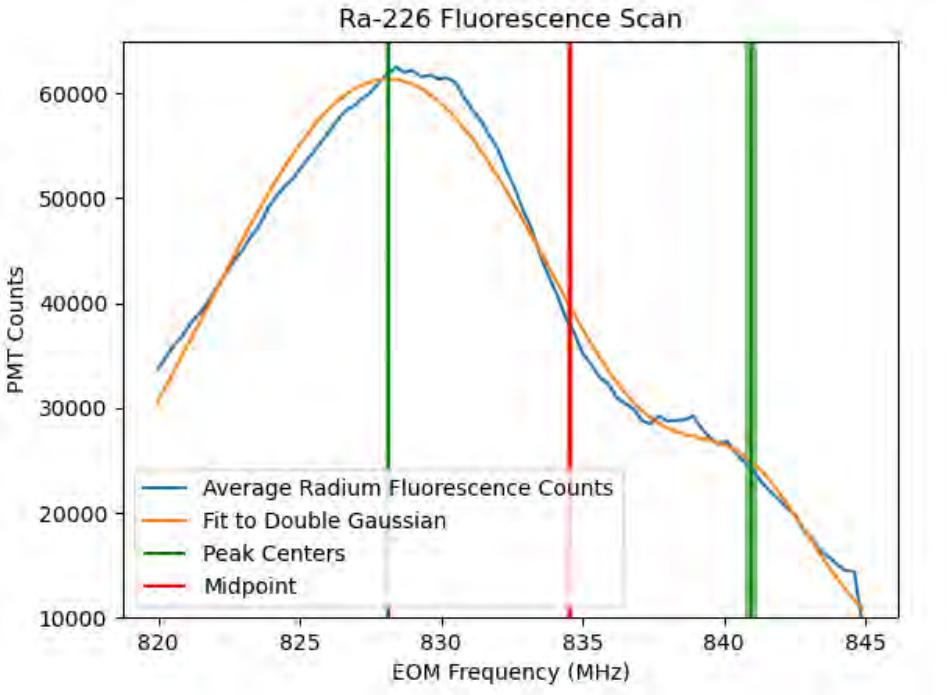

Table 4.7: Gaussian Fits to Oven Crack Scans

Isotope	Peak 1 Location (MHz)	Peak 2 Location (MHz)	Center (MHz)
Ra-226	828.12 ± .07	840.94 ± .22	834.53 ± .12
‘ Ra-223	826.27 ± .06	838.08 ± .19	832.18 ± .10

4.7.2 Beam Spectroscopy of Radium-223

The average of 3 scans was taken, and fit to a double gaussian. This was done for Radium-226 and Radium-223

It should be remembered that the scan for Radium-223 was located 7 FSRs away from Radium-226, so these were not almost at the same point.

Figure 4.3: Average of Fluorescence Scans of Radium-223

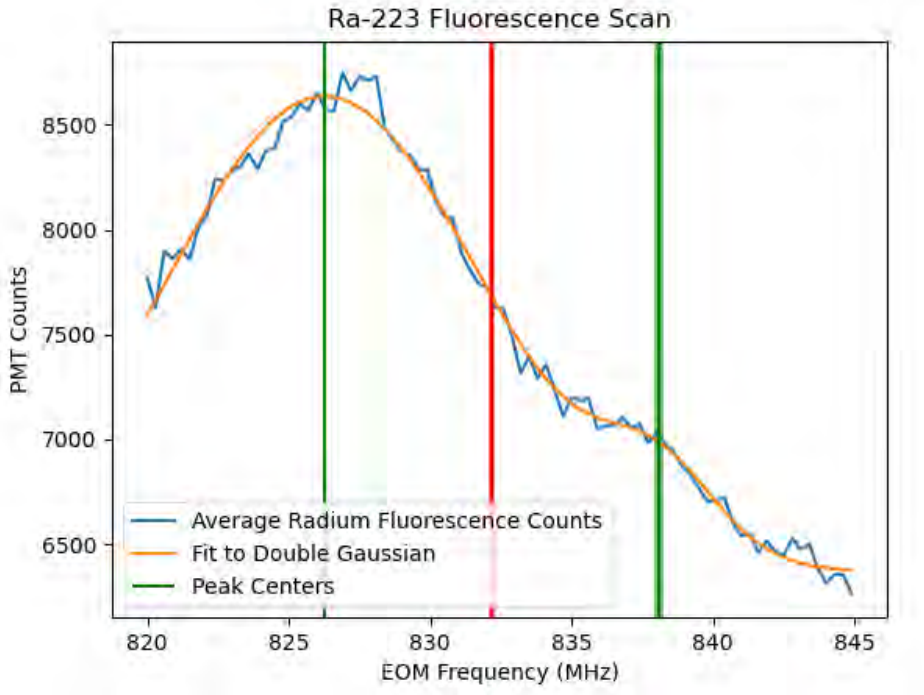

4.8 Ra-223 Trapping Attempts

With the data collected from the beam fluorescence, it was determined that the EOM frequency to attempt to trap Radium-223 should be red-detuned by about 2 MHz. After the crack of the oven, nearly a full half-life of Radium-223 elapsed before Radium-226 was finally able to be trapped. It was found with a ULE EOM Offset of 843.9 MHz.

The shift in the EOM frequency from the beam fluorescence center is believed to be due to a misalignment that was found in the retroreflected beam. The repump frequency used to trap Ra-226 was $6999.835 \pm .0005\text{cm}^{-1}$. The repump laser was not locked during the scanning for Ra-226 or 223, though it seemed stable enough to be accurate to the .001 cm^{-1} level. Data taken on the PMT during these data runs looks something like in Figure 4.5.

Figure 4.4: image of The MOT

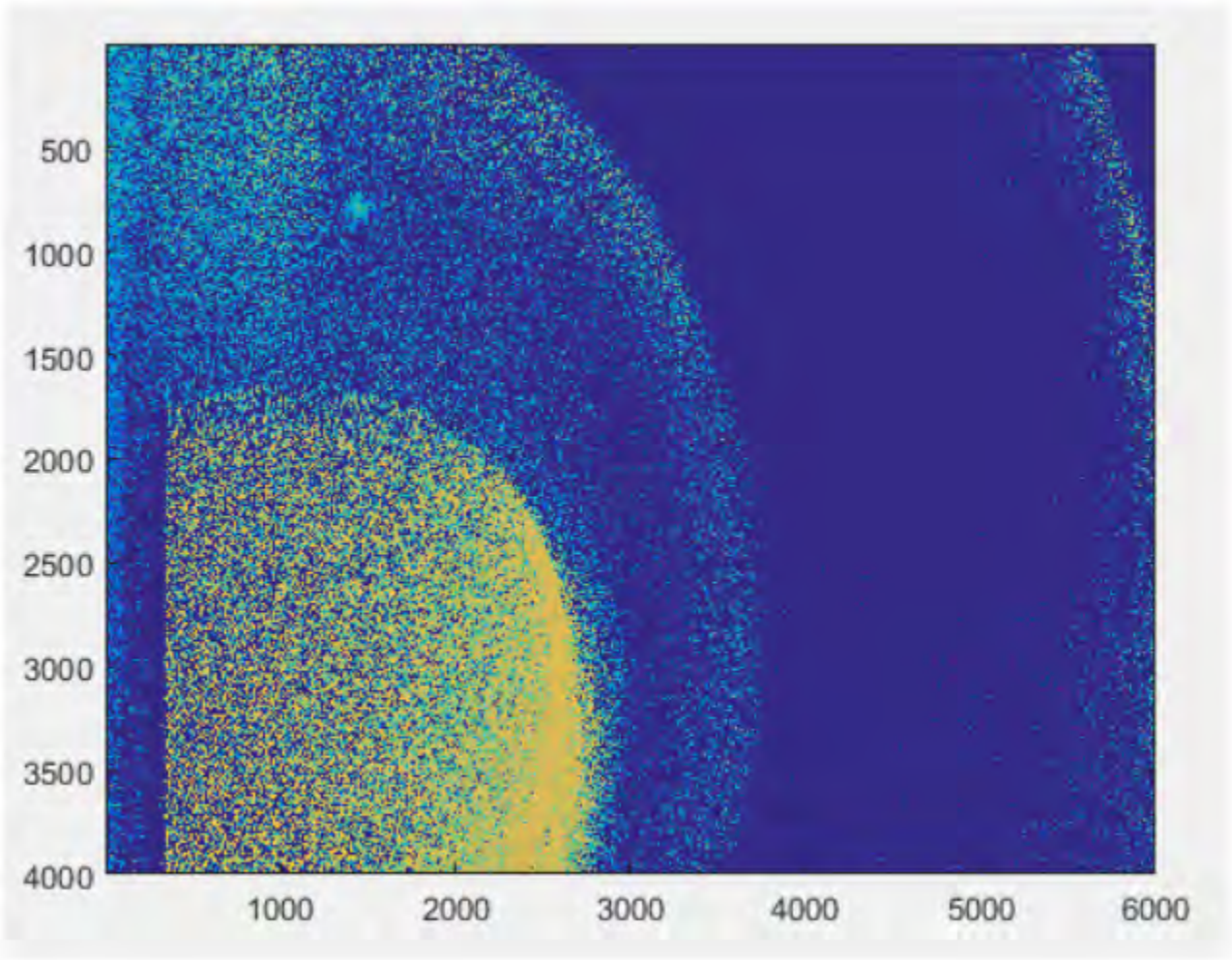

Figure 4.5: PMT Data during MOT Cycles

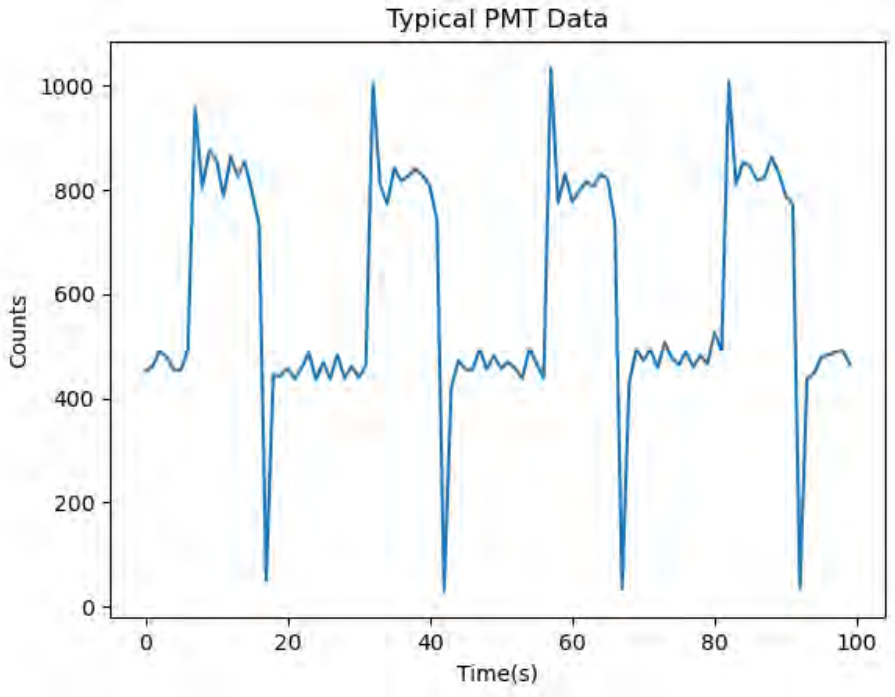

The counts below 600 are taken during the MOT loading phase, during which the PMT is blocked from viewing the MOT chamber. The counts above 600 are taken during the MOT probing phase, which is when fluorescence is attempted. For looking for Ra-223 fluorescence, only the probe phase data should be considered. With this in mind, the ULE was set to 841.9 Mhz, and the repump was scanned around. Periodically, the repump was turned off to get a background. For each repump position, the counts for the probe region, defined as anywhere that the counts were greater than 600, were collected and had their mean and standard deviation taken. This was taken as the mean and standard deviation of the measurement. The mean and standard deviations as a function of Repump Frequency can be seen in Figure 4.6.

The background data, where the repump was off and no trapping should have been seen,

Figure 4.6: Results of Radium 223 Scan

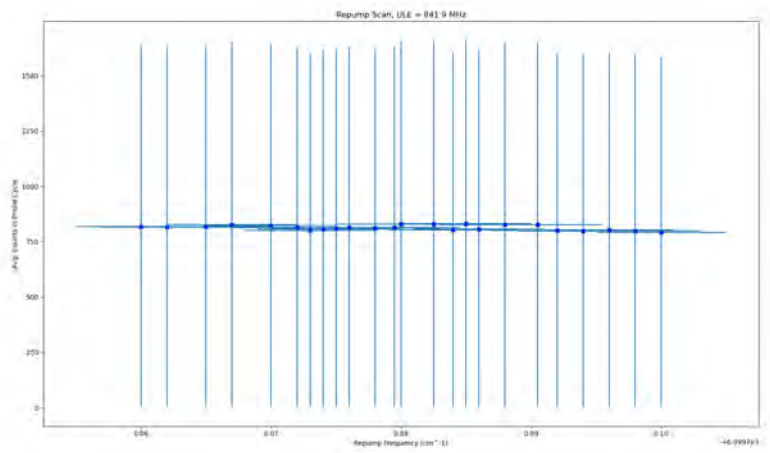

looked like Figure 4.7

The conclusion was that, at this ULE frequency and these repump frequencies, Ra-223 trapping was not achieved.

4.9 Future Work

In the future, when loading Radium-223 into the oven, having the MOT ready to trap Radium-226 to verify it's working would be ideal. Radium-223 ended up also in short supply, and as a result focus was switched back to Radium-225.

Figure 4.7: Trapping Data with Repump Off

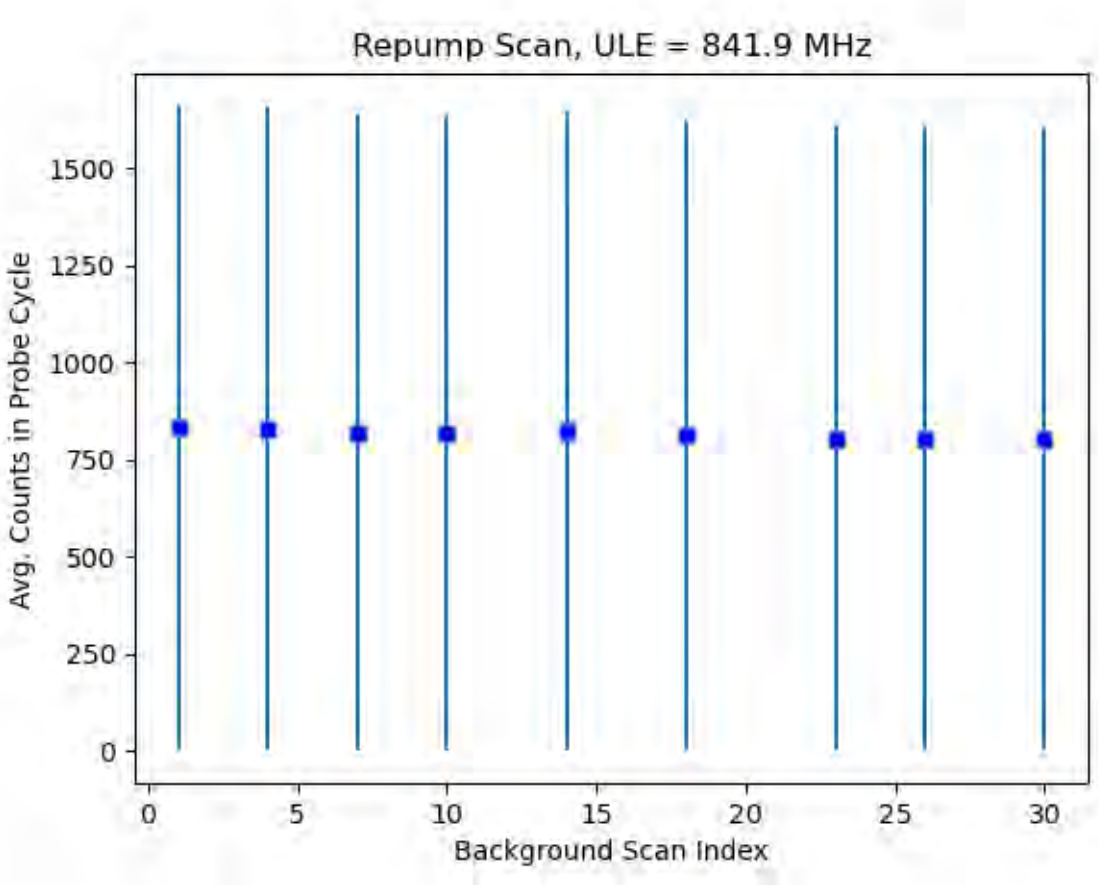

Chapter 5. Calculation of Frequency Shifts Associated with the Laser Trap

5.1 Effect of Laser Trapping on EDM measurements

The precision needed for the Radium EDM experiment requires extreme attention to detail for systematic effects. Any effect that might cause a shift in Larmor precession frequency apart from an EDM needs to be carefully studied and characterized, so that the sensitivity to the EDM is dominated by statistical uncertainty instead. The more these systematics can be controlled and suppressed, the better. One of the potential sources of systematic uncertainty comes from the interaction of the atoms being held in an ODT, and having a static E field applied. For Radium-225, the effect this has can be broken down into two parts: the vector shift, and the Stark shift[48]. For Radium-223, an additional tensor shift is added. To characterize their associated systematic uncertainties, atomic calculations are required. An overview of these ongoing caluclations will now be given.

5.1.1 Vector Shift

When atoms are trapped in an ODT, there is an added interaction expressed by the Hamiltonian

$$H' = e\mathbf{E} \cdot \sum_i \mathbf{r_i} \tag{5.1}$$

where $\mathbf{E} = \frac{E_0}{2}(\hat{\epsilon}e^{-i\omega t} + \hat{\epsilon}^* e^{i\omega t})$. To first order in time dependent perturbation theory,

this results in a vector shift that looks like:

$$\Delta E = \frac{-e^2 E_0^2}{4\hbar}\Sigma_{J',F',m'}[\frac{\langle J',I,F',M'|\epsilon\cdot r|J,I,F,M\rangle\langle J,I,F,M|\epsilon^*\cdot r|J',I,F',M'\rangle}{\omega_{J'}-\omega} + \frac{\langle J',I,F',M'|\epsilon^*\cdot r|J,I,F,M\rangle\langle J,I,F,M|\epsilon\cdot r|J',I,F',M'\rangle}{\omega_{J'}+\omega}] \tag{5.2}$$

This ΔE has a scalar shift component, which is not dependent on the m_F sublevel, and so has no effect on our experiment - Our experiment is sensitive to *changes* in Larmor Precession frequency, not the value of the frequency itself. However, it also gives rise to a vector shift - a term that is linear in the m_F sublevel. The depenency of this vector shift looks something like:

$$\Delta\nu = \nu_V(|\epsilon_L|^2 - |\epsilon_R|^2)m_F\cos\theta \tag{5.3}$$

where θ is the angle between the ODT propagation and the spin quantization axis, ϵ_L and ϵ_R are the degrees of left and right circular polarization, and ν_V is a term dependent upon power (Through the E_0^2 term) and ODT frequency - it is here that the vector shift can cause problems. Any power fluctuation correlated with the applied E field might cause a shift in energy between m_F states proportional to the E field. This would cause a shift in the Larmor Precession frequency between applied E fields that could not be attributed to a non-zero EDM. Thankfully, there are methods of suppression: For one, the ODT is $> 99\%$ linearly polarized - this introduces a suppression of two orders of magnitude. For another, since the ODT is aligned perpendicular to the spin quantization axis- the same axis as the larmor spin precession - there is another suppression factor of 0.1. Ultimately, the false EDM

signal that would be created can be characterized by:

$$d_{false} = \Delta\nu_{1/2}\frac{h}{2E}\frac{\Delta P}{P_0} \tag{5.4}$$

where E is the electric field strength, $\nu_{1/2}$ is the vector shift, and $\frac{\Delta P}{P_0}$ is the fractional difference in holding beam power between different E field directions. The power is continuously monitored, and a 1 σ confidence interval upper limit can be placed on $\frac{\Delta P}{P_0}$ to be 8×10^{-5}. Finally, the calculated $\nu_{1/2}$ is found to be 50 Hz. This all combines to give a 1σ uncertainty of $6 \times 10^{-26} e \cdot cm$ for Ra-225.

5.1.2 Tensor Shift

The tensor shift arises from the next order of perturbation theory, and includes a mixing term with the hyperfine structure. This also contributes to the systematic related to ODT holding beam power correlation with E field. The equation associated with this is:

$$\Delta E = \frac{e^2 E_0^2}{4\hbar} \sum_{J',J",F',M'} \frac{\langle J', I, F', M'|\epsilon \cdot \mathbf{r}|J, I, F, M\rangle\langle J, I, F, M|\epsilon^* \cdot \mathbf{r}|J", I, F', M'\rangle}{(\omega_{J'} - \omega)(\omega_{J"} - \omega)} \tag{5.5}$$

$$\times\langle J", I, F', M'|W|J', I, F', M'\rangle + c.r.$$

where c.r. is an additional counter-rotating term. This results in a tensor shift looking like:

$$\Delta\nu = \nu_T(F)(3\cos^2\phi - 1)m_F^2 \tag{5.6}$$

where ϕ is the angle between the direction of the linearly polarized electric field and the spin quantization axis, and $\nu_T(F)$ is a function of the ODT power and F sublevel. This shift only arises for nuclei with I > 1. It thus is non-existent for Ra-225, though it does have an effect in Radium-223, albeit with a shift that is predicted to be much smaller. Like the vector shift, the false EDM signal this would give rise to would be

$$2Ed_{false} = \Delta E_{M=3/2,1/2}\frac{\Delta P}{P_0} \tag{5.7}$$

So,

$$d_{false} = \Delta\nu_{M=3/2,1/2}\frac{h}{2E}\frac{\Delta P}{P_0} \tag{5.8}$$

Note that this effect is not minimized when the electric field and spin quantization axis are perpendicular, but rather at a magic angle $\phi = cos^{-}1(\sqrt{\frac{1}{3}})$

5.1.3 Parity Mixing Effect

The most dangerous effect outlined in [48] is the parity mixing effect. This arises from a third-order mixing effect between the static E field and the E field of the ODT holding beam. The energy form for this equation looks like:

$$\Delta E = \frac{e^2 \mu_B E_0^2 E_s}{4\hbar^2}$$

$$\times \sum_{J',J'',M',M''} [\frac{\langle J', M'|\epsilon \cdot r|J, M\rangle\langle J'', M'', |b^* \cdot (L+2S)|J', M'\rangle\langle J, M|\epsilon_s \cdot r|J'', M''\rangle}{(\omega_{J'} - \omega)(\omega_{J"} - \omega)} \quad (5.9)$$

$$+\frac{\langle J, M'|b \cdot (L+2S)|J, M\rangle\langle J', M'|\epsilon^* \cdot r|JM'\rangle\langle J, M|\epsilon_s \cdot r|J', M'\rangle}{\omega_{J'}(\omega_{J'} - \omega)}] + perm. + c.r.$$

where perm. is the other permutations of the interactions. A picture of those permutation is given here:

Figure 5.1: Various Permutations of Interactions[3]

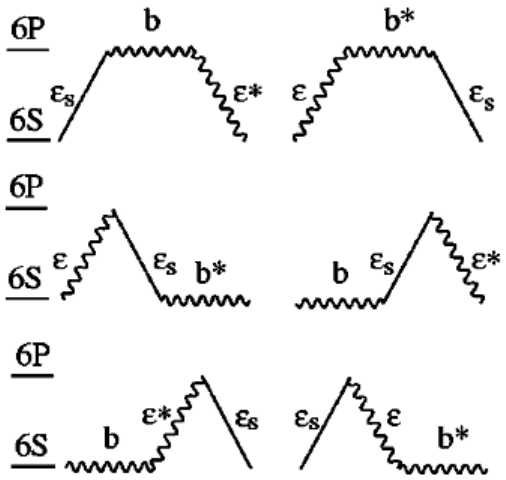

The interactions with ϵ indicate electric dipole transitions induced by the trapping beam, the b interactions indicate magnetic dipole moments induced by the trapping field, and the ϵ_s terms indicate mixing by the static electric field. This happens because static electric field causes states to mix, and some of these have different parities. Normally, since the electric

dipole (E1) transition flips parity and the magnetic dipole (M1) transition conserves it, two states coupled with an E1 transition cannot be coupled back with an M1 transition. With the addition of the static E field, one of the states coupled with E1 can be mixed with a state that can couple to M1. This causes mixing of different parity states. There is also an additional effect that arises from the electric quadrupole (E2) interaction, which has the same parity rule as M1. A good way to look at this is to look at the interactions:

$$H_{E1} = e\mathbf{r} \cdot \mathbf{E} = eyE_0 \cos\omega t \tag{5.10}$$

$$H_{M1} = \frac{e}{2mc}(\mathbf{L} + 2\mathbf{S}) \cdot \mathbf{B} = \frac{e\hbar}{2mc}(L_z + 2S_z)E_0 \cos\omega t \tag{5.11}$$

$$H_{E2} = \frac{e}{6}(3x_i x_j - \delta_{ij} r^2)\frac{\delta E_i}{\delta x_j} = \frac{e\omega}{2c} xyE_0 \sin\omega t \tag{5.12}$$

This causes the multipole amplitudes to be given by:

$$E1 = e\langle \psi_f^0 | E_0 y | \psi_i^0 \rangle \tag{5.13}$$

$$M1 = \frac{e^2 E_s E_0 \hbar}{4mc} \sum_n \frac{\langle \phi_f^0 | y | \phi_n^0 \rangle \langle \phi_n^0 | L_z + 2S_z | \phi_i^0 \rangle}{W_f - W_n} + \frac{\langle \phi_f^0 | L_z + 2S_z | \phi_n^0 \rangle \langle \phi_n^0 | y | \phi_i^0 \rangle}{W_i - W_n} \tag{5.14}$$

$$E2 = \frac{ie^2 \omega E_s E_0}{4c} \sum_n \frac{\langle \phi_f^0 | y | \phi_n^0 \rangle \langle \phi_n^0 | xy | \phi_i^0 \rangle}{W_f - W_n} - \frac{\langle \phi_f^0 | xy | \phi_n^0 \rangle \langle \phi_n^0 | y | \phi_i^0 \rangle}{W_i - W_n} \tag{5.15}$$

Notice how the electric dipole transition couples states ψ_f and ψ_i, which would be a

forbidden transition for the magnetic dipole moment. The stark effect mixing due to the static electric field allows for the transition to still happen.

The Stark frequency shift depends on 4 vectors, and the shift this causes has a dependence like:

$$\Delta\nu_V = \nu_1(\hat{b}\cdot\hat{\sigma})(\hat{\epsilon}\cdot\hat{\epsilon_s}) + \nu_2(\hat{b}\cdot\hat{\epsilon_s})(\hat{\epsilon}\cdot\hat{\sigma}) \tag{5.16}$$

where $\hat{\epsilon}$ is the ODT electric field orientation, $\hat{\sigma}$ is the spin polarization axis, $\hat{\epsilon_\mathbf{s}}$ is the static electric field direction, and $\hat{\mathbf{b}}$ is the ODT magnetic field orientation. Note that in our experiment, ϵ_s and σ are in the same direction. The best way to thus orient the ODT is so that either ϵ or b are perpendicular, in order to suppress at least one of the dot products in both terms of $\Delta\nu_V$.

The single E_s term is scary, since this stark shift does indeed cause a false EDM signature. When the direction of E_s is flipped, it causes a shift in the energy *depending on the direction*.

In addition to the linear effect of E_s, which can cause a false EDM signature, there is also a dependence on the power of the ODT laser. This only comes up if there's some kind of correlation between the direction of E field and the ODT power, though. In addition, it allows for measurement of this false EDM effect. If there's a Larmor frequency shift observed that is dependent on both the electric field strength AND the ODT holding beam power, then the values of these ν_1 and ν_2 can in fact be experimentally observed, as was done in an EDM experiment with Ytterbium-171 in China[4]. In this experiment, the angle θ determining the polarization of the ODT was varied, and the resulting false EDM signal was plotted:

Figure 5.2: False EDM Signal Created by Parity Mixing Effect in Yb-171[4]

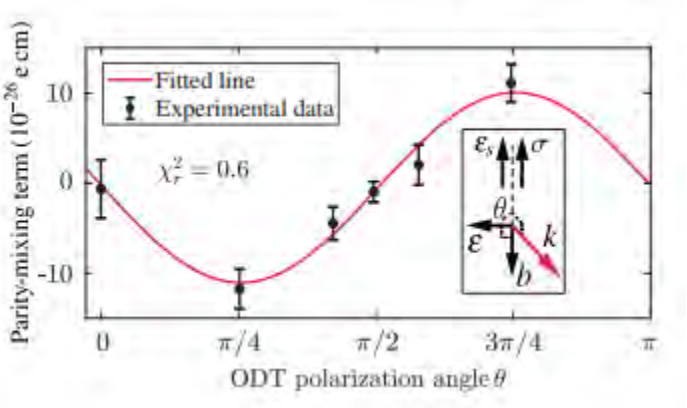

This effect for Radium was calculated out in [36], and gives a systematic uncertainty of $(\hat{b} \cdot \hat{\sigma})(\hat{\epsilon} \cdot \hat{\epsilon_s}) \leq 0.03$ and $(\hat{b} \cdot \hat{\epsilon_s})(\hat{\epsilon} \cdot \hat{\sigma}) \leq 0.1$ which, combined with the values calculated for ν_1 and ν_2, give a 1σ systematic uncertainty of $6 \times 10^{-26} e \cdot cm$. This is the calculated false EDM caused by the phase shift in Larmor precession frequency that would be caused by this effect. [36] contains a brief description of this calculation.

5.2 Reproduction of Published Calcultions

[48] has been used as the basis of calculations of the effects of static electric fields on the energy levels of atoms held in an optical dipole trap. Effort was put into reproducing these calculations, so that they could then be used as the basis for calculating the energy shifts in Ra-225 and Ra-223.

5.2.1 Laser Power Dependency Reproduction

To begin, the paper calculates the laser power necessary to trap atoms with a trap depth of $100\mu K$ as a function of the laser wavelength. For a Gaussian beam with a beam width of

w_0, the radial intensity of the beam as a function of the distance from its center is

$$I(r) = I_0 e^{2(\frac{r}{w_0})^2} \tag{5.17}$$

Where I_0 is the intensity of the beam at its center, and w_0 is the beam width at its focal point. By performing a polar integral, the total power of the beam can be determined:

$$P_0 = \int_0^{2\pi} \int_0^{\infty} I_0 e^{2(\frac{r}{w_0})^2} r dr d\phi = \frac{\pi}{2} I_0 w_0^2 \tag{5.18}$$

I_0 is a function of the electric field strength at the center of the trap, related by:

$$I_0 = \frac{|E_0|^2}{2\eta} \tag{5.19}$$

where η is the impedance of the medium, in this case free space.

Combining gives

$$P_0 = \frac{\pi w_0^2 |E_0|^2}{4\eta} \tag{5.20}$$

In order to get rid of the troublesome factor of π in this equation, Gaussian units must be used. In these units,

$$\eta = \frac{4\pi}{c} \tag{5.21}$$

So, this gives

$$P_0 = \frac{w_0^2 E_0^2 c}{16} \tag{5.22}$$

which is the formula given, but not derived, in the article for the total beam power as a function of the beam width and electric field strength at the center, in Gaussian units.

The formula given in [48] for the energy depth of the optical dipole trap (ODT) is

$$U = -\frac{e^2 E_0^2}{4m}[\sum_{J'} \frac{f_{J'}}{\omega_{J'}^2 - \omega^2} + \int_{\omega_I}^{\inf} \frac{(df/d\omega')d\omega'}{(\omega' - \omega_{J'})^2 - \omega^2}] \tag{5.23}$$

[48] specifies only two states for Cs and Hg that are really necessary for a good calculation. For Cs, these states are $6P_{1/2}$ and $6P_{3/2}$. It gives the oscillator strengths for both of these states, and the energy levels can be found on the NIST website:

Table 5.1: Energy Levels of Excited States Used for Vector Shift Calculation

Element	J'	$\omega_{J'}(cm^{-1})$	$f_{J'}$
Cs	1/2	11178.2686	.35
Cs	3/2	11732.3079	.72
Hg	1/2	54068.781	1.2
Hg	3/2	39412.300	.025

The formula then effectively becomes

$$U = -\frac{e^2 E_0^2}{4m} \sum_{J'=\{1/2,3/2\}} \frac{f_{J'}}{\omega_{J'}^2 - \omega^2} = k_b(-100\mu K) \tag{5.24}$$

note that U is the energy of the trap, so U is negative, meaning the negative has to be taken of the trap depth.

Figure 1 in [48] is a plot of the required ODT laser power versus frequency. The total beam power is a function of E_0^2, and E_0^2 can be found with a rearranging of the above formula:

$$E_0^2 = -\frac{4mU}{e^2 \sum_{J'}} \frac{f_{J'}}{\omega_{J'}^2 - \omega^2} \tag{5.25}$$

By finding E_0^2 as a function of ω, and then the resulting power as a function of ω, Figure 1 can be reproduced for both Hg and Cs:

Figure 5.3: Cesium ODT Power Requirement Reproduction

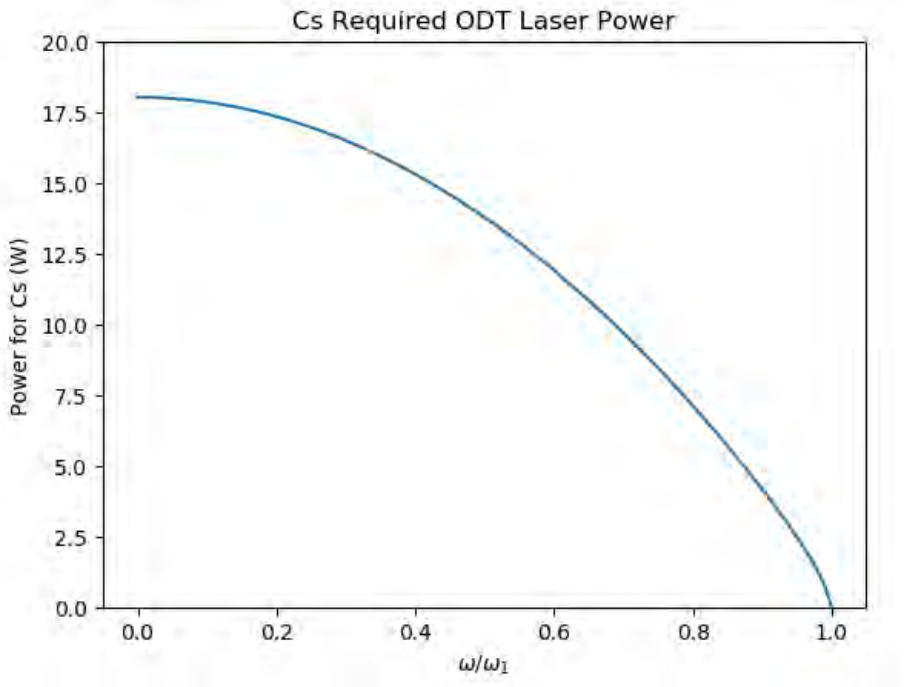

The reproduction of these plots is necessary for the calculation of the vector and tensor shifts.

5.3 Vector Shift Reproduction

In order to reproduce the plots it [48], time dependent perturbation theory is necessary. A derivation is now given.

Figure 5.4: Mercury ODT Power Requirement Reproduction

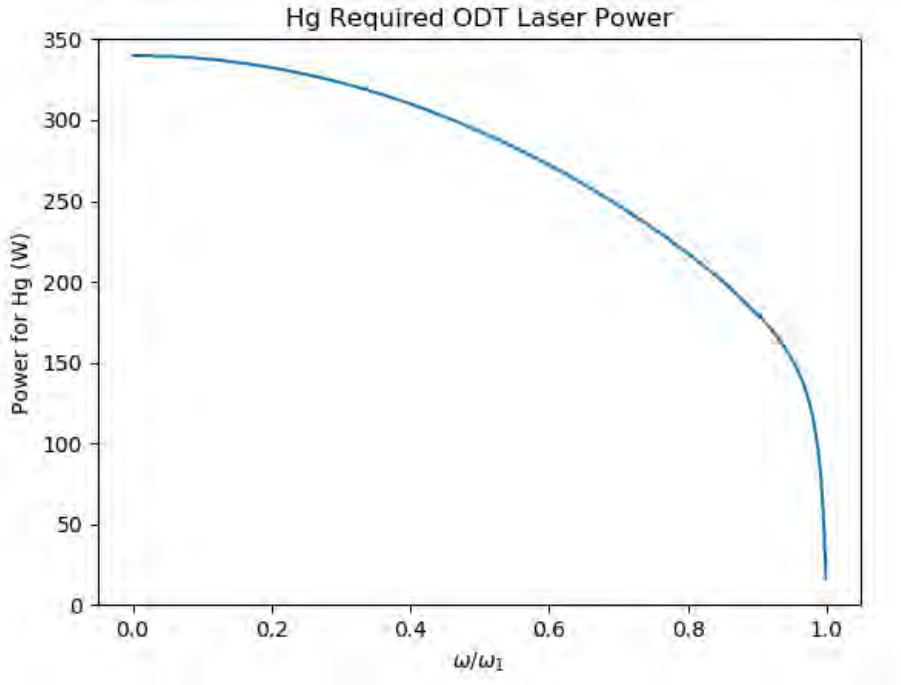

5.3.1 Energy Shift Derivation from Time Dependent Perturbation Theory

The unperturbed eigenstates are the normal $|J, I, F, M\rangle$ hyperfine states for the unperturbed Hamiltonian, which form an orthonormal basis:

$$\langle J', I, F', M'|J, I, F, M\rangle = \delta_{J'J}\delta_{F'F}\delta_{M'M} \tag{5.26}$$

To this system, add an energy perturbation:

$$H'(t) = e\mathbf{E}(t) \cdot \mathbf{r} \tag{5.27}$$

where

$$\mathbf{E}(t) = \frac{E_0}{2}(\hat{\epsilon}e^{-i\omega t} + \hat{\epsilon}^* e^{i\omega t}) \tag{5.28}$$

The full Hamiltonian is:

$$\hat{H} = \hat{H}_0 + \hat{H}'(t) \tag{5.29}$$

where $\hat{H}_0$ is the base Hamiltonian of the atom.

The eigenvectors of $\hat{H}_0$ are a set of orthonormal eigenvectors $|i\rangle$ with eigenvalues

$$\hat{H}_0|i\rangle = E_i|i\rangle \tag{5.30}$$

The total wave function for the Hamiltonian is:

$$\Psi_i(t) = c_i(t)|i\rangle e^{-\iota E_i \frac{t}{\hbar}} + \sum_{k \neq i} c_k(t)|k\rangle e^{-\iota E_k \frac{t}{\hbar}} \tag{5.31}$$

where, to first order, $c_i(0) = 1$, $c_k(0) = 0$

using time dependent perturbation theory,

$$\hat{H}\Psi(t) = \iota\hbar\frac{\delta\Psi}{\delta t} \tag{5.32}$$

$$\hat{H}_0\Psi(t) + \hat{H}'\Psi(t) = \iota\hbar\frac{\delta\Psi}{\delta t} \tag{5.33}$$

expanding,

$$c_i(t)\hat{H}_0|i\rangle e^{-\iota E_i\frac{t}{\hbar}} + \sum_{k\neq i} c_k(t)\hat{H}_0|k\rangle e^{-\iota E_k\frac{t}{\hbar}}$$

$$+c_i(t)\hat{H}'|i\rangle e^{-\iota E_i\frac{t}{\hbar}} + \sum_{k\neq i} c_k t\hat{H}'|k\rangle e^{-\iota E_k\frac{t}{\hbar}} \tag{5.34}$$

$$= \iota\hbar(\dot{c}_i(t)|i\rangle e^{-\iota E_i\frac{t}{\hbar}} + \sum_{k\neq i} \dot{c}_k(t)|k\rangle e^{\iota E_k\frac{t}{\hbar}}$$

$$+c_i(t)\frac{-\iota}{\hbar}E_i|i\rangle e^{-\iota E_i\frac{t}{\hbar}} + \sum_{k\neq i} c_k(t)\frac{-\iota}{\hbar}E_k|k\rangle e^{-\iota E_k\frac{t}{\hbar}})$$

1489 Subtract the $\hat{H}_0$ terms:

$$c_i(t)\hat{H}'|i\rangle e^{-\iota E_i\frac{t}{\hbar}} + \sum_{k\neq i} c_k t\hat{H}'|k\rangle e^{-\iota E_k\frac{t}{\hbar}} = \iota\hbar\dot{c}_i(t)|i\rangle e^{-\iota E_i\frac{t}{\hbar}} + \iota\hbar\sum_{k\neq i}\dot{c}_k(t)|k\rangle e^{-\iota E_k\frac{t}{\hbar}} \tag{5.35}$$

1490 plug in the first order $c_i(0) = 1$, $c_k(0) = 0$:

$$\hat{H}'|i\rangle e^{-\iota E_i\frac{t}{\hbar}} = \iota\hbar\dot{c}_i(t)|i\rangle e^{-\iota E_i\frac{t}{\hbar}} + \iota\hbar\sum_{k\neq i}\dot{c}_k(t)|k\rangle e^{-\iota E_k\frac{t}{\hbar}} \tag{5.36}$$

1491 Thus,

$$\langle i|\hat{H}'|i\rangle e^{-\iota E_i\frac{t}{\hbar}} = \iota\hbar\dot{c}_i(t)e^{-\iota E_i\frac{t}{\hbar}} \tag{5.37}$$

1492 Thus,

$$\dot{c}_i(t) = \frac{\langle i|\hat{H}'|i\rangle}{\iota\hbar} \tag{5.38}$$

for $k \neq i$,

$$\langle j|\hat{H}'|i\rangle e^{-\iota E_i \frac{t}{\hbar}} = \iota\hbar\dot{c}_j e^{-\iota E_j \frac{t}{\hbar}} \tag{5.39}$$

therefore,

$$\dot{c}_j = \frac{1}{\iota\hbar}\langle j|\hat{H}'|i\rangle e^{\iota(E_j - E_i)\frac{t}{\hbar}} \tag{5.40}$$

Now, integrate to find the c_i:

For $\hat{H}' = e\overrightarrow{E} \cdot \overrightarrow{r}$,

$$\langle i|\hat{H}'|i\rangle = 0 \tag{5.41}$$

therefore,

$$\frac{dc_i(t')}{dt'} = 0 \tag{5.42}$$

$$dc_i(t') = 0 \times dt' \tag{5.43}$$

$$\int_{c_i(0)}^{c_i(t)} dc_i(t) = \int_0^t 0dt' \tag{5.44}$$

$$c_i(t) - c_i(0) = 0 \tag{5.45}$$

therefore,

$$c_i(t) = c_i(0) = 1 \tag{5.46}$$

to this first order.

For $k \neq i$,

$$\frac{dc_k(t')}{dt'} = \frac{1}{\iota\hbar}\langle j|\hat{H}'|i\rangle e^{\iota(E_k - E_i)\frac{t'}{\hbar}} \tag{5.47}$$

$$\int_{c_k(0)}^{c_k(t)} dc_j(t') = \frac{1}{\iota\hbar}\int_0^t \langle j|\hat{H}'(t')|i\rangle e^{\iota(E_k - E_i)\frac{t'}{\hbar}} dt' \tag{5.48}$$

since $c_k(0) = 0$,

$$c_k(t) = \frac{1}{\iota\hbar}\int_0^t \langle k|\hat{H}'(t')|i\rangle e^{\iota(E_k - E_i)\frac{t'}{\hbar}} dt' \tag{5.49}$$

Now, we plug these values into the equation again

$$\begin{aligned}\hat{H}'|i\rangle e^{-\iota E_i\frac{t}{\hbar}} + \sum_{k\neq i}\frac{1}{\iota\hbar}\int_0^t \langle k|\hat{H}'(t')|i\rangle e^{\iota(E_k - E_i)\frac{t'}{\hbar}} dt'\hat{H}'|k\rangle e^{-\iota E_k\frac{t}{\hbar}} \\ = \iota\hbar\dot{c}_i(t)|i\rangle e^{-\iota E_i\frac{t}{\hbar}} + \iota\hbar\sum_{k\neq i}\dot{c}_k(t)|k\rangle e^{-\iota E_k\frac{t}{\hbar}}\end{aligned} \tag{5.50}$$

once again, project onto $\langle i|$

$$\iota\hbar\dot{c}_i e^{-\iota E_i\frac{t}{\hbar}} = \langle i|\hat{H}'|i\rangle e^{-\iota E_i\frac{t}{\hbar}} + \sum_{k\neq i}\frac{1}{\iota\hbar}\int_0^t \langle k|\hat{H}'(t')|i\rangle e^{\iota(E_k-E_i)\frac{t'}{\hbar}}dt'\langle i|\hat{H}'|k\rangle e^{-\iota E_k\frac{t}{\hbar}} \quad (5.51)$$

1504 therefore,

$$\dot{c}_i = \frac{\langle i|\hat{H}'|i\rangle}{\iota\hbar} + \sum_{k\neq i}\frac{-1}{\hbar^2}\int_0^t \langle k|\hat{H}'(t')|i\rangle e^{\iota(E_k-E_i)\frac{t'}{\hbar}}dt'\langle i|\hat{H}'|k\rangle e^{\iota(E_i-E_k)\frac{t}{\hbar}} \quad (5.52)$$

1505 For $H'(t) = e\overrightarrow{E}\cdot\overrightarrow{r}$, $\langle i|H'|i\rangle = 0$

1506 so,

$$\frac{dc_i(t')}{dt'} = \sum_{k\neq i}\frac{-1}{\hbar^2}\int_0^{t'} \langle k|\hat{H}'(t")|i\rangle e^{\iota(E_k-E_i)\frac{t"}{\hbar}}dt"\langle i|\hat{H}'|k\rangle e^{\iota(E_i-E_k)\frac{t'}{\hbar}} \quad (5.53)$$

$$\int_{c_i(0)}^{c_i(t)} dc_i = \sum_{k\neq i}\frac{-1}{\hbar^2}\int_0^t\int_0^{t'} \langle k|\hat{H}'(t")|i\rangle e^{\iota(E_k-E_i)\frac{t"}{\hbar}}dt"\langle i|\hat{H}'(t')|k\rangle e^{\iota(E_i-E_k)\frac{t'}{\hbar}}dt' \quad (5.54)$$

1507 thus,

$$c_i(t) - 1 = \frac{-1}{\hbar^2}\sum_{k\neq i}\int_0^t\int_0^{t'} \langle k|\hat{H}'(t")|i\rangle e^{\iota(E_k-E_i)\frac{t"}{\hbar}}dt"\langle i|\hat{H}'(t')|k\rangle e^{\iota(E_i-E_k)\frac{t'}{\hbar}}dt' \quad (5.55)$$

1508 and,

$$c_i(t) = 1 - \frac{1}{\hbar^2}\sum_{k\neq i}\int_0^t \int_0^{t'} \langle k|\hat{H}'(t")|i\rangle e^{\iota(E_k-E_i)\frac{t"}{\hbar}}\,dt" \langle i|\hat{H}'(t')|k\rangle e^{\iota(E_i-E_k)\frac{t'}{\hbar}}\,dt' \tag{5.56}$$

Now, take a look at the actual form of $\hat{H}'(t)$:

$$\int_0^{t'} \langle k|\hat{H}'(t'')|i\rangle e^{\iota(E_k-E_i)\frac{t''}{\hbar}}\,dt''$$

$$= \frac{eE_0}{2}\int_0^{t'} (\langle k|\hat{\epsilon}e^{-\iota\omega t"}\cdot\overrightarrow{r}|i\rangle + \langle k|\hat{\epsilon}^* e^{\iota\omega t"}\cdot\overrightarrow{r}|i\rangle)e^{\iota(E_k-E_i)\frac{t"}{\hbar}}\,dt''$$

$$= \frac{eE_0}{2}(\int_0^{t'} \langle k|\hat{\epsilon}\cdot\overrightarrow{r}|i\rangle e^{\iota(E_k-E_i-\omega\hbar)\frac{t"}{\hbar}}\,dt" + \int_0^{t'} \langle k|\hat{\epsilon}^*\cdot\overrightarrow{r}|i\rangle e^{\iota(E_k+\omega\hbar-E_i)\frac{t"}{\hbar}}\,dt") \tag{5.57}$$

$$= \frac{eE_0}{2}(\langle k|\hat{\epsilon}\cdot\overrightarrow{r}|i\rangle\frac{e^{\iota(E_k-E_i-\omega\hbar)\frac{t'}{\hbar}}-1}{\frac{\iota}{\hbar}(E_k-E_i-\omega\hbar)} + \langle k|\hat{\epsilon}^*\cdot\overrightarrow{r}|i\rangle\frac{e^{\iota(E_k-E_i+\omega\hbar)\frac{t'}{\hbar}}-1}{\frac{\iota}{\hbar}(E_k-E_i+\omega\hbar)})$$

Therefore,

$$c_i(t) - 1 = \frac{-1}{\hbar^2} \sum_{k \neq i} \int_0^t \frac{eE_0}{2} (\langle k|\hat{\epsilon} \cdot \overrightarrow{r}|i\rangle \frac{e^{\iota(E_k - E_i - \omega\hbar)\frac{t'}{\hbar}} - 1}{\frac{\iota}{\hbar}(E_k - E_i - \omega\hbar)}$$

$$+ \langle k|\hat{\epsilon}^* \cdot \overrightarrow{r}|i\rangle \frac{e^{\iota(E_k - E_i + \omega\hbar)\frac{t'}{\hbar}} - 1}{\frac{\iota}{\hbar}(E_k - E_i + \omega\hbar)}) \tag{5.58}$$

$$\times \frac{eE_0}{2} (\langle i|\hat{\epsilon} \cdot \overrightarrow{r}|k\rangle e^{\iota(E_i - E_k - \omega\hbar)\frac{t'}{\hbar}}$$

$$+ \langle i|\hat{\epsilon}^* \cdot \overrightarrow{r}|k\rangle e^{\iota(E_i + \omega\hbar - E_k)\frac{t'}{\hbar}}) dt'$$

1511 Thus,

$$c_i(t) = 1 - \frac{e^2 E_0^2}{4\hbar^2} \int_0^t (\langle k|\hat{\epsilon} \cdot \overrightarrow{r}|i\rangle \langle i|\hat{\epsilon} \cdot \overrightarrow{r}|k\rangle \frac{e^{-2\iota\omega t'} - e^{\iota(E_i - E_k - \omega\hbar)\frac{t'}{\hbar}}}{\frac{\iota}{\hbar}(E_k - E_i - \omega\hbar)}$$

$$+ \langle k|\hat{\epsilon} \cdot \overrightarrow{r}|i\rangle \langle i|\hat{\epsilon}^* \cdot \overrightarrow{r}|k\rangle \frac{1 - e^{\iota(E_i + \omega\hbar - E_k)\frac{t'}{\hbar}}}{\frac{\iota}{\hbar}(E_k - E_i - \omega\hbar)}$$

$$+ \langle k|\hat{\epsilon}^* \cdot \overrightarrow{r}|i\rangle \langle i|\hat{\epsilon} \cdot \overrightarrow{r}|k\rangle \frac{1 - e^{\iota(E_i - \omega\hbar - E_k)\frac{t'}{\hbar}}}{\frac{\iota}{\hbar}(E_k - E_i + \omega\hbar)} \tag{5.59}$$

$$+ \langle k|\hat{\epsilon}^* \cdot \overrightarrow{r}|i\rangle \langle i|\hat{\epsilon}^* \cdot \overrightarrow{r}|k\rangle \frac{e^{2\iota\omega t'} - e^{\iota(E_i + \omega\hbar - E_k)\frac{t'}{\hbar}}}{\frac{\iota}{\hbar}(E_k - E_i + \omega\hbar)}) dt'$$

Now consider what exactly is ΔE:

$$\Delta E = \langle \Psi_i | \hat{H} - \hat{H}_0 | \Psi \rangle = \langle i | \hat{H} | \Psi_i \rangle - \langle i | \hat{H}_0 | \Psi \rangle \tag{5.60}$$

$$\begin{aligned} \hat{H}|\Psi\rangle = \iota\hbar\frac{\delta\Psi}{\delta t} = \iota\hbar\dot{c}_i(t)|i\rangle e^{-\iota E_i \frac{t}{\hbar}} + c_i(t)E_i|i\rangle e^{-\iota E_i \frac{t}{\hbar}} \\ + \sum_{k\neq i} \iota\hbar\dot{c}_k(t)|k\rangle e^{-\iota E_k \frac{t}{\hbar}} + c_k(t)E_k|k\rangle e^{-\iota E_k \frac{t}{\hbar}} \end{aligned} \tag{5.61}$$

since

$$\hat{H}_0|\Psi\rangle = c_i(t)E_i|i\rangle e^{-\iota E_i \frac{t}{\hbar}} + c_k(t)E_k|k\rangle e^{-\iota E_k \frac{t}{\hbar}} \tag{5.62}$$

this means

$$(\hat{H} - \hat{H}_0)|\Psi\rangle = \iota\hbar(\dot{c}_i(t)|i\rangle e^{-\iota E_i \frac{t}{\hbar}} + \sum_{k\neq i} \dot{c}_k(t)|k\rangle e^{-\iota E_k \frac{t}{\hbar}}) \tag{5.63}$$

thus,

$$\langle \Psi_i | \hat{H} - \hat{H}_0 | \Psi \rangle = e^{\iota E_i \frac{t}{\hbar}} \langle i | \iota\hbar\dot{c}_i(t)|i\rangle e^{-\iota E_i \frac{t}{\hbar}} = \iota\hbar\dot{c}_i(t) \tag{5.64}$$

using the 2nd fundamental theorem of calculus,

$$\Delta E = \iota\hbar(\frac{-1}{\hbar^2}\sum_{k\neq i}\frac{e^2E_0^2}{4}(\langle k|\hat{\epsilon}\cdot\overrightarrow{r}|i\rangle\langle i|\hat{\epsilon}\cdot\overrightarrow{r}|k\rangle\frac{e^{-2\iota\omega t}-e^{\iota(E_i-E_k-\omega\hbar)\frac{t}{\hbar}}}{\frac{\iota}{\hbar}(E_k-E_i-\omega\hbar)}$$

$$+\langle k|\hat{\epsilon}\cdot\overrightarrow{r}|i\rangle\langle i|\hat{\epsilon}^*\cdot\overrightarrow{r}|k\rangle\frac{1-e^{\iota(E_i+\omega\hbar-E_k)\frac{t}{\hbar}}}{\frac{\iota}{\hbar}(E_k-E_i-\omega\hbar)} \tag{5.65}$$

$$+\langle k|\hat{\epsilon}^*\cdot\overrightarrow{r}|i\rangle\langle i|\hat{\epsilon}\cdot\overrightarrow{r}|k\rangle\frac{1-e^{\iota(E_i-\omega\hbar-E_k)\frac{t}{\hbar}}}{\frac{\iota}{\hbar}(E_k-E_i+\omega\hbar)}$$

$$+\langle k|\hat{\epsilon}^*\cdot\overrightarrow{r}|i\rangle\langle i|\hat{\epsilon}^*\cdot\overrightarrow{r}|k\rangle\frac{e^{2\iota\omega t}-e^{\iota(E_i+\omega\hbar-E_k)\frac{t}{\hbar}}}{\frac{\iota}{\hbar}(E_k-E_i+\omega\hbar)})$$

1517 Anything of the form $e^{\iota\omega t}$ time averages out to zero. So,

$$\Delta E = \iota\hbar(\frac{-1}{\hbar^2}\sum_{k\neq i}\frac{e^2E_0^2}{4}\frac{\hbar}{\iota}(\frac{\langle k|\hat{\epsilon}\cdot\overrightarrow{r}|i\rangle\langle i|\hat{\epsilon}^*\cdot\overrightarrow{r}|k\rangle}{E_k-E_i-\omega\hbar}+\frac{\langle k|\hat{\epsilon}^*\cdot\overrightarrow{r}|i\rangle\langle i|\hat{\epsilon}\cdot\overrightarrow{r}|k\rangle}{E_k-E_i+\omega\hbar}) \tag{5.66}$$

1518 Thus,

$$\Delta E = -\frac{e^2E_0^2}{4\hbar}\sum_{k\neq i}(\frac{\langle k|\hat{\epsilon}\cdot\overrightarrow{r}|i\rangle\langle i|\hat{\epsilon}^*\cdot\overrightarrow{r}|k\rangle}{\omega_{ki}-\omega}+\frac{\langle k|\hat{\epsilon}^*\cdot\overrightarrow{r}|i\rangle\langle i|\hat{\epsilon}\cdot\overrightarrow{r}|k\rangle}{\omega_{ki}+\omega}) \tag{5.67}$$

1519 where $\omega_{ki}=\frac{E_k-E_i}{\hbar}$. Note that this is the same as equation 11 given in [48] for the energy

1520 shift.

5.3.2 Calculation of Vector Shift for Cs-133

In order actually get numeric values for the energy shift, the expression

$$\Delta E = \frac{-e^2 E_0^2}{4\hbar}\Sigma_{J',F',m'}[\frac{\langle J',I,F',M'|\epsilon\cdot r|J,I,F,M\rangle\langle J,I,F,M|\epsilon^*\cdot r|J',I,F',M'\rangle}{\omega_{J'}-\omega} + \frac{\langle J',I,F',M'|\epsilon^*\cdot r|J,I,F,M\rangle\langle J,I,F,M|\epsilon\cdot r|J',I,F',M'\rangle}{\omega_{J'}+\omega} \tag{5.68}$$

needs to be put in a form that makes sense to a computer.

Using the formalism of spherical tensors,

$$\langle J',I,F',M'|\epsilon\cdot r|J,I,F,M\rangle = \Sigma_\rho(-1)^{\rho+F'-M'+J'+I+F+1} \times\epsilon_\rho\langle J'||r||J\rangle\sqrt{(2F+1)(2F'+1)}\begin{pmatrix} F' & 1 & F \\ -M' & -\rho & M\end{pmatrix}\begin{Bmatrix} J' & F' & I \\ F & J & 1\end{Bmatrix} \tag{5.69}$$

So,

$$\langle J', I, F', M'|\epsilon \cdot r|J, I, F, M\rangle\langle J, I, F, M|\epsilon^* \cdot r|J', I, F', M'\rangle =$$

$$(2F+1)(2F'+1)\langle J'||r||J\rangle\langle J||r||J'\rangle \begin{Bmatrix} J' & F' & I \\ F & J & 1 \end{Bmatrix} \begin{Bmatrix} J & F & I \\ F' & J' & 1 \end{Bmatrix} \tag{5.70}$$

$$\times\Sigma_{\rho,\rho'}(-1)^{\rho+\rho'+2F'+2F-M'-M+J'+J+2I+2}\epsilon_\rho\epsilon^*_{\rho'}$$

$$\times \begin{pmatrix} F' & 1 & F \\ -M' & -\rho & M \end{pmatrix} \begin{pmatrix} F & 1 & F' \\ -M & -\rho' & M' \end{pmatrix}$$

Note: Both $\begin{pmatrix} F' & 1 & F \\ -M' & -\rho & M \end{pmatrix}$ and $\begin{pmatrix} F & 1 & F' \\ -M & -\rho' & M' \end{pmatrix}$ have to be nonzero to contribute to the sum. By the rules of Wigner 3j symbols,

$$-M' - \rho + M = 0 \tag{5.71}$$

and

$$-M - \rho' + M' = 0 \tag{5.72}$$

Therefore,

$$\rho = M - M' = -\rho' \tag{5.73}$$

Furthermore, by the triangle inequality rules, $\rho = 0, \pm 1$

Therefore, $M' = M - 1, 0, M + 1$ if the term is to be nonzero.

Now, consider the epsilons:

$$\hat{\epsilon} = \epsilon_L \frac{-\hat{x} - i\hat{y}}{\sqrt{2}} + \epsilon_R \frac{\hat{x} - i\hat{y}}{\sqrt{2}} \tag{5.74}$$

Thus,

$$\hat{\epsilon} = \epsilon_L \hat{e}_{+1} + \epsilon_R \hat{e}_{-1} \tag{5.75}$$

and,

$$\hat{\epsilon}^* = -\epsilon_R \hat{e}_{+1} - \epsilon_L \hat{e}_{-1} \tag{5.76}$$

So,

Table 5.2: Values of Circular Polarizations

$\epsilon_{+1} = \epsilon_L$	$\epsilon^*_{+1} = -\epsilon_R$
$\epsilon_0 = 0$	$\epsilon^*_0 = 0$
$\epsilon_{-1} = \epsilon_R$	$\epsilon^*_{-1} = -\epsilon_L$

Therefore, the term is also zero for $\rho = 0$. Thus, the two M' needed to be summed over are $M + 1, M - 1$

Consider now

$$\Sigma_{J',F',M'}\langle J',I,F',M'|\epsilon\cdot r|J,I,F,M\rangle\langle J,I,F,M|\epsilon^*\cdot r|J',I,F',M'\rangle$$

$$= \Sigma_{J',F'}(2F+1)(2F'+1)\langle J'||r||J\rangle\langle J||r||J'\rangle \begin{Bmatrix} J' & F' & I \\ F & J & 1 \end{Bmatrix} \begin{Bmatrix} J & F & I \\ F' & J' & 1 \end{Bmatrix} \tag{5.77}$$

$$\times\Sigma_{M'=M\pm1}(-1)^{2F'+2F-M'-M+J'+J+2I+2}\epsilon_{M-M'}\epsilon^*_{M'-M}$$

$$\times \begin{pmatrix} F' & 1 & F \\ -M' & M'-M & M \end{pmatrix} \begin{pmatrix} F & 1 & F' \\ -M & M-M' & M' \end{pmatrix}$$

1539 Note: by the rules of wigner 3J symbols,

$$\begin{pmatrix} F & 1 & F' \\ -M & M-M' & M' \end{pmatrix}$$

$$= (-1)^{F+F'+1} \begin{pmatrix} F' & 1 & F \\ M' & M-M' & -M \end{pmatrix} \tag{5.78}$$

$$= (-1)^{2(F+F')} \begin{pmatrix} F' & 1 & F \\ -M' & M'-M & M \end{pmatrix}$$

Therefore,

$$\Sigma_{J',F',M'}\langle J', I, F', M'|\epsilon \cdot r|J, I, F, M\rangle\langle J, I, F, M|\epsilon^* \cdot r|J', I, F', M'\rangle$$

$$= \Sigma_{J',F'}(2F+1)(2F'+1)\langle J'||r||J\rangle\langle J||r||J'\rangle \begin{Bmatrix} J' & F' & I \\ F & J & 1 \end{Bmatrix} \begin{Bmatrix} J & F & I \\ F' & J' & 1 \end{Bmatrix} \times \tag{5.79}$$

$$\Sigma_{M'=M\pm1}(-1)^{4F'+4F-M'-M+J'+J+2I+2}\epsilon_{M-M'}\epsilon^*_{M'-M} \begin{pmatrix} F' & 1 & F \\ -M' & M'-M & M \end{pmatrix}^2$$

Furthermore,

$$\langle J||r||J'\rangle = (-1)^{J-J'}\langle J'||r||J\rangle^* \tag{5.80}$$

and, by the rules of Wigner 6-j symbols,

$$\begin{Bmatrix} J' & F' & I \\ F & J & 1 \end{Bmatrix} = \begin{Bmatrix} F & J & I \\ J' & F' & 1 \end{Bmatrix} = \begin{Bmatrix} J & F & I \\ F' & J' & 1 \end{Bmatrix} \tag{5.81}$$

So,

$$\Sigma_{J',F',M'}\langle J',I,F',M'|\epsilon\cdot r|J,I,F,M\rangle\langle J,I,F,M|\epsilon^*\cdot r|J',I,F',M'\rangle$$

$$=\Sigma_{J',F'}(2F+1)(2F'+1)(-1)^{J-J'}|\langle J'||r||J\rangle|^2\begin{Bmatrix}J' & F' & I\\ F & J & 1\end{Bmatrix}^2\times \tag{5.82}$$

$$\Sigma_{M'=M\pm1}(-1)^{4F'+4F-M'-M+J'+J+2I+2}\epsilon_{M-M'}\epsilon^*_{M'-M}\begin{pmatrix}F' & 1 & F\\ -M' & M'-M & M\end{pmatrix}^2$$

Now,

$$|\langle J'||r||J\rangle|^2=\frac{3\hbar(2J+1)}{2m\omega_{JJ'}}f_{JJ'} \tag{5.83}$$

where $f_{JJ'}$ is the oscillator strength

Therefore,

$$\Sigma_{J',F',M'}\langle J',I,F',M'|\epsilon\cdot r|J,I,F,M\rangle\langle J,I,F,M|\epsilon^*\cdot r|J',I,F',M'\rangle$$

$$=\Sigma_{J',F'}(2F+1)(2F'+1)(-1)^{J-J'}\frac{3\hbar(2J+1)f_{JJ'}}{2m\omega_{JJ'}}\begin{Bmatrix}J' & F' & I\\ F & J & 1\end{Bmatrix}^2\times \tag{5.84}$$

$$\Sigma_{M'=M\pm1}(-1)^{4F'+4F-M'-M+J'+J+2I+2}\epsilon_{M-M'}\epsilon^*_{M'-M}\begin{pmatrix}F' & 1 & F\\ -M' & M'-M & M\end{pmatrix}^2$$

Likewise,

$$\Sigma_{J',F',M'}\langle J',I,F',M'|\epsilon^*\cdot r|J,I,F,M\rangle\langle J,I,F,M|\epsilon\cdot r|J',I,F',M'\rangle$$

$$=\Sigma_{J',F'}(2F+1)(2F'+1)(-1)^{J-J'}\frac{3\hbar(2J+1)f_{JJ'}}{2m\omega_{JJ'}}\begin{Bmatrix}J' & F' & I\\ F & J & 1\end{Bmatrix}^2\times \tag{5.85}$$

$$\Sigma_{M'=M\pm1}(-1)^{4F'+4F-M'-M+J'+J+2I+2}\epsilon^*_{M-M'}\epsilon_{M'-M}\begin{pmatrix}F' & 1 & F\\ -M' & M'-M & M\end{pmatrix}^2$$

Therefore,

$$\Delta E = \frac{-e^2 E_0^2}{4\hbar}\Sigma_{J',F'}[(2F+1)(2F'+1)(-1)^{J-J'}\frac{3\hbar(2J+1)f_{JJ'}}{2m\omega_{JJ'}(\omega_{JJ'}-\omega)}\begin{Bmatrix} J' & F' & I \\ F & J & 1 \end{Bmatrix}^2 \times$$

$$\Sigma_{M'=M\pm1}(-1)^{4F'+4F-M'-M+J'+J+2I+2}\epsilon_{M-M'}\epsilon^*_{M'-M}\begin{pmatrix} F' & 1 & F \\ -M' & M'-M & M \end{pmatrix}^2 +$$

$$(2F+1)(2F'+1)(-1)^{J-J'}\frac{3\hbar(2J+1)f_{JJ'}}{2m\omega_{JJ'}(\omega_{JJ'}+\omega)}\begin{Bmatrix} J' & F' & I \\ F & J & 1 \end{Bmatrix}^2 \times$$

$$\Sigma_{M'=M\pm1}(-1)^{4F'+4F-M'-M+J'+J+2I+2}\epsilon^*_{M-M'}\epsilon_{M'-M}\begin{pmatrix} F' & 1 & F \\ -M' & M'-M & M \end{pmatrix}^2] \tag{5.86}$$

Using this formula, the shift in energy levels can be found as shown in Figure 5.5

This shift includes an M_f independent scalar shift, as well as a linearly M_f dependent vector shift. Using this calculation, a reproduction of figure 4 in [48] was succesfully made, and can be seen in Figure 5.6.

the ΔE is the shift in energy for a single ground state - that is to say, it has a specific F and m_F dependence. There is both a scalar shift, and a vector shift that results from this calculation - the scalar shift is the same for all the the m_F sublevels, while the vector shift goes linearly with m_F. The dependence on this is given in the [48] by equation 14:

Figure 5.5: ODT Energy Level Shift

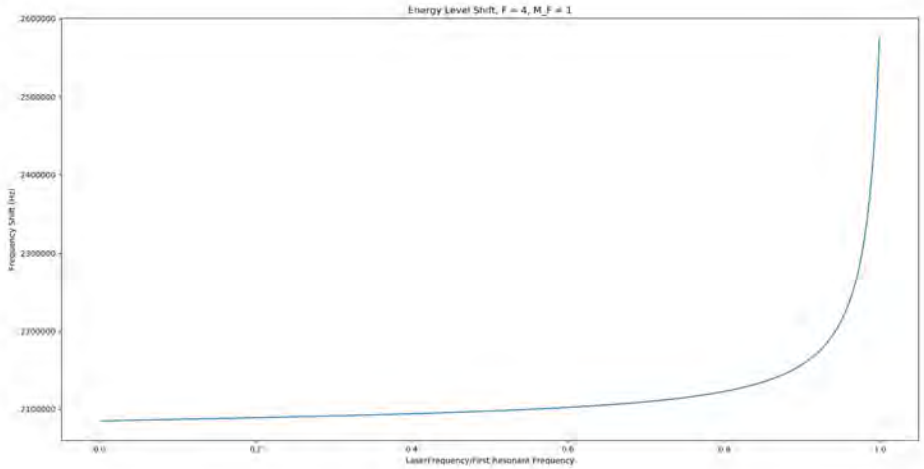

Figure 5.6: ODT Energy Level Vector Shift for Cs-133

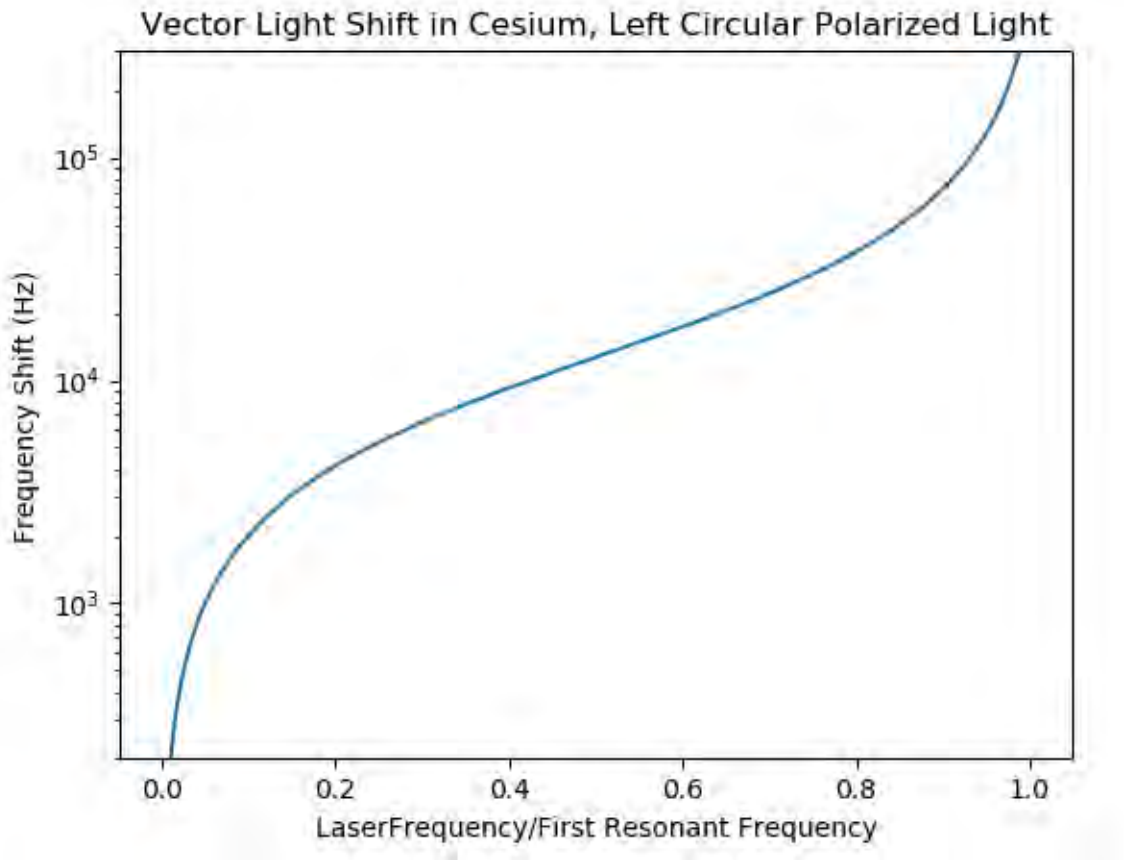

$$\Delta\nu_{F=I\pm1/2} = \pm\nu_V(\omega)(|\epsilon_L|^2 - |\epsilon_R|^2)m_F cos\theta \tag{5.87}$$

the $cos\theta$ term is dependent upon θ, which is the angle between the ODT trap propagation and the spin quantization axis. It is assumed to be 0 for the purposes of calculating the frequency dependence $\nu_V(\omega)$. By having the trap and spin quantization perpendicular, as is done in the RaEDM experiment, the total vector shift can be minimized. The m_F dependence is linear. The dependence on F flips the sign of the change in energy, so the energy gets positive with negative m_F values, and vice versa. It has no bearing on the magnitude of the vector shift. The polarization dependence is given in the term $|\epsilon_L|^2 - |\epsilon_R|^2$. This means that the shift is maximized when the polarization is completely circularly polarized, and that flipping the direction of circular polarization flips the sign of the vector shift as well. In addition, it also suggests that the vector shift should be minimized when the ODT is linearly polarized: when both $|\epsilon_L|^2$ and $|\epsilon_R|^2$ are equal to $\frac{\sqrt{2}}{2}$. Finally, there is the dependnce on ω, which is the actual quantity plotted. In order to get this, the scalar shift has to be subtracted out. The easiest way to do this is to subtract out the term wtih $m_F = 0$:

$$\Delta\nu_{F=I\pm1/2,m_F} = \Delta E(F, m_F) - \Delta E(F, 0) \tag{5.88}$$

The accuracy of this calculation can be tested by testing the dependence of the vector shift on each of these variables.

Consider the m_F dependence. Here is a plot of the vector shift of the m_F sublevels for F = 4:

The vector shift here is linear with m_F - at each ω, each m_F level is separated by the same amount. Further more, the m_F levels go in order, from -4 to +4.

Figure 5.7: Vector Shift Dependence on M_F Sublevel for F = 4

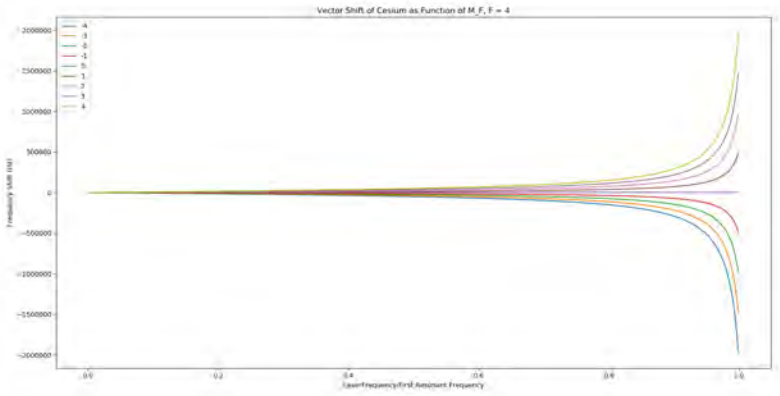

Figure 5.8: Vector Shift Dependence on M_F Sublevel for F = 3

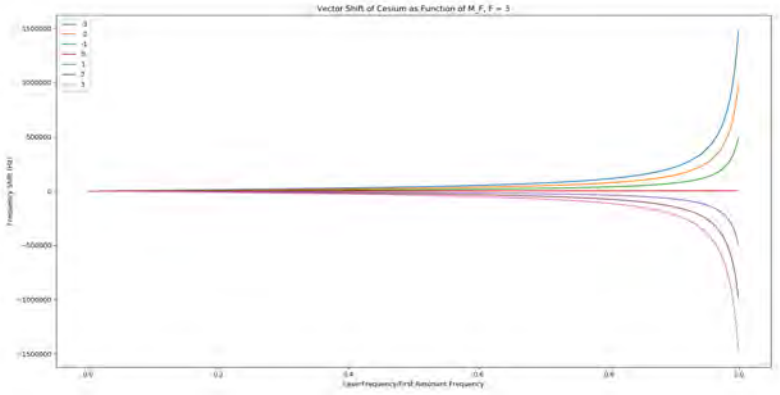

Now, consider F = 3 :

The plot is the same, with one notable exception: instead of going from -3 to +3, it goes from +3 to -3. This is expected, as the change in F is supposed to change the sign of the vector shift.

Finally, consider the polarization dependence. Fix $\frac{\omega}{\omega_1} = .501$, and vary $\epsilon_L = \sqrt{1 - |\epsilon_R|^2}$ from 0 to 1:

Once again, the correct behavior is observed. The shift is minimized at $\frac{\sqrt{2}}{2}$.

Another test that can be done is to compare to a known value given by [48]. This paper

Figure 5.9: Vector Shift Dependence on ϵ_L

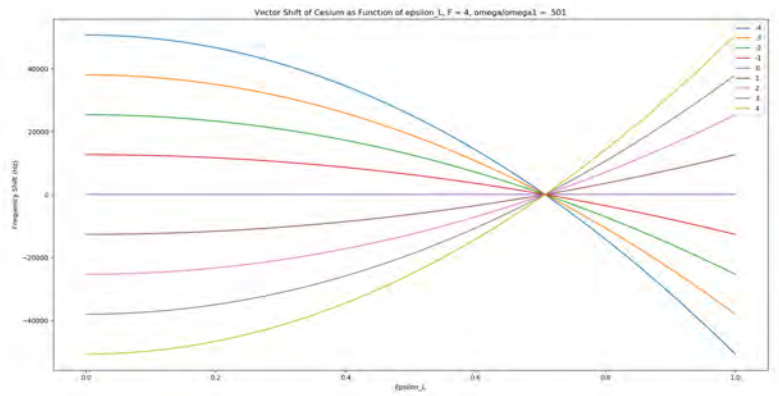

calculates the vector shift at $\lambda = 10\mu m$ to be $\Delta\nu = m \times 170\mu Hz$. Note that this is after a 7 order of magnitude deduction that it makes, with 3 orders of magnitude from minimizing circular polarization, and 3 orders of magnitude by making θ as close to $\frac{\pi}{2}$ as possible. The code used to reproduce these plots returns a value of 1806 Hz, which after a 7 order of magnitude reduction, gives $\approx 181\mu Hz$. So, there is a slight discrepancy here, though it is only 6% higher. Considering that this paper was published in 1999, questions arise if there were issues with the precision of the computers available at the time.

It's important to make clear the dependence on the hyperfine structure: the hyperfine structure is included in the angular momentum coupling. However, it is not included in any correction to the energy level $\omega_{J'J}$ as a function of F. The same energy value is used for all the F' levels for the excited state. Considering the hyperfine structure contribution is much smaller than the overall energy level, this is an acceptable approximation to make. It will not be, however, for the mercury vector shift, since making this approximation results in the vector shift being identically zero. It is necessary to include the splitting of the hyperfine levels in the terms $\omega_{J'J}$.

Figure 5.10: ODT Energy Level Vector Shift for Hg-199

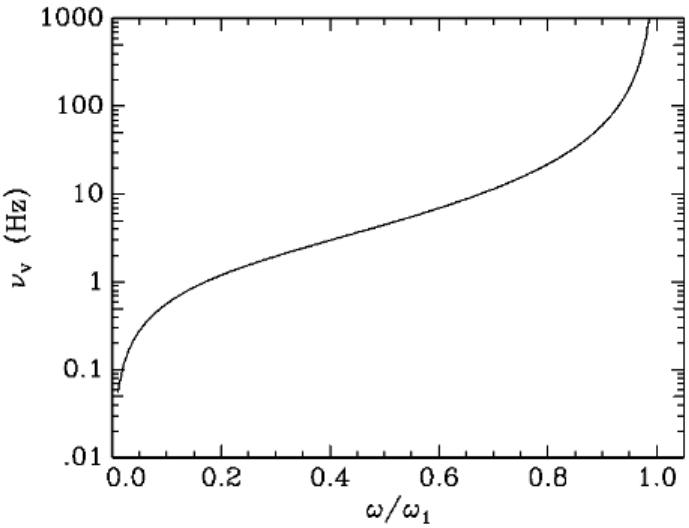

FIG. 7. The vector light shift ν_V for ^{199}Hg for circularly polarized trapping light.

5.3.3 Ongoing Efforts to Caculate the Vector Shift for Hg-199

In [48], the vector shift for Hg-199 is also calculated, and its plot can be seen in Figure 5.10.

With the vector shift for Cs-133 successfully reproduced, the next step is to modify the calculation to account for two valence electrons, instead of one. Thankfully, [48] also contains a vector shift calculation for Hg-199, which has two valence electrons. Once this calculation can also be reproduced, it should be a simple matter to modify the code to work with Radium-225. As such, attempts to reproduce Figure 5.10 are ongoing. Simply swapping the values of the energy levels from Cs-133 to Hg-199 creates a plot that is non-monotonic, as can be seen in Figure 5.11.

This plot is clearly in discrepancy with [48], since it crosses zero. This recent calculation seems to line up with other code previously used by the Radium team, which is available.

Figure 5.11: First Attempt to Reproduce Hg-199 Vector Shift

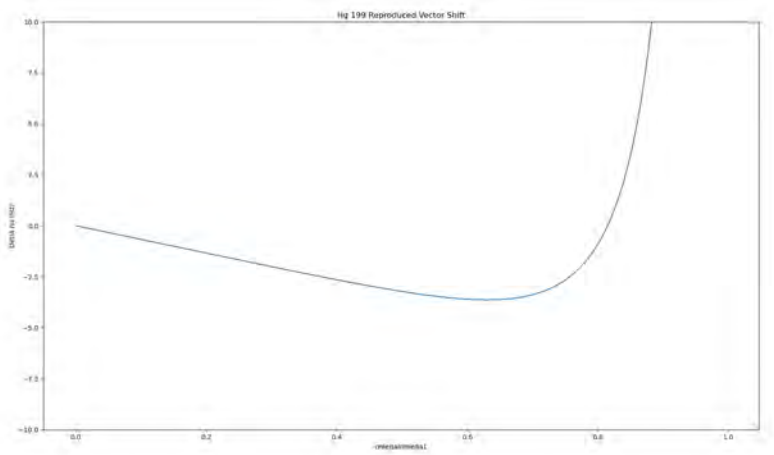

This code seems to also have found a crossing at zero, which lines up very closely with the more recent code. Its plot can be seen in Figure 5.12.

There were concerns about whether or not significant alterations had to be made to the form of the formula, due to the fact that there are two valence electrons instead of 1 - For instance, the energy perturbation that results in the vector shift for cesium is of the form

$$H' = e\mathbf{E} \cdot \mathbf{r} \tag{5.89}$$

where r is the position of the valence electron. Was this form also good for two valence electrons, or would $\mathbf{r}$ have to be replaced with r_1? What would that do to the $|\langle J'||r||J\rangle|^2$ term? Would each J have to be written as the sum of a j_1 and j_2?

It was concluded that this was not necessary, due to equation 9.188 in Sobelman. This equation reads

Figure 5.12: Previous RaEDM Calculation of Hg-199 Vector Shift

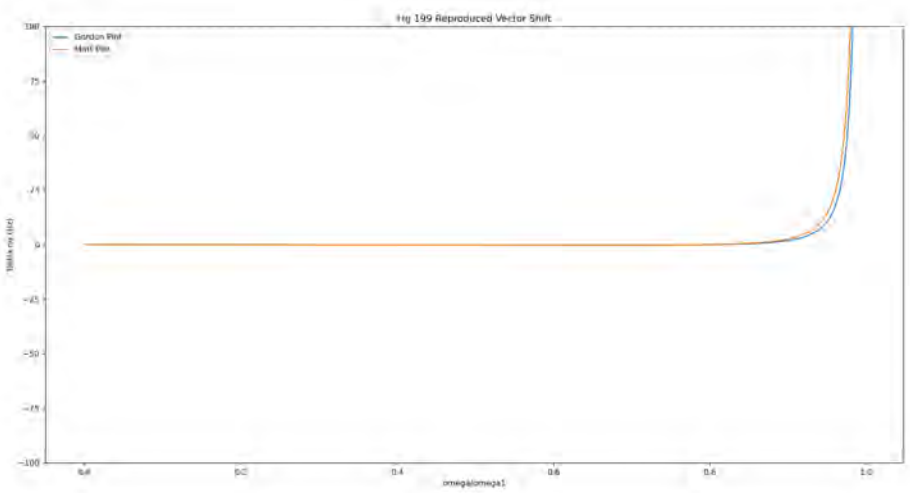

$$-\frac{2m}{3\hbar}\sum_{\gamma',J'}\omega(\gamma J;\gamma',J')\sum_{M'}|\langle\gamma JM|\sum_{j}\mathbf{r_j}|\gamma' J'M'\rangle|^2 = Z \tag{5.90}$$

where $\sum_j \mathbf{r_j}$ is the sum over all electrons in the system. The book then compares this with equation 9.48, which gives the definition for the oscillator strength:

$$-f(\gamma J;\gamma' J') = \frac{2m}{3\hbar e^2}\frac{\omega_{\gamma J,\gamma' J'}}{2J+1}\sum_{MM'}|\langle\gamma JM|\mathbf{D}|\gamma' J'M'\rangle|^2 \tag{5.91}$$

From this equation, it was unclear whether this definition only applies for hydrogen-like atoms. Thankfully, after equation 9.188, it writes:

$$-\frac{2m}{3\hbar}\frac{1}{(2J+1)}\sum_{\gamma',J'}\omega(\gamma J;\gamma' J')\sum_{MM'}|\langle\gamma JM|\sum_{i}\mathbf{r_i}|\gamma' J'M'\rangle|^2 = \sum_{\gamma' J'}f(\gamma J;\gamma' J') \tag{5.92}$$

This seems to suggest that, individually, even for a multi-electron atom, each oscillator

strength $f(\gamma J;\gamma' J')$ is given by

$$f(\gamma J;\gamma' J') = -\frac{2m}{3\hbar}\frac{1}{(2J+1)}\omega(\gamma J;\gamma' J') \sum_{MM'} |\langle \gamma JM| \sum_i \mathbf{r_i} |\gamma' J' M'\rangle|^2 \tag{5.93}$$

In other words, the oscillator strength isn't somehow broken up into the contributions from individual electrons, but instead encompasses the information from all electrons as a whole. This means that the formula

$$|\langle J'||r||J\rangle|^2 = \frac{3\hbar(2J+1)}{2m\omega_{JJ'}} f_{JJ'} \tag{5.94}$$

is used in the same way for Hg as for Cs.

5.3.4 Future Work

Further work has to be done on the Hg-199 calculation, to diagnose why simply plugging in the new values doesn't work. Once diagnosed, it should be a simple matter to plug in the values for Ra-225 and derive its vector shift. In addition, further work needs to be done to characterize the Stark shift, which is particularly dangerous for false EDM effects, considering that it scales directly with the applied static E field.

Chapter 6. Electric Field Upgrades

A key part of the Radium-EDM experiment is the static electric field used to cause a frequency shift due to a non-zero EDM. The electric field has to be as strong as possible, while also having as little leakage current as possible, with discharges being rare, and with a very uniform E field that can be reversed. Looking at the sensitivity equation

$$\delta d = \frac{\hbar}{2E\sqrt{NT\tau\epsilon}} \tag{6.1}$$

It can be seen that the most effective way to decrease uncertainty in d is to increase the electric field, since there is a 1-to-1 correlation in orders of magnitude. Unfortunately, increasing the E field is more difficult than might seem. In addition to more frequent electrode discharges, all the equipment used in the HV switching system must be rated to the required voltage. Efforts are underway to increase the E field for the next Ra-225 data run, through electrode conditioning, and an upgraded HV switching system that will also improve reversibilty of the E field.

6.1 Setup from Previous Ra-225 Runs

The Ra-EDM experiment requires a stable magnetic field for Larmor spin precession. This can be disturbed by magnetic field caused by leakage currents. The leakage can come from two sources: First, extremely small currents that travel through the ceramic mounting for our electrodes, and second, from discharges between the electrodes created by microscopic defects and irregularities on the electrode surface. This was measured at the experimental

setup at Argonne National Laboratory using a Macor support structure, and button-shaped copper electrodes of dimensions shown in Figure 6.1.

Figure 6.1: Radium Run Copper Electrode Dimensions. All Units in mm

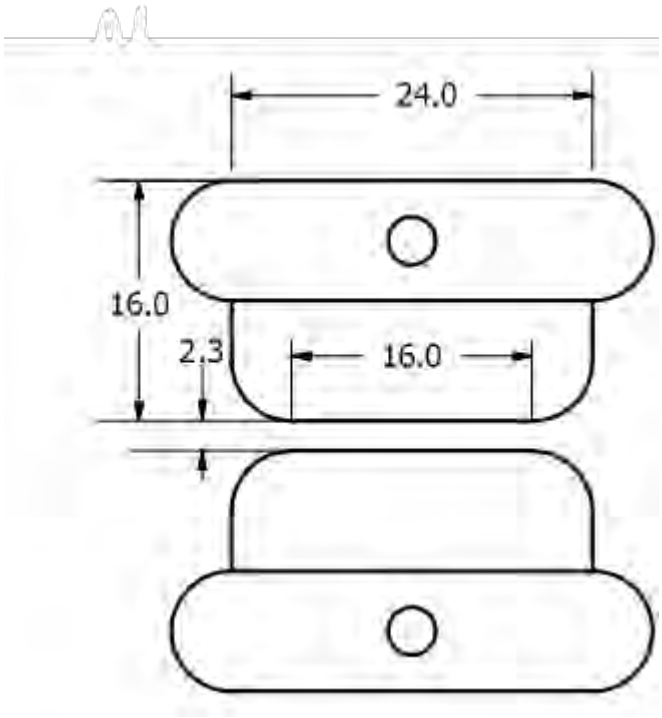

Correct field alignment and direction was absolutely critical to this experiment. "To avoid systematic effects at [the 10^{-26} e cm] level, we must align our fields to within 0.002 radians of their design orientations" [36]. Many of the systematic effects that are present in this experiment get suppressed by improved field alignment - This can be seen, for instance, in the stark interference effect detailed in Chapter 4, where this systematic effect is proportional to $\hat{b} \cdot \hat{\sigma}$ and $\hat{b} \cdot \hat{\epsilon}_s$, where $\hat{b}$ is the direction of the ODT magnetic field, $\hat{\sigma}$ is the direction of spin quantization, and $\hat{\epsilon}_s$ is the direction of the static E field. If the spin quantization axis and static E field are perfectly parallel, and $\hat{b}$ perfectly perpendicular to both, then this systematic has no effect. However, in the real world, the orientations of these angles can only be guaranteed to within certain tolerances. To characterize the orientations of these fields,

an NIST-traceable digital level with 350 μrad absolute accuracy. In addition, the ceramic Macor holder serves its purpose as an extreme insulator. For the duration of the data run, a Picoammeter was used to monitor the leakage current flowing across the electrodes and macor holder. This leakage current was characterized to a 1σ accuracy as being less than 2 pA. The smaller this leakage current, the smaller the systematic effect that results from it. Care also needs to be taken to minimize the frequency of discharges between the electrodes, as this is also results in a current, that greatly disturbs the experiment.

6.2 Electrode Conditioning for Higher Electric Field Generation

The next Ra-EDM run is attempting an improvement in sensitivity of 3 orders of magnitude. In previous data runs, the electric field was provided by a pair of copper electrodes, held $2.3 \pm .1$ mm apart. The bottom electrode was permanently grounded, and the top connected to a bipolar power supply. A $\pm$ 15.5 kV voltage was applied to the top electrode, generating a $\mp$ 67 kV/cm electric field. The whole apparatus was in vacuum. For future data runs, fields on the order of hundreds of kV/cm are desired. This improvement in E field requires solving difficult problems. During the spin precession measurement, it is vital that leakage current be kept to a minimum, and that sudden discharges between the electrodes be avoided. If a discharge occurs during a spin precession measurement, the data taken during that measurement cannot be used. Furthermore, as the electric field is increased, these discharges become more frequent. If upcoming Ra-EDM data runs are to use higher E fields, something must be done to reduce the frequency of these discharges. The solution is electrode conditioning.

6.2.1 Electrode Processing Techniques

The discharges seen between the electrodes are caused by microscopic imperfections on the electrode surface. To reduce these defects, a wide variety of cleaning, polishing, and conditioning techniques were performed. Other materials, such as Titanium and Niobium, were tried. Magnetic Johnson noise and hardness are the important consideration to take into account when selecting the material to use, as well as previous documentation of their stability. Surface processing included buffered chemical polishing, silicon carbide machine polishing, ultrasonic rinses, and high pressure rinses. From there, they were installed in a HV conditioning apparatus under clean room conditions. A summary of the various techniques utilized is given in Table 6.1.

Table 6.1: Surface Processing of Various HV Electrodes. Guide: OF = Oxygen Free. G2 = Grade-2. Simichrome Polish by Hand.DPP = Diamond Paste Polish by Hand. LPR = Low Pressure Rinse. HPR = High Pressure Rinse. HF=Hydro fluoric Chemical Polish. EP = Electropolish. BCP = Bu ered Chemical Polish. SiC = Silicon Carbide Machine Polish. CSS = Colloidal Silica Suspension Machine Polish. VB = 420 - 450 C Vacuum Outgas Bake. WB=150-160 C Water Bake. USR = Ultrasonic Rinse after Detergent Bath

Material	Pair	Surface Processing
OF Copper	Cu_{12}	Simichrome → EP → USR → WB
LG Niobium	Nb_{14}	SiC → BCP → DPP → CSS → USR → VB → LPR → HPR
LG Niobium	Nb_{23}	SiC → BCP → USR → VB v HPR → Resurface BCP → HPR
G2 Titanium	Ti_{24}	SiC → HF → USR → VB → HPR
G2 Titanium	Ti_{13}	SiC → HF → EP → USR → VB → HPR
LG Niobium	Nb_{56}	SiC → BCP → USR → HPR → WB
LG Niobium	Nb_{78}	SiC → BCP → USR → HPR

Of these, pair Cu_{12} was used in the first RaEDM data runs. The Nb_{56} pair is currently installed in the apparatus at Argonne National Laboratory. The conditioning process will now be described.

6.2.2 Electrode Conditioning Procedure

Electrode conditioning was done by holding the electrodes at high voltage for long periods of time, with the belief that over hours of time the rate of discharges would decrease. The apparatus used to do this can be seen in Figure 6.2, taken from [49]

Figure 6.2: MSU HV test apparatus. 1) 9699334 Agilent Turbo-V vibration damper 2) Pfeiffer HiPace 80 turbomolecular pump with foreline Edwards nXDS10i A736-01-983 dry scroll rough pump and two valves 3) Matheson 6190 Series 0.01 micron membrane filter and purge port 4) Ceramtec 30 kV 16729-03-CF HV feedthroughs 5) 0.312 in. 2 electrodes in PEEK holder (resistivity 1016 M cm) 6) 20 AWG Kapton-insulated, gold-plated copper wire 7 MKS 392502-2-YG-T all-range conductron/ion gauge 8) Shielded protection-circuit: Littelfuse SA5.0A transient voltage suppressor, EPCOS EX-75X gas discharge tube, Ohmite 90J100E 100 resistor in series withKeithley 6482 2-channel picoammeter 9) Ohmite MOX94021006FVE 100 M resistors in series with Applied Kilovolts HP030RIP020 HV

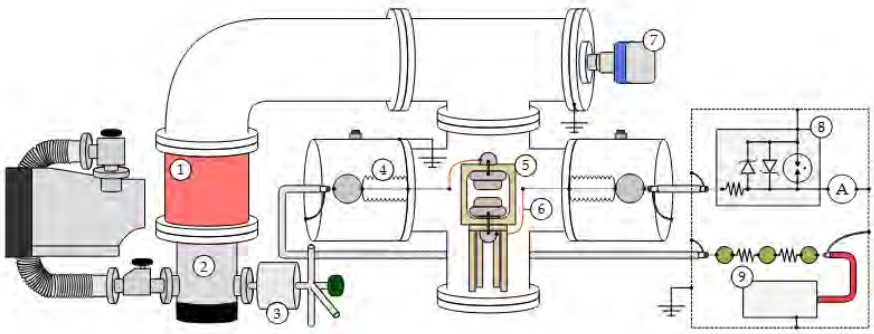

The electrode stand at MSU utilizes the material PEEK, and not Macor. Similar to the design at ANL, the top electrode is permanently affixed to a high voltage power supply, and the bottom is permanently held at ground. The circuit utilizes a picoammeter to measure the current in real time. A measurement of the current consists of taking the average and standard deviation of 8192 samples taken at 16 kHz for Nb_{56} and Nb_{78}, and 30 kHz for Ti_{13} and Nb_{23}. This current reading was used to characterize the leakage current, as well as detect any discharges. The conditioning was done in 4 minute cycles. The Voltage was ramped up to the positive polarity, where it was held for 60 seconds. Afterwards, the high

voltage was reduced back to zero, where it was kept for another 60 seconds, and a signal sent to the HV power supply to reverse the polarity. Then, 60 seconds of high voltage in the reversed direction was applied, and then another 60 seconds of High voltage off. This was done to simulated the cycle of measurements during the Ra EDM procedure. By doing this for many hours, with the voltage being steadily ramped up, the electrodes could be conditioned, with discharges kept to a minimum. Utilizing this technique, the Nb_{56} pair was conditioned to be able to accept fields of 20 kV/mm with no discharges, then installed in the apparatus at Argonne National Laboratory, where it was revalidated to accept this field strength. A display of the results of this conditioning can be seen in Figure 6.3, also taken from [49]

Figure 6.3: Conditioning Results for Nb_56

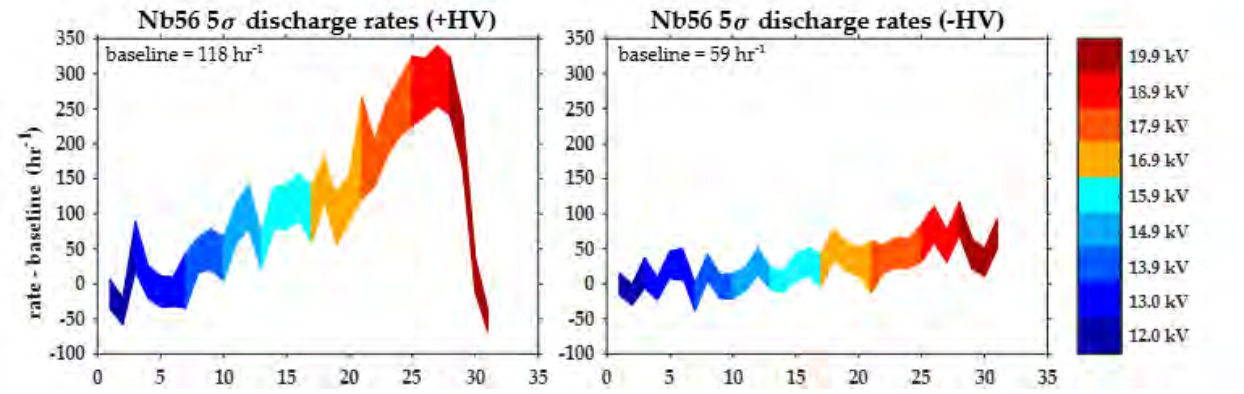

During the conditioning, it was noted that discharge rates markedly increased for negative polarity instead of positive polarity. This suggests a fundamental difference in the circuitry within the Applied Kilovolts bipolar power supply, between the positive and negative polarities. This signifies other potential discrepancies between the two E field directions, such as in E field strength. This would cause an increase in the E^2 systematic effect. To

resolve this, efforts are underway to utilize a unipolar power supply, with a system of relays to swap the polarity between electrodes. An improved HV divider will also allow for more precise measurements of the E field applied.

6.3 Upgrades Needed to Achieve Higher Voltage

To increase E field and decrease systematics, new components and parts were necessary. They will now be discussed.

6.3.1 HV Power Supply

Two different power supplies were utilized to perform electrode conditioning for the Ra EDM experiment. The apparatus at Argonne National laboratory currently uses a Spellman HV CZE 2000 power supply. The electrodes conditioned at MSU utilized an Applied Kilovolts HP030RIP020 Power supply. The next round of conditioning will utilize a Heinzinger PNChp60000-1 power supply, to allow for higher applied voltages and improved stability.

Table 6.2: RaEDM Power Supply Specifications

Specification	Spellman HV	Applied Kilovolts	Heinzinger
Model Number	CZE 2000	HP030RIP020	PNChp60000-1
Maximum Voltage	30 kV	30 kV	60 kV
Polarity	$\pm$	$\pm$	+
Maximum Current	.3 mA	.25 mA	1 mA
Maximum Voltage Drift over 8 Hours	0.02%	0.05%	.0001%
Maximum Voltage Drift at 30 kV over 8 Hours	6 V	15 V	30 mV
Maximum Voltage Ripple	.1% V_{p-p}	.001% V_{p-p}	.001% $V_{p-p} \pm 50$mV
Maximum Voltage Ripple at 30 kV	30 V	300 mV	350 mV

6.3.2 High Voltage Feedthroughs

This increase in power requires various components to be upgraded, to be compliant with the increase in voltage. Two of these components are the HV feedthroughs which lead the high voltage into the electrode test stand. The 30 kV Ceramtec feedthroughs previously installed were upgraded to 50 kV versions. Specifications can be found in Table 6.3

Table 6.3: Specifications for HV Feedthroughs

Model	Max. Voltage	Max. current	Diameter of Inuslator	Fitting
16729-03-CF	30 kV	3 A	1.5”	2.75” CF Flange
21184-01-CF	50 kV	10 A	1”	2.75” CF Flange

The fact that these new feedthroughs are rated only to 50 kV and not 60 kV means some kind of hardware limiting the output of the HV power supply to only 50 kV will be required.

6.3.3 High Voltage Cables

Another component crucial to the setup are the cables leading from the cage to the electrode stand. These are M1 Mammoflex cables manufactured by Claymount. They are coaxially shielded cables with a single conductor inside, able to handle 60 kV of voltage. In the future, Varex Imaging L4-type cables may be used. Their specifications can be found in Table 6.4

Table 6.4: HV Cable Specifications

Model	Max. Voltage	Max. Current	Internal Resistance	Internal Capacitance
M1-type Mammoflex	60 kV	3 A	$\geq 10^{12}\Omega \cdot m$	171 pF/m
L4-Type Cable	75 kV	9 A	$\geq 5 \times 10^{12}\Omega \cdot m$	865 pF/m (bare conductor)

The HV components and circuitry necessary for switching the voltage from electrode to electrode is kept in a grounded metallic box, known as the HV cage.

6.3.4 HV Cage Design

In order to safely perform the high voltage work necessary for electrode conditioning, a grounded cage must surround any hot components. This cage must have adequate spacing to prevent discharge from hot components to grounded components.

6.3.4.1 Old Cage Design

The previous high voltage cage was created with a maximum voltage of ±30 kV specified. The breakdown of voltage in air was taken as about 75 kV/in. When considering humidity, it became possible for the breakdown voltage to be reduced by a factor of 2, to 37.5 kV/in. This implies that for 30 kV, a minimum of .8 inches of distance should be between any hot components and ground. With an additional factor of 5 for safety, the old cage was designed with a minimum distance of 4 inches between any hot components and ground. The internal components can be seen in Figure 6.4.

This layout was able to be used for leakage testing the new mechanical relays at 30 kV. To utilize the full 60 kV of the new high voltage system, however, a new cage is required.

6.3.4.2 New Cage Design

The new HV system requires not only large relays, but two large HV dividers as well. These all need to be housed with a larger distance from hot components to ground, due to the factor of 2 increase in voltage. Current FRIB guidelines require 1 inch of separation for every 10 kV. This would necessitate 6 inches of separation between all hot components and ground. Designs of the new cage have already been considered, with concepts like the one seen in Figure 6.5.

Figure 6.4: Overview of inside of Old HV Cage. 15) 1 3/8 brass ball connector on glazed grade L5 ceramic, 5 cylindrical standoffs 16) Ohmite MOX94021006FVE 10 W, 45 kV-rated 100 MΩ resistors 17) Spinlab transient protection circuit in light- tight EM shield. Littelfuse SA5.0A transient voltage suppressor (TVS) diode, EPCOS EX-75X gas discharge tube (GDT), Ohmite 90J100E 1.08 kV, 11 W-rated 100 Ω resistor 19) Applied Kilovolts HP030RIP020 bipolar power supply 20) Keithley 6482 2-channel picoammeter 21) NIST-traceable high voltage divider, Ross model VD30-8.3-BD-LD-A 880.8:1 120 MΩ

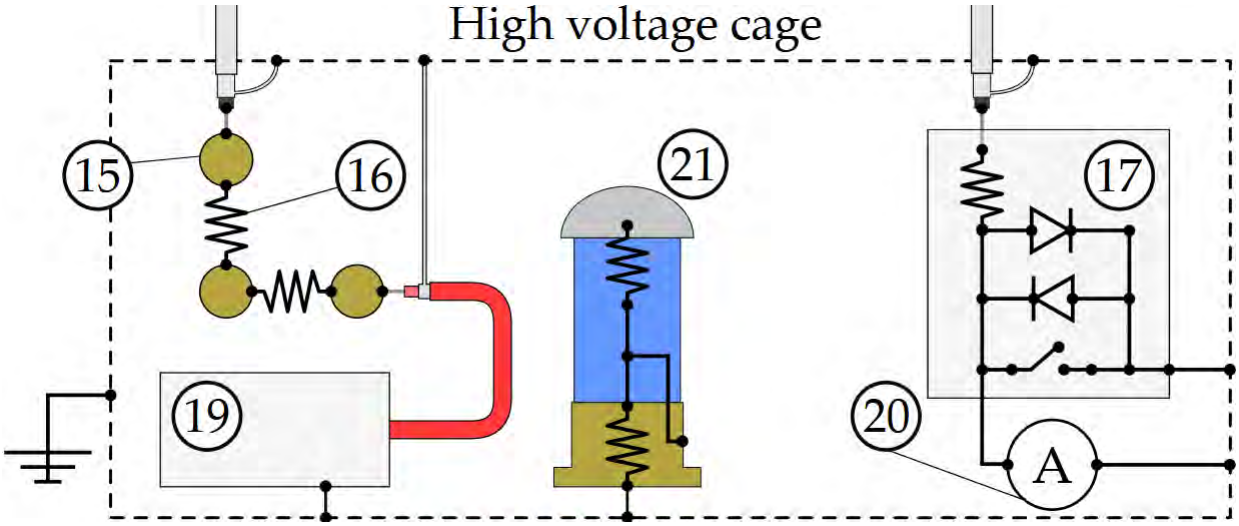

In addition, another size of protection may be needed for the HV stand itself to protect the feedthroughs going into the vacuum chamber. Sufficient radiological shielding will also be needed so that x-rays produced by discharge will not increase radiation doses above acceptable levels. A previous calcuation done for 30 kV is shown in Figure 6.6

Efforts are underway to reproduce this plot, to then be able to modify its calculation to 60 kV of voltage. This new HV cage will also require an interlock system to prevent unwanted contact between personnel and hot components.

6.4 Upgrades to Improve E-Field Reversibility

Previously, the RaEDM experiment, for both the main apparatus at Argonne and the electrode conditioning stand at MSU, used the apparatus shown in Figure 6.7

Figure 6.5: Non-Finalized Diagram of the New HV Cage Concept

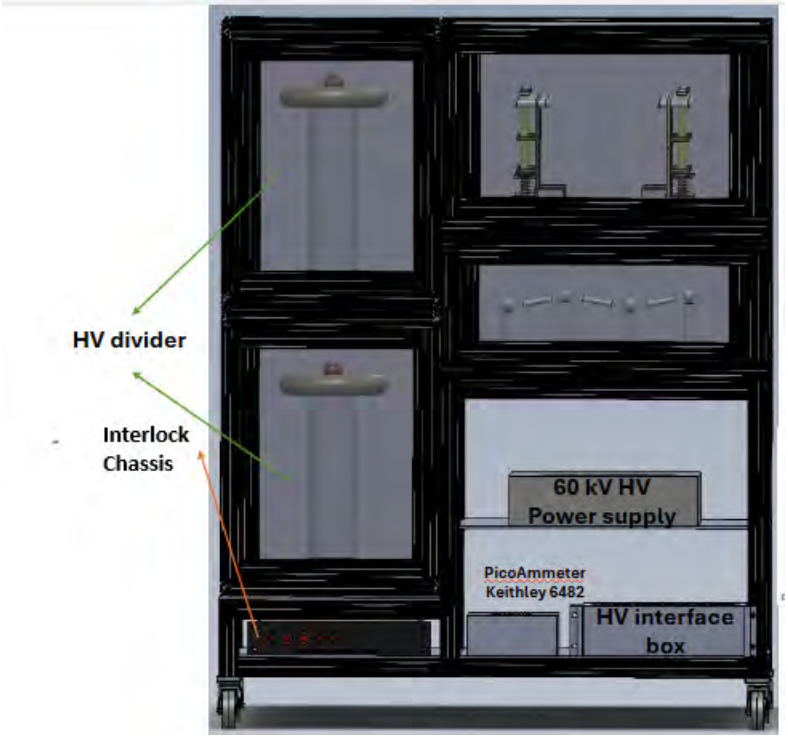

With a unipolar power supply, a new apparatus like the one shown in Figure 6.8 is required.

This switching system, utilizing high voltage, needs careful consideration. Not only does leakage current have to be minimized, and all components rated to the new high voltage, but safety is paramount. For this reason, new components are needed, and safety systems and interlocks put in place.

6.4.0.1 Relay Circuit

A precise circuitry diagram of the old HV conditioning setup can be seen in Figure 6.9

For the new setup, a new circuit must be made, and can be seen in Figure 6.10

The relays for this upgrade were important to get right, and will now be discussed.

Figure 6.6: Maximum X-Ray Power Spectrum from 1 mA Electron Current at 30 kV, after Passing through 5 mm of Pyrex 7740

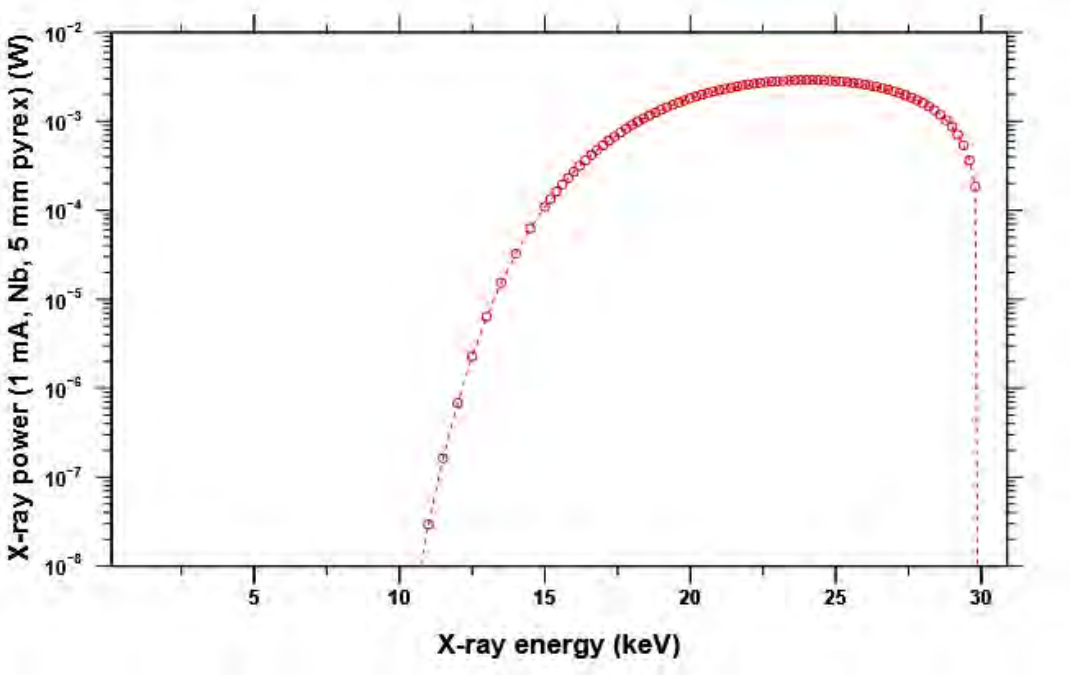

6.4.0.2 Mecahnical Relays

The new setup will utilize four Single-Pull Single-Throw (SPST) mechanical relays for the high voltage switching. The specifications for these relays is shown in Table 6.5

Table 6.5: Specifications for SPST Relays for HV Switching

Manufacturer	Ross Engineering
Part Number	E60-NO-80
Contact Rating	60 KV
Insulation to Groud	80 kV
Maximum Dimensions	$6 \times 4 \times 14.25$ (in)
Rated Resistance (Open)	
Actuation Power	115 V, 60 Hz Coil
Maximum Switching Time	140 ms

These relays have a pair of mechanical switches on the side, that are depressed when the

Figure 6.7: Legacy HV RaEDM Apparatus

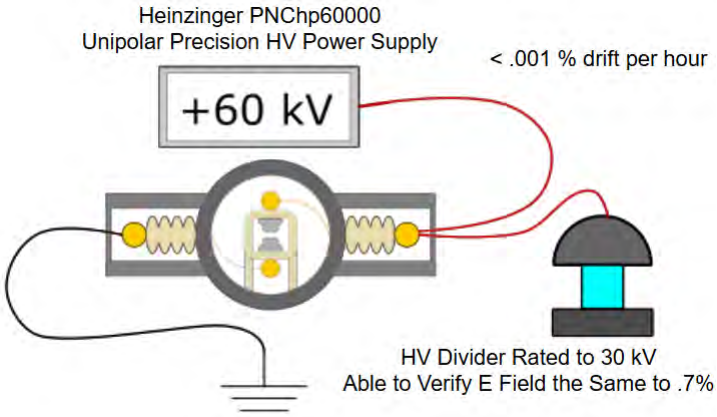

Figure 6.8: Planned HV RaEDM Apparatus

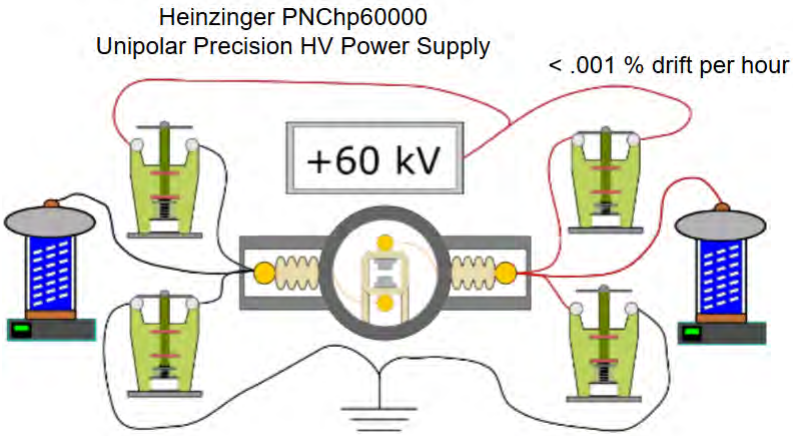

relay is closed. There are three contacts on each switch, that make the switch able to be used in either a normal closed or normal open capacity. Since these are mechanical, they are very useful for diagnosing whether a switch is open or closed, as they aren't susceptible to any bugs in the software. They can be utilized to design a completely hardware-based logic interlock system, as will be discussed later. These two switches with three contacts each give a total of six contacts. In addition, there are two more to actuate the relay, by applying standard American 125 V 60 Hz wall power to its coil. This gives a total of eight contacts,

Figure 6.9: Diagram of Legacy Circuit

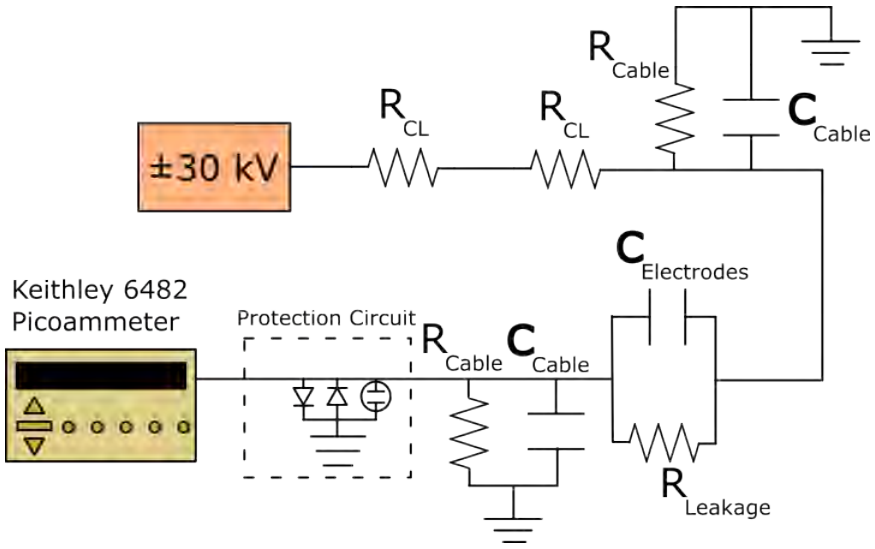

two of which are at high voltage. The nature of the high voltage means that an insulating shield is needed, to prevent unwanted contact. This is done by utilizing a 3D-printed shield, which can be fastened onto the base of the relay utilizing 3D-printed brackets. An overview of attaching the shields to the relays will be given in the appendix. The various contacts are attached to feedthroughs that allow for the electrical components to be accessed from the outside. The feedthroughs allow for 120 VAC power to be provided with a standard power cord. Actuating the relay amounts to turning this 120 VAC power on and off. This can be accomplished utilizing a Powertail. The Powertail is a power module that has an outlet that turns on and off from a 5 V input signal.

6.4.0.3 Solid State Relay

In addition to the mechanical relays, a Behlke HTS-500-10 HV solid state relay will also be used directly after the power supply. This is to allow the HV to quickly disconnect, at a rate faster than the mechanical relays can. The specifications of the relay are shown in Table 6.6

Figure 6.10: Planned Circuitry for HV Upgrade

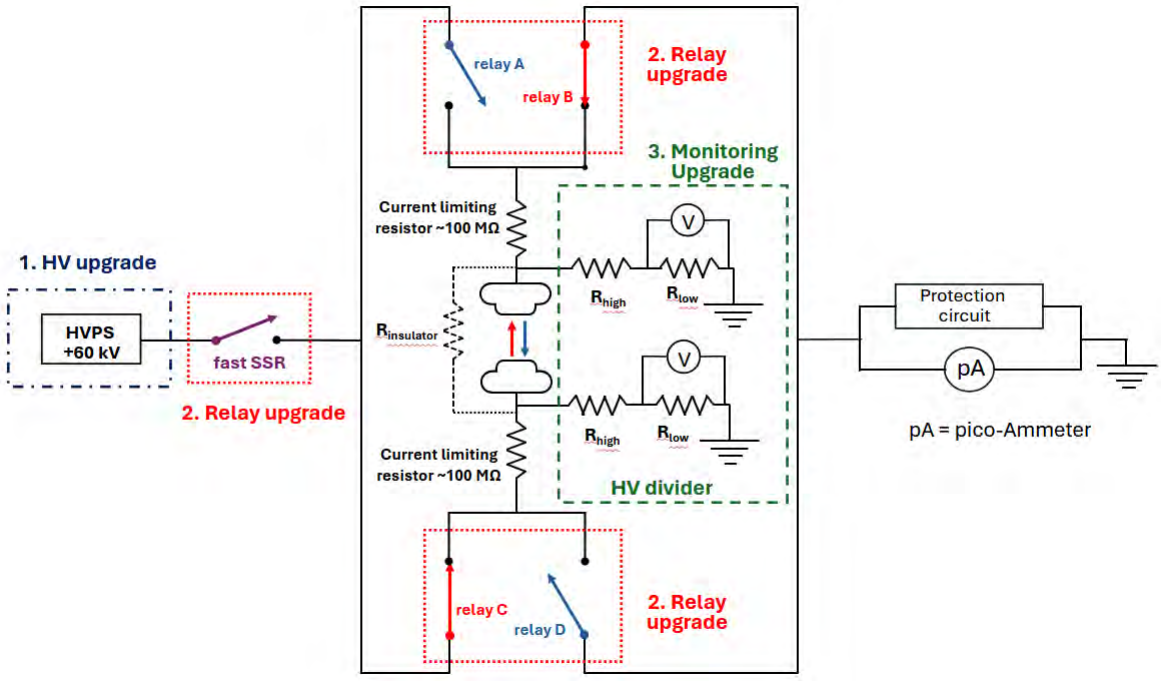

Table 6.6: Solid State Relay Specifications

Specification	Value
Model	Behlke HTS-500-10
Maximum Voltage	50 kV
Minimum Turn-On Time	200 ns
Minimum Turn-Off Time	210 ns
Interface	4-pin pinout

Interfacing with this relay requires additional circuitry to control. Such a circuit should look something like in Figure 6.11

With all these mechanical relays, hardware interlocks will be necessary to make sure high voltage never goes straight to ground.

Figure 6.11: Circuit for Interfacing with the Solid State Relay

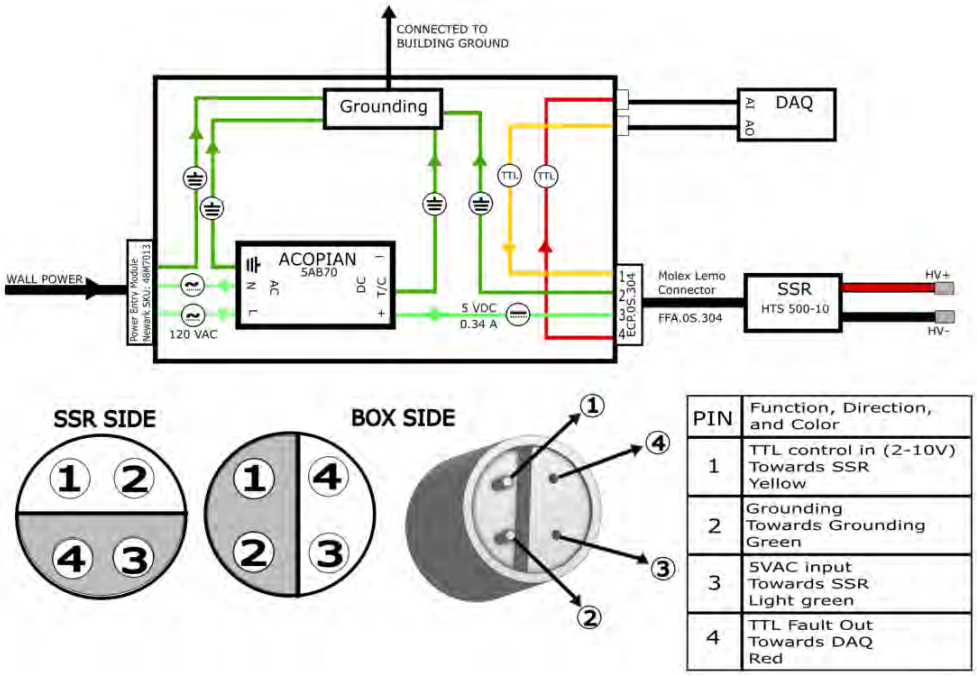

PIN	Function, Direction, and Color
1	TTL control in (2-10V) Towards SSR Yellow
2	Grounding Towards Grounding Green
3	5VAC input Towards SSR Light green
4	TTL Fault Out Towards DAQ Red

6.4.0.4 Interlock Design

An essential component of the HV safety cage is the presence of interlocks that interrupt the power to the high voltage power supply. This means that, if anyone should attempt to access the inner workings of the cage, the power will be immediately interrupted and shut off. The circuitry to do this is contained in the interlock Chassis.

Figure 6.12: Interlock Chassis Circuitry Diagram Pt. 1

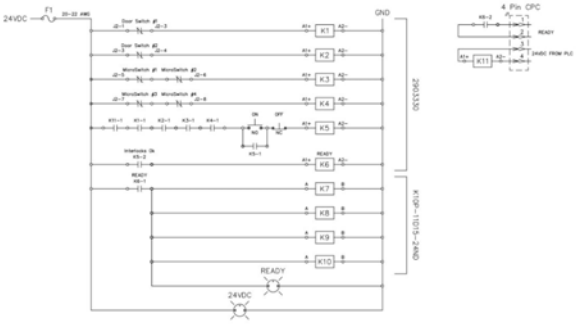

Figure 6.13: Interlock Chassis Circuitry Diagram Pt. 2

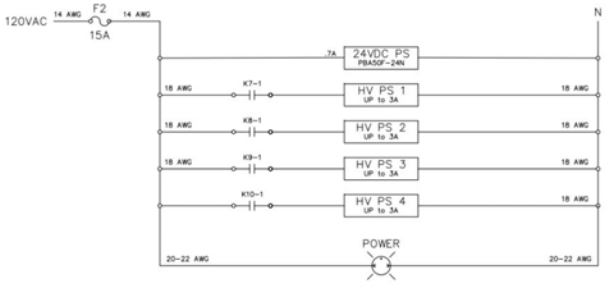

A similar system, with interlocked soup cans and doors, will have to exist in the new HV cage. In addition, another interlock system will be needed so that at no point does the high voltage get connected directly to ground. In a system such as this:

Figure 6.14: Basic Relay Setup

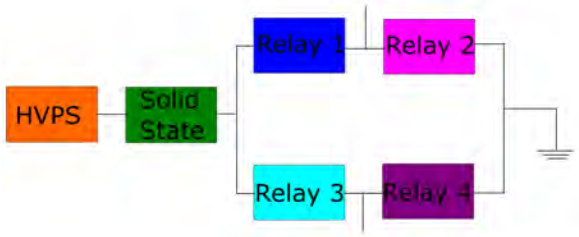

it's important that hardware based logic be implemented to prevent shorts to ground. A logic system needs to be built something like in Figures 6.15 and 6.16.

The mechanical switches on either side of the relays can prove very useful for this, since they provide a way, free of any software, of telling whether or not a relay is open or closed. Consider a setup like in Figure 6.17

With this setup, there are normally open relays interrupting the logic that flows from the control to the powertails that turn the power on and off to the mechanical relays. Should relay 1 close, then the voltage closing the control relay for relay 2 is interrupted, and it opens. Even if a signal is sent to close relay 2, it will not be received by its powertail. The

Figure 6.15: Relay Logic Pt. 1

Figure 6.16: Relay Logic Pt. 2

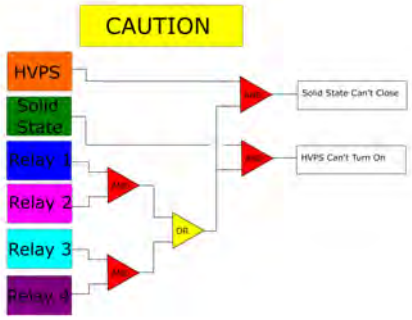

same is true for relay 2 interrupting relay 1. Notice that, should something fail with the 5V power supply that powers the interface, the relays inside will both result to their normal open positions, and neither relays 1 or 2 will be able to be closed. The implementation of a system like this was the reason for the choice of 4 SPST relays, instead of 2 SPDT relays. With these relays in place, a more precise measurement of the voltage across the electrodes was desired. For this reason, new HV dividers were needed.

Figure 6.17: Hardware Logic to Interrupt Relays

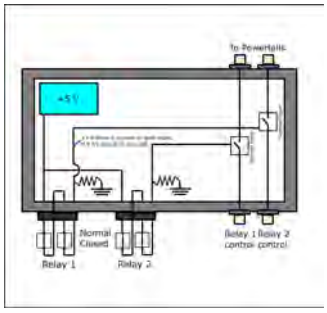

6.5 Upgrades to Electric Field Monitoring

In the most recent limit measured for the EDM of Radium-225, the E field across the electrodes could only be verified to be the same for both orientations to within .7%. To change this, a more precise way to measure the voltage applied to the electrodes is needed. In addition, due to the new relay setup, two of these HV dividers would be needed instead of one. the choice of design to use was settled upon a design traceable to the Physikalish-Technische Bundesanstalt (PTB) from Germany. Three of these HV dividers were previously made, one by PTB, and two in the lab of Kei Minamisono at FRIB. One of the FRIB HV Dividers was given to us, for our use. The other would have to be custom made. Great progress has been made with its assembly, though issues with the temperature controlling circuitry still exist. The assembly is discussed in detail in the appendix.

6.5.1 HV Divider Operation

The HV divider consists of a corona ball and disk at its top where high voltage can be applied, a temperature-controlled cylinder with HV resistors wound around in series a spiral pattern below it, and a metal box at the bottom containing the relevant circuitry for operating the

Figure 6.18: Circuitry for HV Divider Temperature Controller

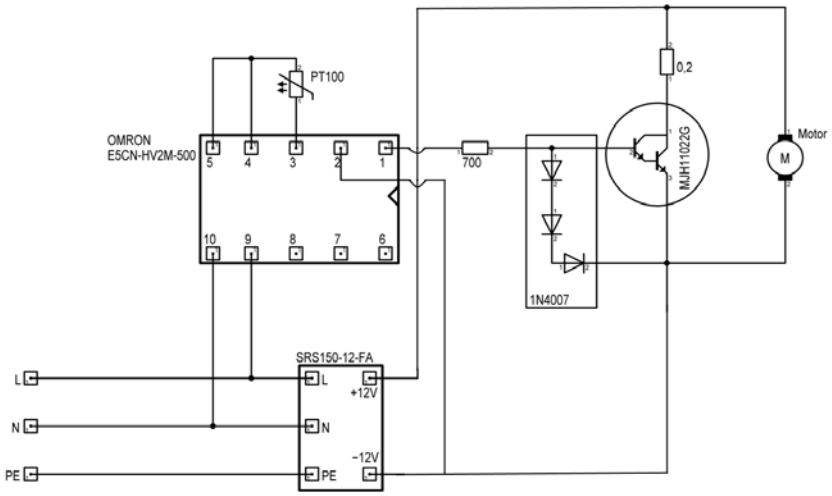

temperature control. This Circuitry can be seen in Figure 6.18

The HV dividers winding down the center pillar lower the voltage to an acceptable level, with extremely precise HV resistors. These resistors are rated to each handle 1 kV across them, and are 10 MΩ each. They come in sets of 5, meant to be used each in series. The resistors used for these HV dividers in particular are marked "MDN1475", indicating that the resistors are individually selected based on their individual temperature coefficients, so that the five resistors in series have, in aggregate, as low of a temperature coefficient as possible. As such, it's extremely important that sets of 5 stay together, and that these are marked. 12 sets of 5 resistors are used, so that for 60 kV applied at the top, each individual resistor only receives a 1 kV voltage drop across it. The total resistance is thus 600 MΩ. In series with this coil of resistors is a very precise 700 resistor. It is across this resistor that the voltage is measured. For a maximum voltage applied of 60 kV, there will only be a 70 mV voltage across the 700 Ω resistor - this can then be safely measured by a voltmeter. In the metalbox below the main cylinder lies the temperature control system.

Figure 6.19: Difference in Relative Voltage to Average between HV Dividers

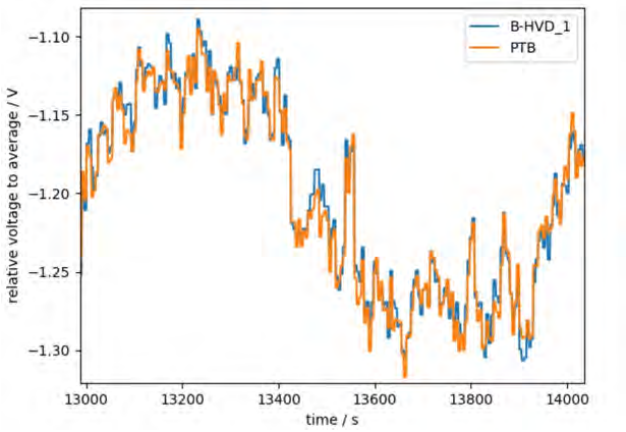

This utilizes a temperature feedback console that continuously measures the temperature with a temperature probe inside the cylinder, and sends current to a transistor whenever it needs to warm up. When working properly, this will create a stable temperature in the HV divider, which improves the stability of the resistors.

6.5.2 HV Divider Specifications

The HV divider provided to us, HVD-3, was tested versus the HV divider made by PTB. To perform this test, both dividers were attached to the same 30 kV power supply, and two voltmeters were used to measure the data simultaneously. The purpose was to see how closely the two measured the same voltage. Data taken looked like Figure 6.19, using another test with HVD-1 as an example.

Three runs were done of this experiment, performed by Professor Kei Minamisono, and the results for the B-HVD3 divider can be seen in Table 6.7

For each run, the standard deviation of the difference between the two, $\sigma_{PTB-BHVD}$, was less than a single part per million. With two of these HV dividers, part-per-million sensitivity to E field reversibility can be achieved. Another crucial component to this experiment is

Table 6.7: Experimental Runs for B-HVD3

Run	Voltage (kV)	Voltmeter 1	Voltmeter 2	PTB/ B-HVD3	$\sigma_{PTB-BHVD}$
1	30 kV	B-HVD3	PTB	1.000052	.27 ppm
2	30 kV	PTB	B-HVD3	1.000026	.23 ppm
3	10 kV	PT	B-HVD3	1.000025	.10 ppm

Figure 6.20: Legacy Protection Circuit

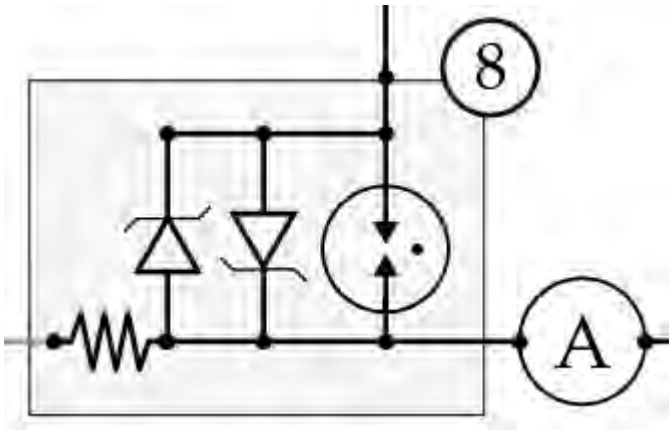

the monitoring of leakage current. This utilizes a Picoammeter, with a protection circuit to protect it from intermittent discharges. This protection circuit took time to get right, and will now be discussed.

6.5.3 Protection Circuit Development

The original protection circuit that was present in the old circuit diagram looked like 6.20

The diodes used were 5.0A TVS diodes, in parallel in opposite directions, and an EC75X Gas Discharge Tube. The resistor used was 1 $k\Omega$. The picoammeter, of model type Keithley 6482, was attached parallel to all three. Some relevant specifications are given in Table 6.8

To test the protection circuit, a Keithley 6221 current source was used. Some specifications are in Table 6.9

The current source has a "Voltage Compliance," which is the maximum voltage the

Table 6.8: Specifications of Keithley 6482 Picoammeter

Specification	Value
Model	Keithley 6482
Maximum Current Range	±20 mA
Minimum Current Range	±2 nA
Resolution at Minimum Current Range	1 fA
Current Input	Triaxial Cable
Reading Output	Analog or Digital
Maximum Input Impedance	20 $k\Omega$ @ 2 nA setting

Table 6.9: Specifications of Keithley 6221 Current Source

Specification	Value
Model	Keithley 6221
Maximum Current Range	100 mA
Minimum Current Range	2 nA
Voltage Compliance Range	.1V to 105V (Typically set to 47 V)
Current Output	Triaxial Cable
Remote Control Protocol	SCPI

current source is willing to output to reach the desired current output. Typically, this was set to 47 V, lower than the 50 V lab threshold where additional safety measures need to be taken. Care had to be taken that any observed cutoff current was the result of the protection circuit working as intended, and not caused by the voltage hitting the compliance limit. Testing the circuit was done by attaching the current source to the protection circuit, and sweeping the output current.

Figure 6.21: Legacy Protection Circuit Testing Diagram

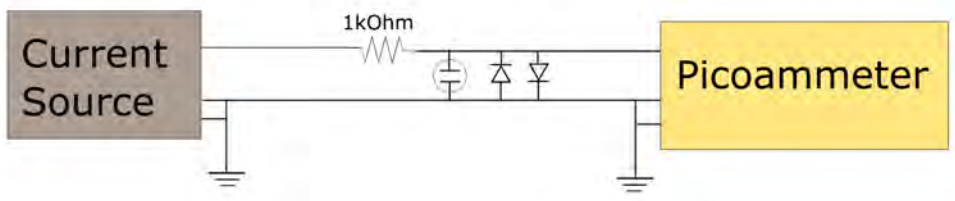

In this diagram, for the triaxial connections, the top wire is the inner conductor, the middle wire is the outer conductor, and the lower wire is the braided shield around the triax. A test was done to vary the input current from -200 nA to 200 nA twice, once with the current source directly attached to the picoammeter, and once with the legacy protection circuit installed. At each current source setting, the picoammeter was allowed to run for a few seconds, so that a histogram could be made of the data, shown in Figure 6.22

Figure 6.22: Histogram of Picoammeter Reading Counts

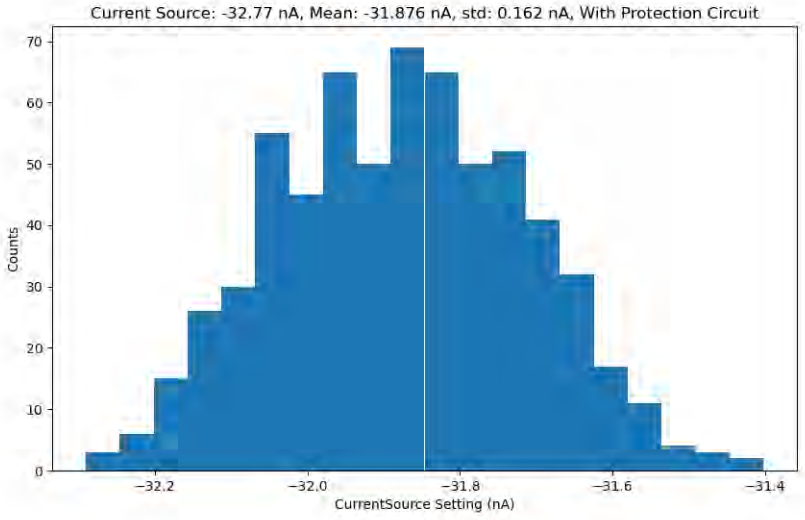

By taking the mean and standard deviation of this data, a central value and error could be retrieved. From there, the readings could be plotted relative to the current source setting.

Note the horizontal errorbars in Figure 6.23, which account for the error specification in the current supply. The coefficients for the linear fit are shown in Table 6.10

Table 6.10: Values of Linear Fit for Legacy Protection Circuit and Baseline

Test	Slope	Offset (nA)
No Protection Circuit	.99562 ± .00002	-.098 ± .001
With Protection Circuit	.9955 ± .0001	.670 ± .006

Figure 6.23: Legacy Protection Circuit Current Readings Compared to Baseline

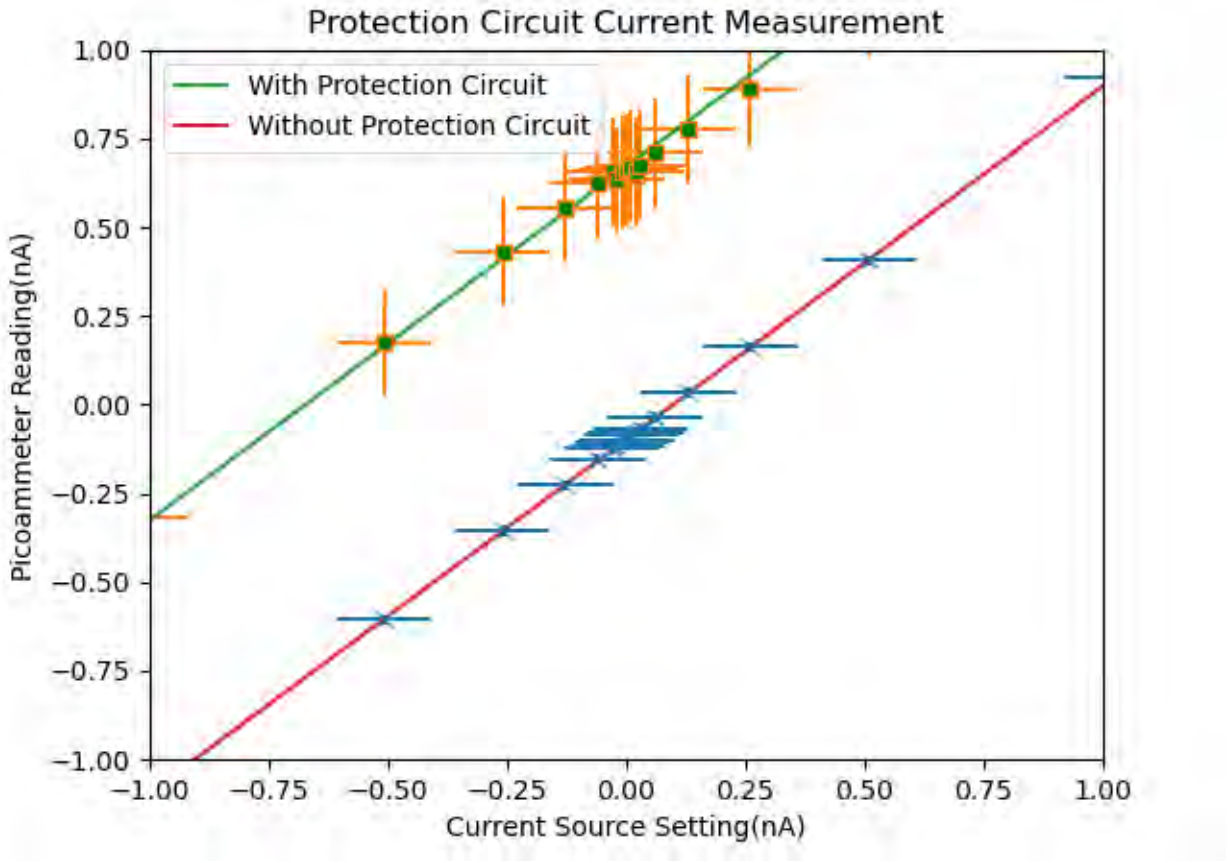

The issue seen was a lack of a cutoff above 200 nA, as well as a slight offset in the current reading, equivalent to 670 pA. This suggested that the protection circuit needed some modifications. A different system was built, shown in Figure 6.24

This setup made sure to isolate the loop of current from the surroundings. In order to collect and record the data, the analog output voltage was used. This utilized a triaxial output. The outer shield was grounded to the box, and connected to the ground as well, while the inner and outer conductors were attached to an NI DAQ card to collect data. While taking data, there was a discrepancy noted between what was being read on the computer, and what was being displayed on the display of the picoammeter. A test was

Figure 6.24: Diagram of Intermediate Setup

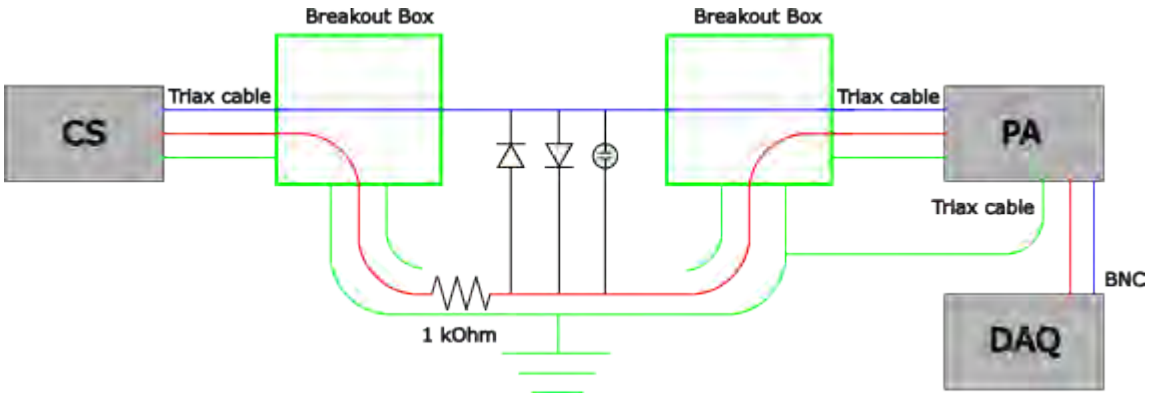

done where at each step of the current source, data would be taken by the computer, and an approximate value would be taken for the reading displayed. The data taken by the computer at each step had a histogram made, with the mean and standard deviation. The value for the displayed reading was taken to have an uncertainty of .1 nA. A residual plot was then made, of the difference between the displayed reading and the computer-measured reading. The uncertainty was propagated from both measurements to the residual, shown in Figure 6.25

This gives a linear relationship of the residuals, with a slope of -.00502 $\pm$ .00005. Clearly, some kind of cross talk was going on. The solution to this was to instead use a GPIB digital connection to read from the picoammeter. As development continued, it was desired to be able to change the current cutoff. The solution to this was to include a resistor in series with the picoammeter, so that at a specified current, the voltage would cause current to flow through the diodes. This used the circuit shown in Figure 6.26

Four different resistor values were used, and each had two current scans performed. The first scan would scan from -200 to 200 nA. the second scan scanned from -2 to 2 mA. It should be noted when these scans were performed, the current was still recorded through

Figure 6.25: Residual between Picoammeter Display and Analog Reading

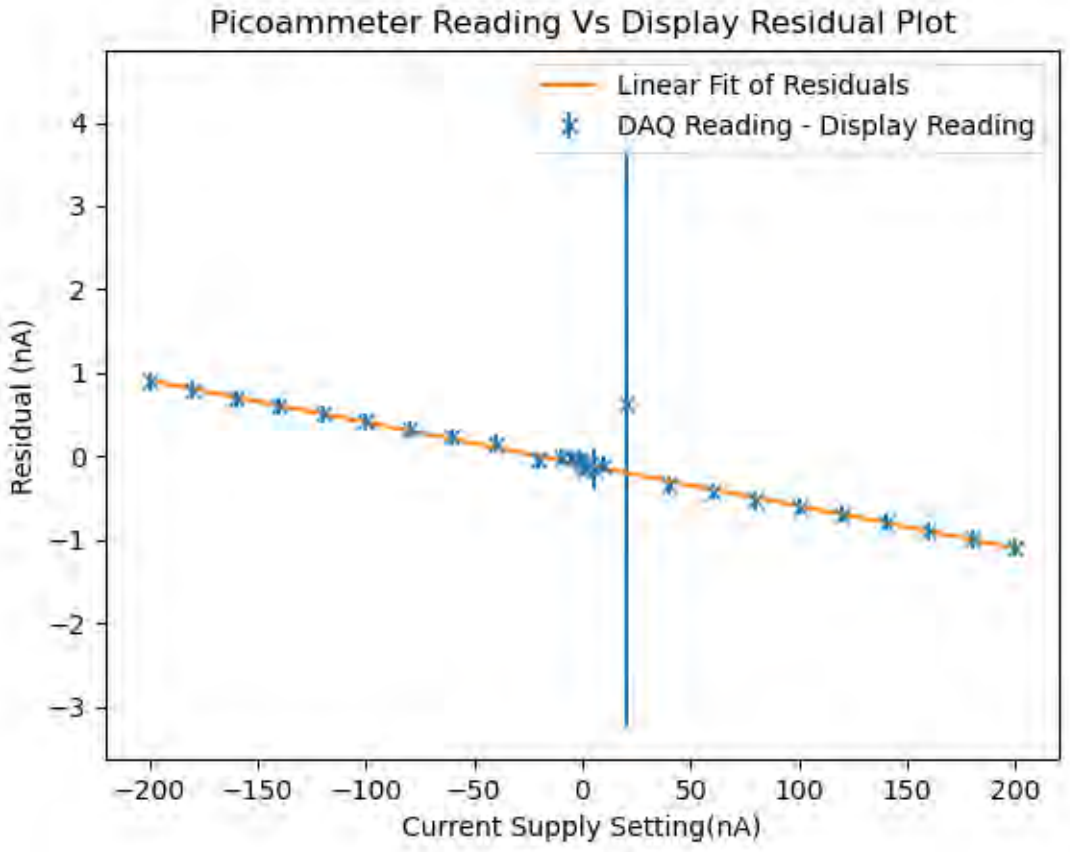

the voltage analog output. As such, the uncertainty was taken to be .5% of the measured current, in accordance with the study done on the residual between the picoammeter display and the analog output reading.

for the -200 to 200 nA scans, the graphs looked linear, and a fit was taken of the slope of applied current to measured current.

Cutoff behavior was observed for the -2 to 2 mA scans however. The maximum current measured was taken as the cutoff voltage

Below is a table of the these values:

These slopes being less than one were an issue, since what was measured on the picoam-

Figure 6.26: Protection Circuit Utilizing Resistors to Determine Current Cutoff

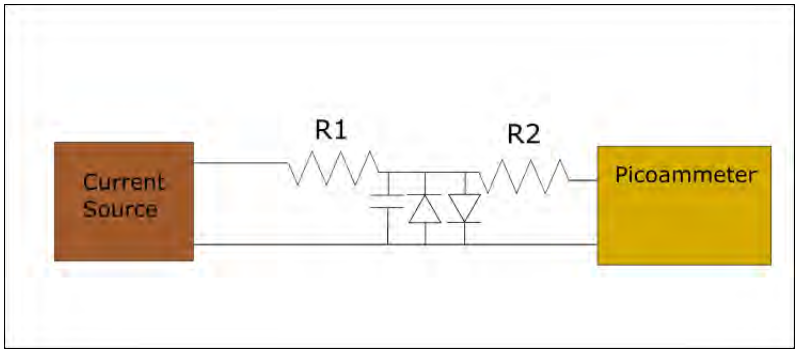

Table 6.11: Cutoff and Linear Values

Resistance	Slope (Linear Region)	Maximum Measured Cutoff Current
300 MΩ	.000371 ± .000002	1.76 nA
100 MΩ	.001111 ± .000004	9.23 nA
300 kΩ	.273 ± .001	1764 nA
100 kΩ	.530 ± .002	5279 nA

meter did not match the current actually sent to the circuit. A measurement of 1 pA with a 100 MΩ resistor installed would actually correspond to 1 nA of current. However, it was still desired that the cutoff current be kept low. The solution to this was to replace the diodes with ones with different specifications. The 5.0A TVS diodes were replaced with 1N3595 diodes.

Specification	5.0A TVS Diode	1N3595 Diode
Manufacturer	Littlefuse	Fairchild/Onsemi
Direction	Unidirectional	Unidirectional
Breakdown Voltage	6.4 - 7.0 V @ 10 mA	150 V @ 100 μA
Forward Voltage	No Information	.52 - .68 V @ 1.0 mA

A similar test was then run for the setup with the 5.0A TVS diodes, except this time the 1N3595 diodes were used, and the R1 resistor was replaced with a 100 MΩ resistor. As this resistor was in series with the rest of the circuit, it was not believed that it would have

Figure 6.27: Linear Region for 100 kOhm Resistor

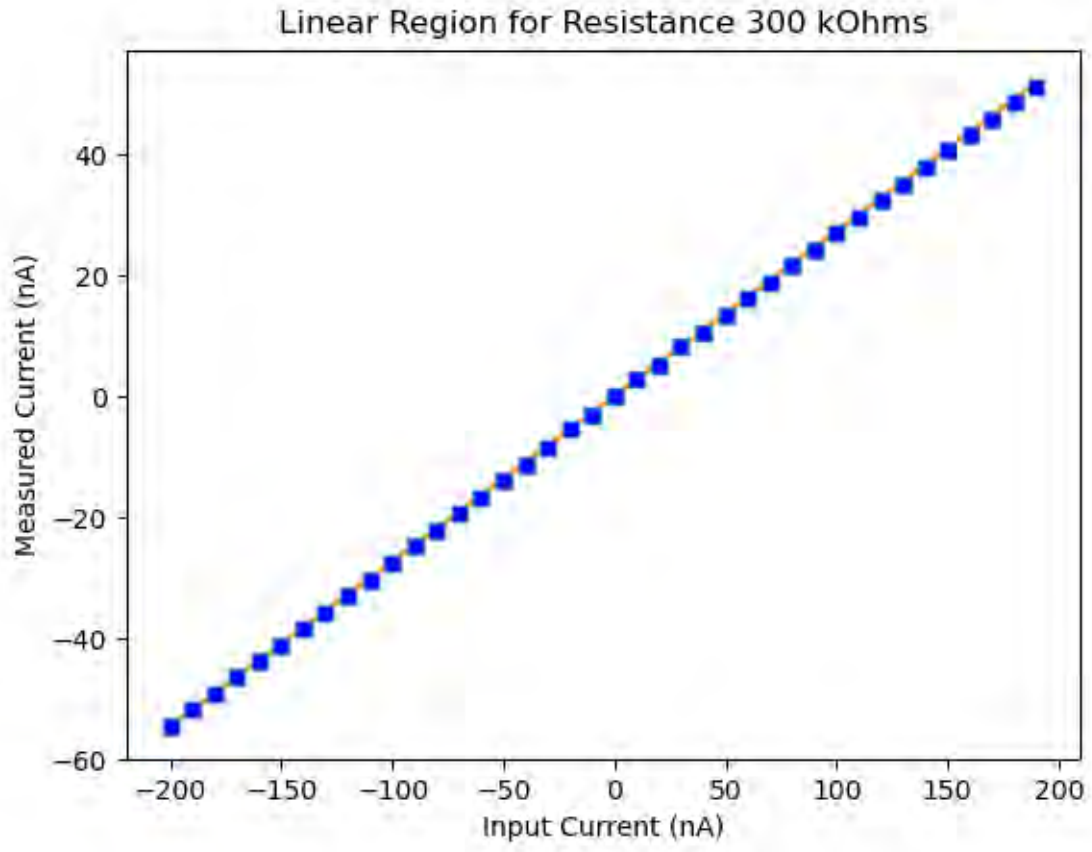

any effect other than to increase the voltage necessarily put out by the current source, which was not relevant. The test was run for R2 values of 100 MΩ and 200 MΩ. The slopes were determined by a range from -.2 to .2 nA, and the cutoff from a range from -8 to 8 nA. The results are below.

Table 6.12: Results for Protection Circuit with 1N3595 Diode

Resistor	Slope	Cutoff Current
100 MΩ	.945 ± .001	2.28 nA
200 MΩ	.889 ± .007	1.17 nA

With these new diodes, the cutoff currents are again in the nA range, but with a slope

Figure 6.28: Cutoff Region for 100 kOhm Resistor

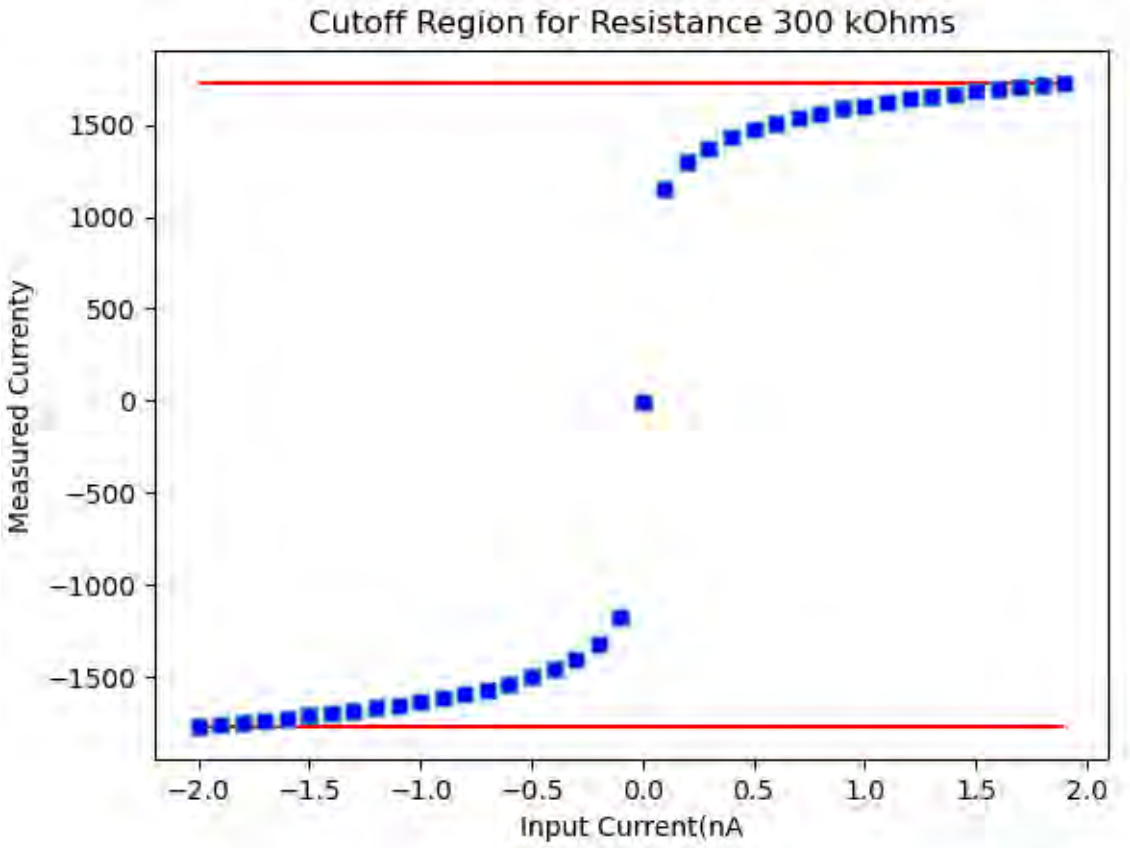

much closer to 1. It may be desired to use smaller resistors, which will get a slope even closer to 1, but with a slightly higher cutoff current.

Chapter 7. Atomic Beam Fluorescence Studies

7.1 Increased Demand of Radium

Ra-225 has been established as being an ideal candidate for fundamental symmetries research. Its usefulness, however, goes beyond pure discovery research, and goes into medicinal purposes as well. This makes procuring it for fundamental physics research difficult, since medical research takes clear priority for the distribution of available Ra-225. With the FRIB coming online, and the radioactive beam dump nearing operation, a new source of Ra-225 should be available. The amount of Ra-225 created, while unfortunately not enough to contribute to medical research, should still be enough for fundamental symmetry research.

7.1.1 Ac-225 Targeted Alpha Therapy

Ra-225 decays through β^- emission, resulting in Ac-225. The decay chain of Ac-225, before reaching stable Bi-209, contains 4 α decays and 2 more β^- decay.[5]

Figure 7.1: Decay chain of Th-229. Figure taken from [5].

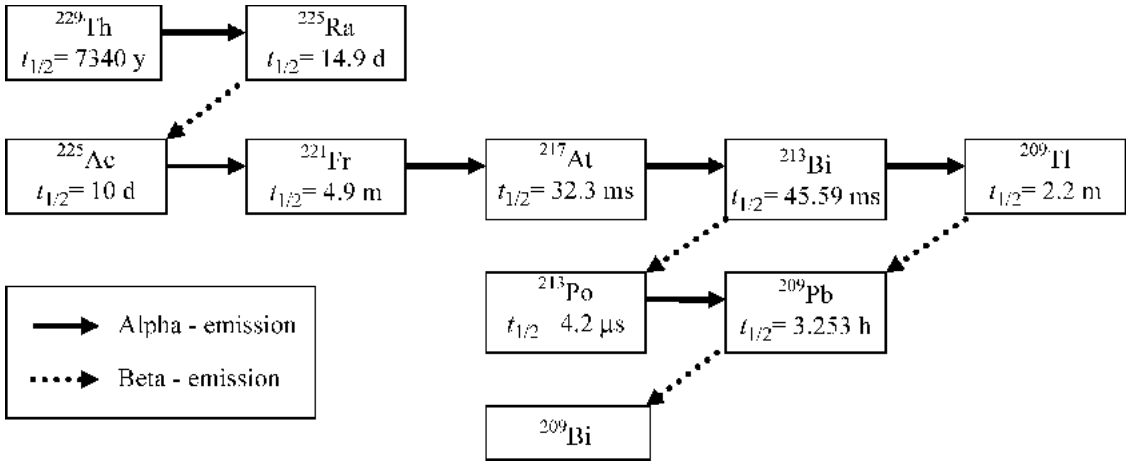

This decay chain makes Ac-225 an ideal candidate for Targeted Alpha Therapy (TAT). TAT uses alpha emitters for killing cancer cells, which has advantages over other kinds of radiation. The "short range of alpha radiation in human tissue correspond[s] to only a few cell diameters,", which "allows the selective killing of targeted cancer cells while sparing surrounding healthy tissue." Furthermore, "the high energy of alpha radiation of several MeV and its associated high linear energy transfer leads to highly effective cell killing."[6].

Figure 7.2: Progression of Ac-225 cancer treatment. Image taken without permission from [6].

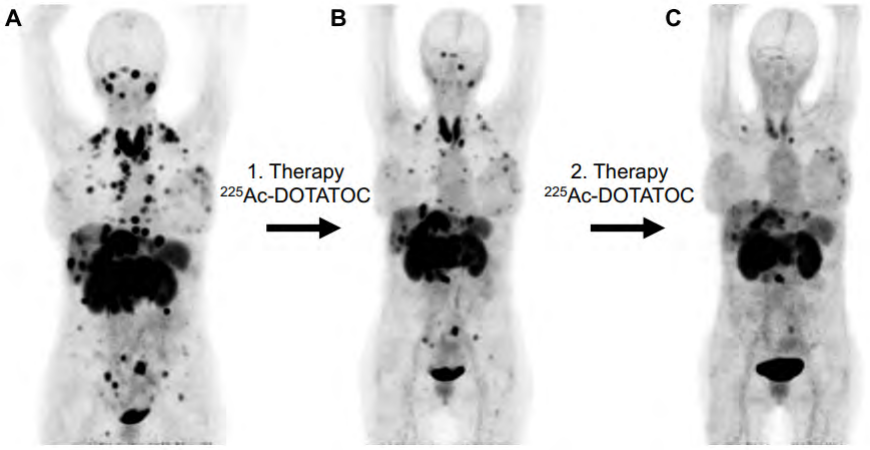

Promising results of TAT using Ac-225 have shown success in treating "difficult" cancers. [6] This, fantastically, has caused a great deal of interest in Ac-225 as a medical isotope. As a result, Ra-225 for fundamental symmetries measurements is in short supply from our normal sources. For this reason other sources from which to procure Ra-225 must be investigated..

7.1.2 Tests of Fundamental Symmetries

The Ra-225 isotope is the backbone the backbone of our experiment, due to its octupole deformed nuclear structure. This gives it a large nuclear Schiff moment, as well as a nearly degenerate parity doublet. Both of these properties together give it an enhancement in the

sensitivity to new physics in any EDM measurement performed upon it. However, Ra-225 also has a 14-day half life, making it a rare isotope. This makes sources of Ra-225 few and far between.

7.2 Sources of Radium

The procurement of Ra-225 has proven to be a particularly challenging problem to overcome in our experiment. We have looked to a variety of sources for the atoms for our measurement:

7.2.1 Old Source of Radium

In the two previous data runs of the RaEDM experiment, the Radium-225 used was sourced from the National Isotope Developement Center at Oak Ridge National Laboratory (ORNL). The first data run used two separate samples, one 3 mCi, and one 6 mCi. The second data run was done with a single 9 mCi sample of Ra-225[36]. The origin of this radium at Oak Ridge National Laboratory is from a source of Thorium-229, which has a half life of 7,917 years. This relatively long-lived nucleus then slowly decays into Ra-225, which it is then harvested from. It is this source that now supplies ongoing medical research. Other sources are thus needed.

7.2.2 Ra-223 as a Surrogate

For a time, Radium-223 was explored as a potential substitute. This could still be procured from ORNL for fundamental physics experimentation. It has a similar octupole deformation to Radium-225, which gives it a similar enhancement factor for EDM measurements. However, there are reasons why it is less than ideal. Its half life is only 11 days, instead of 14,

and it has a nuclear spin I = 3/2 instead of 1/2. This not only makes adds more hyperfine F levels to its excited states, but it also introduces hyperfine B coefficients into the theory of the hyperfine splitting. This made trapping it a challenge, as some of these spectroscopic properties for the necessary Ra-223 levles have never been measured. An effort was made to find these values, but supply of Ra-223 was also interrupted at ORNL, and this came to a halt.

7.2.3 Th-229 Source

A recent effort to laser cool and trap Ra-225 ions at UC Santa Barbara [50] was able to use Ra-225 for its experiment, through using an oven containing Th-229. 8 μCi of Th-229 was loaded into a titanium crucible, and heated to 350-400 C. This resulted in a long-term oven of Radium-225, as the Thorium would continuously decay into Radium. However, the resulting number of Radium-225 ions trapped was 12 on average, which while sufficient for measuring the energy levels and states of the Radium-225 ion, is rather low for the number of atoms we need for an EDM experiment. This could be improved by increasing the amount of Th-229 put into the oven, but there are limits to how much we can put in due to the resulting increase in radioactivity. Any source of Th-229 we put in will be at least slightly contaminated with other isotopes of Thorium, many of which have significantly smaller half-lives.

Table 7.1: Decay Properties of Thorium Isotopes

Isotope	Half-Life	Decay Mode	Dps in 1 ng of Material
Th-229	7916 years	α	7.25 Bq
Th-228	1.9 years	α	30.4 kBq

As can be seen, a sample of Th-229 even 1% contaminated with Th-228 will have over 97.6% of its total activity come from the Th-228. With activity being a key safety concern,

this greatly reduces the amount or Th-229 that can be put in an oven given an upper limit of activity.

7.2.4 Isotope Harvesting at FRIB

The FRIB at Michigan State University is capable of accelerating atoms to energies of over 200 MeV/u, for the purpose of the creation of rare isotopes. These are created by accelerating a primary beam of ionized atoms to these energies, and hitting them against a stationary target. After the target, an apparatus is in place to perform measurements on secondary beam that results. There are atoms created which are not a part of this secondary beam, however, which are deposited in a water beam dump. This beam dump has been proposed as a potential source of rare isotopes, and the concept of harvesting isotopes from it has been proven [51]. It has been mostly completed, and is awaiting operation. Once in operation, with the right beams such as Uranium and Thorium, Ra-225 will be available once more.

7.2.5 Forming Atomic Beams from Harvested Isotopes

Ra-225 will be harvested from the FRIB beam dump dissolved in water, alongside other products of the accelerator. From there, radiochemistry can be done to isolated the radium, and present it to us as Radium Nitrate - the form that it arrived in from Oak Ridge National Laboratory. To form an atomic beam from the radium, the same process would be used as for previous Ra-EDM measurements [36]. The Radium Nitrate is dried upon a square of aluminum foil, alongside two 25 mg pieces of metallic barium. The aluminum foil is then crumpled up, and placed inside a crucible, where it is inserted into the apparatus and heated to 500 C. Eventually, Radium will begin to flow out of the crucible, at which

point it is "cracked." Then, smaller flow rates of radium can be created by turning down the temperature of the oven. The exact process by which this reaction occurs is not well understood. Notably, the temperature at which a "crack" occurs varies between oven loads.

Table 7.2: Cracking Temperatures of Various Oven Loads

Date	Load	Crack Temperature
02/28/2020	1 μCi Ra 226	528 C
07/23/2020	First 223 load	525 C
03/11/2021	2 μCi Ra 226	524 C
04/16/2021	2 μCi Ra 226 and 10 mCi Ra 223	

Due to the nature of our experiment, the more efficiently we can create a beam of radium, the more atoms we will be able to measure. As a consequence, our statistical sensitivity will improve. It is entirely possible that a more efficient chemistry process than what we currently use exists. For this purpose, an Atomic Beam Fluorescence (ABF) setup has been built at Michigan State University, to study different chemical processes using non-radioactive chemical surrogates. Experimentation can be done where a known amount of Calcium is dissolved in water, and prepared by FRIB radiochemistry personnel in the form of Calcium nitrate. This has already been demonstrated with high efficiency [52]. It can then be loaded into the oven with aluminum foil and barium, in the same procedure as for radium, and hopefully have a beam of atomic Calcium be produced when heating. By measuring the atomic flux of the Calcium beam being emitted, and knowing the amount of Calcium initially put in, the efficiency by which an atomic beam is created can be characterized. In addition, with non-radioactive sources, different chemical procedures can be tested. Calcium can arrive in other forms, such as Calcium Chloride, and the metallic Barium can be replaced with other elements as well. In this way, the efficiency can be measured for different chemical loading procedures, and any improvement in efficiency can be identified to be tried for Radium.

Test studies have been done with metallic calcium, and a signal has successfully been seen. Our goal at this stage, before we begin testing other processes, is to refine our setup to be able to resolve atomic fluxes at the 10^8 atoms per second level. A variety of studies were performed to characterize the current lowest atomic flux currently visible, and a summary is now given.

7.3 Metallic Calcium Fluorescence Studies

Scans were done on different days, under varying conditions. For each day, scans were done at varying powers, and the area under the fluorescence peaks was characterized. A more detailed description of the ABF apparatus is given below:

7.3.1 Experimental Setup

Our apparatus consists of an effusive oven, attached to a 6-way cross viewing chamber. The oven creates the atomic beam, and the 6-way cross enables atomic fluorescence. The fluorescence is enabled by an MSquared laser system, and collected by an Single Photon Detector. The whole measurement is performed by a Labview program.

The particulars of each system is now discussed.

7.3.1.1 Effusive Oven

The effusive oven currently installed is the second fabricated by MSU. The first was shipped to the Massachusets Institute of Technology, for use with their study of Radium Fluoride. The one currently in use was custom fabricated, based on designs and lessons learned from making the first one. It was fabricated in the machine shop at the Biophysical Sciences

Figure 7.3: Overview of the Laser Apparatus

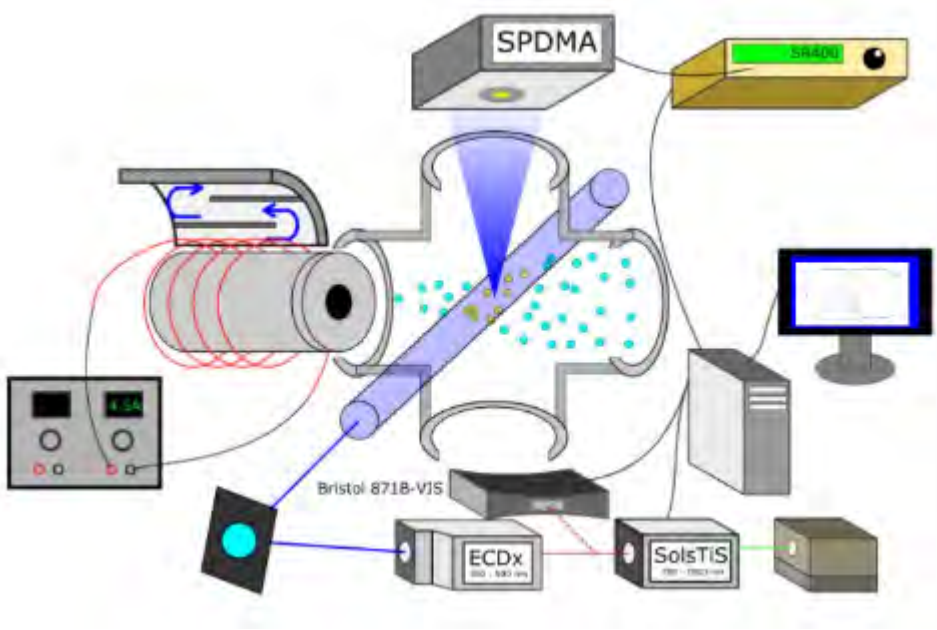

building at Michigan State University. A detailed description of its assembly will be in the appendix, but a brief overview is provided here. The overall shell of the oven is a 4.5"-flange 6-way cube. One of the flanges contains a 3" long 4.5"- 2.75" reducing nipple, into which the crucible and nozzle is inserted.

Figure 7.4: Titanium Crucible for Oven Loading

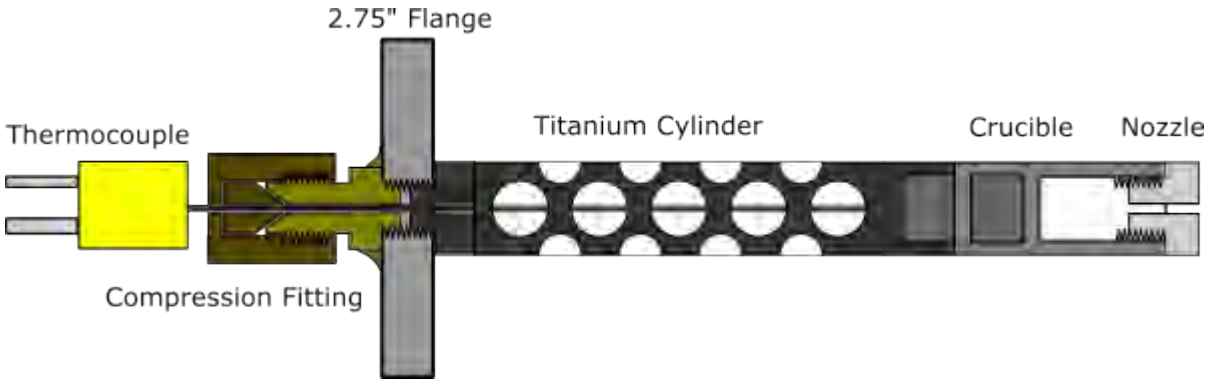

Another flange perpendicular to this provides a cooling jacket, designed to be placed right at the center of the cube. The water lines are cooled using a chiller set to 20 C. A vacuum

Figure 7.5: Atomic Beam Effusive Oven Diagram

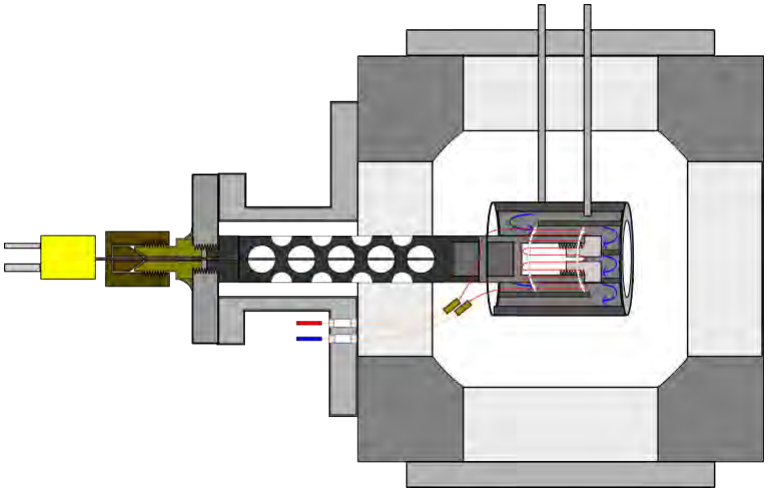

pump assembly and ion gauge are also attached, so as to pump down to vacuum. Within the vacuum gauge is sat a Tantalum wire that serves as a filament. This is woven through the holes of two ceramic discs, so that filament surrounds the crucible, but no part of of the filament comes into contact with the outer oven. The filament is connected to feedthroughs welded into the reducing nipple, which lead to a power supply from which current can be run.

The temperature of the crucible is monitored in real time with a K-type thermocouple. The relationship between oven current and stable oven temperature was studied, and can be seen below:

The points on this plot can be summarized on the table below:

7.3.1.2 6-way Cross

Attached to the oven via a 4.5" - 2.75" reducing flange is a 6-way cross. This is the chamber where the fluorescence takes place.

Directly across from the 6-way cross is a blank flange. On either side, perpendicular to

Figure 7.6: Oven Temperature Versus Power Supply Current

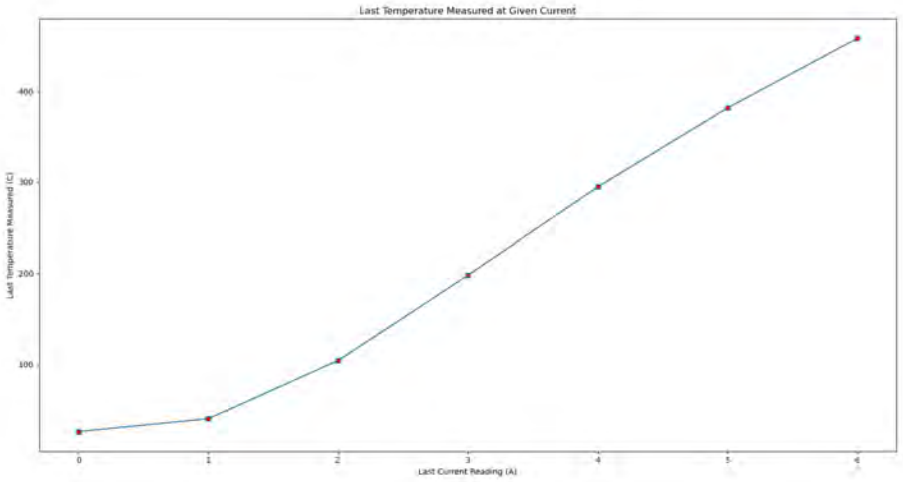

Table 7.3: Corresponding Temperatures for Currents

Current (A)	Temperatures (C)
0.0	26.0
1.0	40.2
2.0	104.2
3.0	198.0
4.0	294.7
5.0	381.5
6.0	458.2

the atomic beam, are two anti-reflection coated viewports. These allow for laser light to be directed in and out, and overlap with the atomic beam. On the top of the 6-way cross, perpendicular to both the atomic beam and laser beam, is the 422nm filter and Thorlabs SPDMA single photon detector that we use to count the fluorescence count rate. The SPDMA detects individual photons hitting it, and outputs a proportional number of TTL signals that requires counting. The 422nm filter is used to filter out background light that is off-resonance from the transition we are actually trying to fluoresce.

Figure 7.7: Full Diagram of ABF Setup

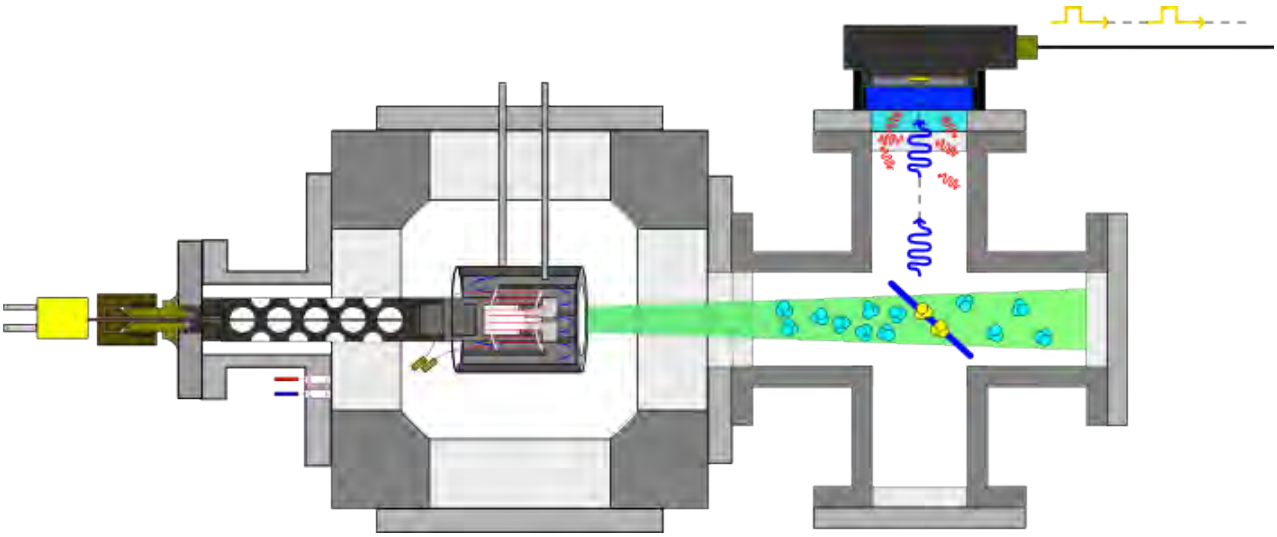

7.3.1.3 Laser System

The laser beam sent into the 6-way cross is created from a laser system consisting of a 532 nm Lighthouse Photonics SPROUT pump laser, an MSquared SOLSTiS Titanium-sapphire laser capable of outputting 700 - 1000 nm light, and an MSquared ECDX doubling cavity, capable of outputting 350 - 500 nm of light. To fluoresce Calcium, both the SOLSTiS and ECDX had to be utilized to produce light at 422nm wavelength. A table of various isotope peaks is given here:

Table 7.4: Relevant Calcium transitions

Isotope	Abundance	I	Transition	Vacuum Wavelength (nm)	Wavemeter Reading (nm)
Ca-40	.96941	0	${}^1S_0 \rightarrow {}^1P_1 (F = 0 \rightarrow 1)$	422.7917	845.5834
Ca-44	.02086	0	${}^1S_0 \rightarrow {}^1P_1$	422.7912	845.5825
Ca-42	.00647	0	${}^1S_0 \rightarrow {}^1P_1$	422.7915	845.5830
Ca-48	.00187	0	${}^1S_0 \rightarrow {}^1P_1$	422.7908	845.5816
Ca-43	.00135	7/2	${}^1S_0 \rightarrow {}^1P_1 (F = 7/2 \rightarrow 5/2)$	422.7913	845.5826
Ca-43	.00135	7/2	${}^1S_0 \rightarrow {}^1P_1 (F = 7/2 \rightarrow 7/2)$	422.7913	845.5827
Ca-43	.00135	7/2	${}^1S_0 \rightarrow {}^1P_1 (F = 7/2 \rightarrow 9/2)$	422.7914	845.5828

Table 7.5: Relevant Calcium transitions

Isotope	Transition	Detuning from Ca-40 (GHz)	Reference
Ca-40	$^1S_0 \rightarrow ^1 P_1(F = 0 \rightarrow 1)$	0	[53]
Ca-44	$^1S_0 \rightarrow ^1 P_1$	.7738	[53]
Ca-42	$^1S_0 \rightarrow ^1 P_1$	.3931	[53]
Ca-48	$^1S_0 \rightarrow ^1 P_1$	1.513	[53]
Ca-43	$^1S_0 \rightarrow ^1 P_1(F = 7/2 \rightarrow 5/2)$	.6788	[53], [54]
Ca-43	$^1S_0 \rightarrow ^1 P_1(F = 7/2 \rightarrow 7/2)$	.6287	[53], [54]
Ca-43	$^1S_0 \rightarrow ^1 P_1(F = 7/2 \rightarrow 9/2)$	.5554	[53], [54]

Table 7.6: Hyperfine Coefficients of Ca-43

Ca-43	Value	Reference
A Coefficient	-15.54 MHz	[54]
B Coefficient	-3.48 MHz	[54]

The isotope shifts and A and B coefficients for the Ca-43 isotope are given here:

7.3.1.4 Optical Setup

In order to properly fluoresce Calcium, simply creating the beam was not enough - it had to be guided to the interaction region of the atomic beam. The optical setup to do this went through several iterations, labeled setups 1-5. The optical system consisted of two separate parts. The first was directly in front of the laser, designed to couple the output beam into the fiber. It was also used to adjust the power sent into the fluorescence chamber, with any excess power being sent to a beam dump. A diagram is shown below:

This optical setup remained unchanged during the studies. The optics after the fiber, which were directly on the ABF stand, went through various changes. This optical setup served multiple purposes: it has to depolarize the beam by sending it through a depolarizer, ideally with as large a beam as possible. Then, it has to shrink the size of the beam with

Figure 7.8: Laser Setup before Fluroescence Stand

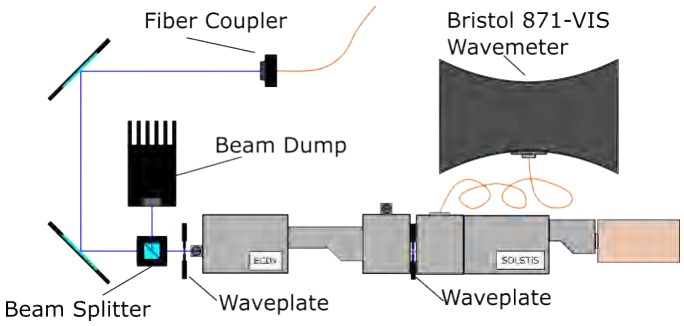

a series of telescoping lenses, before sending a collimated beam through the 6-way cross. Finally, the beam exiting from the 6-way cross has to be focused onto a powermeter, so a measurement of the power can be made.

5 different setups in total were used over the course of the scan studies. A brief table is given here:

Table 7.7: Setups of different scans

Setup	Description
Setup 1	Same as Setup 2, but elastic alignment tools were left in place for the scan, likely increasing the background significantly
Setup 2	See 7.9. Uses two telescopes, one with 100/-50 mm telescoping pair, and one with 250/150 mm telescoping pair
Setup 3	On 06/26/2024, black acktar tape was installed for background reduction purposes. This involved removing the ABF apparatus from its stand with the optical components, and putting it back, altering the optical components. After doing background scans with this setup, it was noticed that the laser was not aligned well through the center.
Setup 4	After the background scan was done on 07/03/2024, it was noticed that the laser was no longer aligned through the center, due to moving the apparatus. It was realigned through the center, giving setup 4.
Setup 5	To reduce the size of the beam going through the 6-way cross, the second 250/150 mm telescoping lenses were replaced with a single 500 mm lens. See 7.10 for a diagram.

Figures for the two main overall setups are given here:

Throughout these studies, the size of the beam was difficult to control. The fiber used to move the light onto the ABF stand was a 40 m long multimode fiber, meaning that different modes could be coupled into it. This caused wide variations in the beam profile. A study was done with simulation code to determine the effect that the beam width has on the laser

profile, and the conclusion was that it was minimal. More detail on this simulation will be given later.

The lasers are controlled by software native to them on the computer. In order to control the lasers, lock them to the wavemeter, and simultaneously record the wavelength and count TTL signals, software had to be created.

7.3.1.5 Software

The measurement software uses LabVIEW version 2022. The software I made not only takes data, but it also locks the laser to the wavemeter. In order to figure out how to do this, I had to first make a program that strictly serves the purpose of locking the laser. This program, LockingFluorescenceCombinedV7, is described in detail in the appendix, but a brief inteview will be given here. The interface of the program is shown on the next page:

Figure 7.9: Laser Apparatus Used for Setup 2

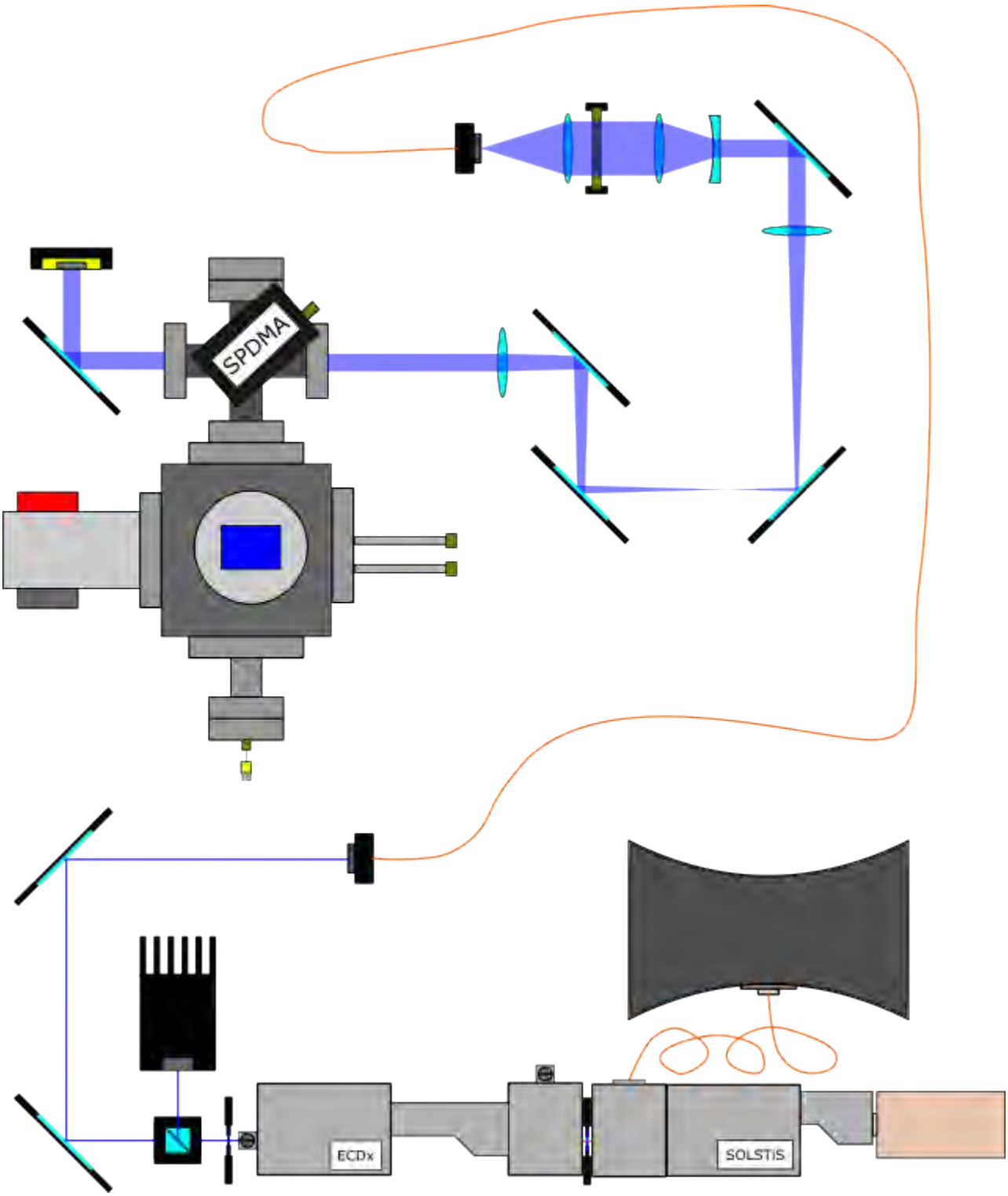

Figure 7.10: Laser Apparatus Used for Setup 5

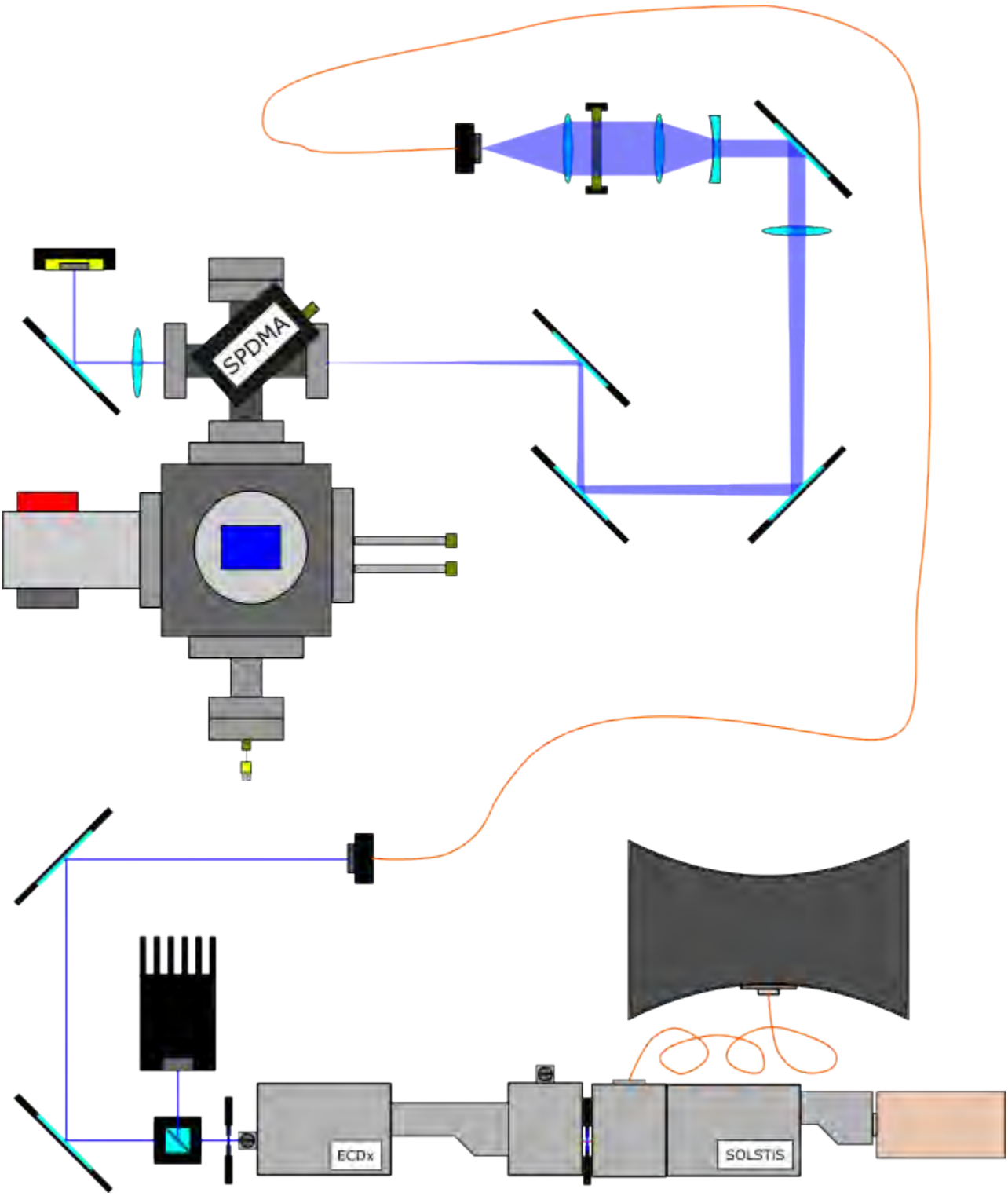

Figure 7.11: Front Panel of Fluorescence Measurement Software

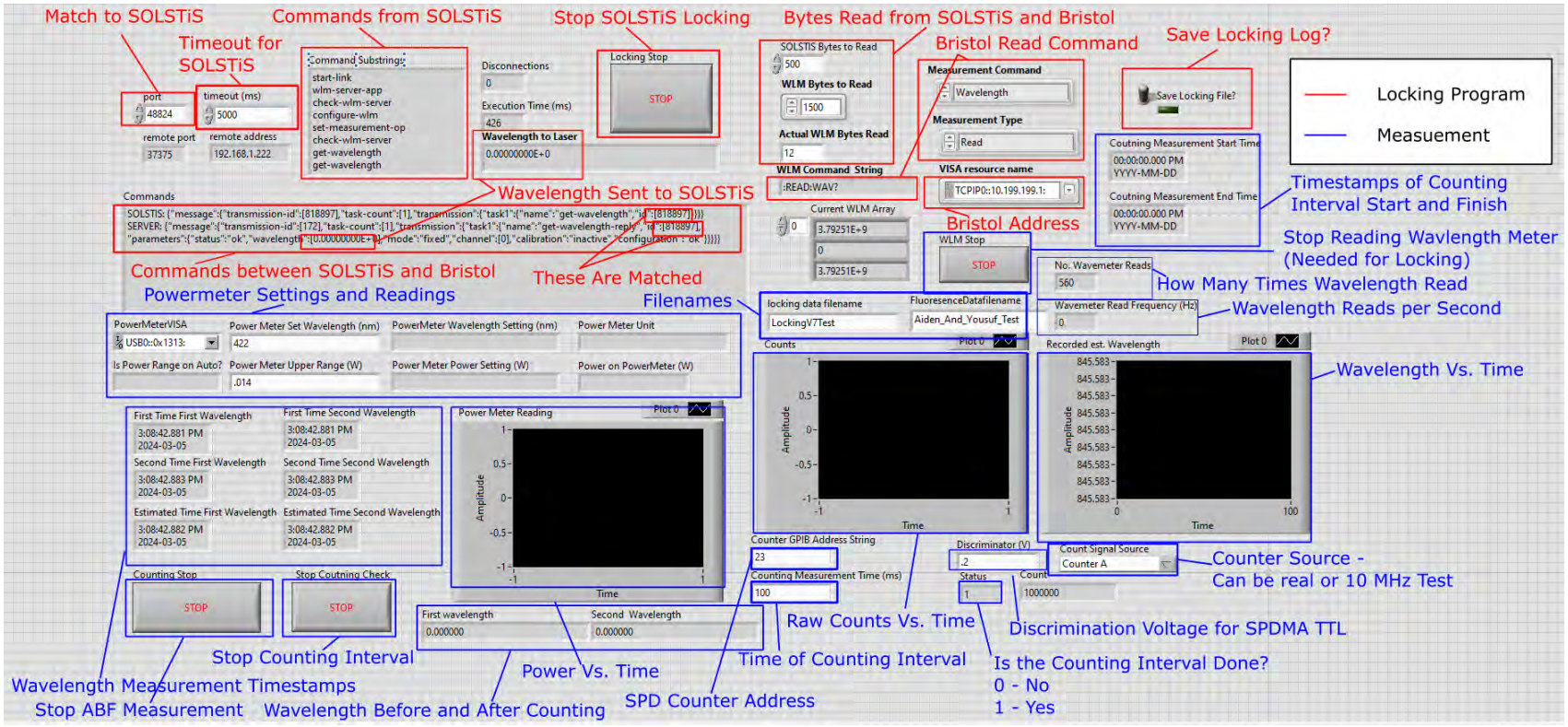

The program essentially runs by constantly reading from the wavemeter, and updating a corresponding local variable. Every time the value is needed, either because it's been asked by the laser locking or it needs to be logged, this local variable is referenced, which holds the most recent measurement. Logged into the data at each step are the results of the counting interval, two wavelength measurements, four timestamps, and a laser power reading.

The timestamps are provided by the computer, the wavelengths from the wavemeter, the power from a PM1000 Thorlabs power meter, and the counting interval from an SRS400 Counter. The counter takes inputs from the SPDMA, and counts them using a 10 MHz internal clock. This clock can also be used to test the counter. The length of the counting interval can be set in milliseconds. It is reset every time upon program start, and the resetting process takes roughly 5 seconds to occur. Once the reset is done, the counter is automatically fed the necessary commands to configure the settings needed, and the counting measurements start. Typically, 100 ms counting intervals are used. Each data point is separated in time by roughly 110 ms, so it seems that all the other data taking operations take around 10 ms. This means that the program is actually measuring the counts 10% of the time. This seems to be fine, but does limit how short the counting interval should be. A counting interval of 10 ms, for example, would be non-ideal, since only 50% of the time would the measurement actually be counting.

7.3.1.6 Typical Experimental Values

With so many instruments, it can be hard to keep track of what each needs to be set to. A summary table is given below:

Table 7.8: Summary of Parameters for SPDMA

SPDMA		
Dark Count Rate	Photon Detection Efficiency @ 422 nm	Sensor Diameter
$\approx$ 100 Hz	89.4% (Rough Estimate)	500 μm
Maximum Count Rate	TTL Output Height (Low)	TTL Output Height (High)
20 MHz	0 V	3.5 V

Table 7.9: Summary of Settings and Parameters for SR400 Counter

SR400		
Input (set)	Timing Clock (set)	Counting Mode (set)
Counter A	10 MHz Internal Clock	A, B separate
Discriminator Voltage (Typical)	Counting Interval Length (Typical)	Reset time
.2 V	100 ms	$\approx$ 5s

Table 7.10: Summary of Settings and Parameters for Chillers

Chillers	
ABF Cooling Jacket Chiller Temp (Typical)	SOLSTiS Chiller (Typical
20 C	20 C

Table 7.11: Summary of Settings for Laser

SOLSTiS		
Scan Start	Scan End	Scan Rate
845.581 nm	845.585	5 MHz/s
ECD Lock?	Laser Scan Doubled Light Max Power through Fiber	Sprout Power (set)
ON	20 mW	18 W

Table 7.12: Summary of Settings for Current Source for Oven

Current Source	
Current and Voltage Range	Source Setting
8A, 20V	Current Source

7.4 Data Summary

Five fluorescence studies were done, each for a particular day. Each fluorescence study involved performing a fluorescence scan under varying powers. The integrated fluorescence signal as a function of laser power is linear in the low power regime. By getting a value for this slope, it can be compared to simulated values to get a measurement of the atomic flux. Other studies were done to reduce the background signal of our measurement. A summary table is given below:

Table 7.13: Summary of Spectroscopic Studies

Purpose	date	T	Power Range (# of scans)	Background Suppression	Laser Beam Profile	Background Power Slope (First Method)	Scan Rate
-	-	C	mW (-)	-	-	kHz / mW	MHz/s
Background	05/10/2024	Room Temp	$1 \rightarrow 8$ (5)	422 nm Filter	Setup 2	465.4 ± 2.7	2
Background	07/03/2024	Room Temp	$1 \rightarrow 12$ (5)	422 nm Filter, Black Aktar Tape	Setup 3	$93.28 \pm .85$	5
Purpose	date	T	Power Range (# of scans)	Background Suppression	Laser Beam Profile	Low Power Curve Area Slope	Scan Rate
-	-	C	mW (-)	-	-	GHz · kHz / mW	MHz/s
Ca High Flux	05/02/2024	457	$.5 \rightarrow 4$ (5)	422 nm filter	Setup 1	785.3 ± 64.6	2
Ca High Flux	05/10/2024	380	$.5 \rightarrow 8$ (3)	422 nm filter	Setup 2	96.08 ± 2.94	2
Ca High Flux	07/03/2024	457	$3 \rightarrow 12$ (4)	422 nm filter, Black Aktar Tape	Setup 4	3503 ± 365	5
Ca Low Flux	07/08/2024	338	$1 \rightarrow 7$ (5)	422 nm filter, Black Aktar Tape	Setup 4	$1.894 \pm .103$	5
Ca Low Flux	07/22/2024	338	$3 \rightarrow 16$ (8)	422 nm filter, Black Aktar Tape	Setup 5	$1.672 \pm .171$	5

More detail will now be given, starting with how the integrated signal was characterized.

7.5 Fluorescence Signal Analysis

For each scan, the fluorescence count rate, power reading, and laser wavelength are all taken in real time, through the software previously discussed. Each raw data file contains data taken both before the scan, and after. This excess data must be cut out for a proper count rate versus wavelength plot to be made. This requires the actual scan data to be defined.

7.5.1 Defining the Scan Interval

When the raw data file is plotted line by line, the count rate and power look something like this:

The best way to define the scan is to look at the wavelength versus data point index, and use it to custom define the beginning and end of the scan. Since the fluorescence occurs in the middle of the scan, it's not a big deal to exclude the very tail ends of the scan. This ensures all of the data being analyzed is relevant. The wavelength plot looks something like this:

The scan interval is then very clear: It's the section which sees a gradual increase in the wavelength. By selecting two of the indices, one at the very beginning of the scan, and one at the very end, only the relevant data is used. Since the down time in between each scan can change, this has to be done separately for each measurement. If the software was updated to allow for the scan to be controlled from the LABVIEW data acquisition program, it might become possible to only take the scan data. For now though, the LABVIEW program has no idea when the scan starts and ends, so this is necessary.

Figure 7.12: Raw Scan Data File

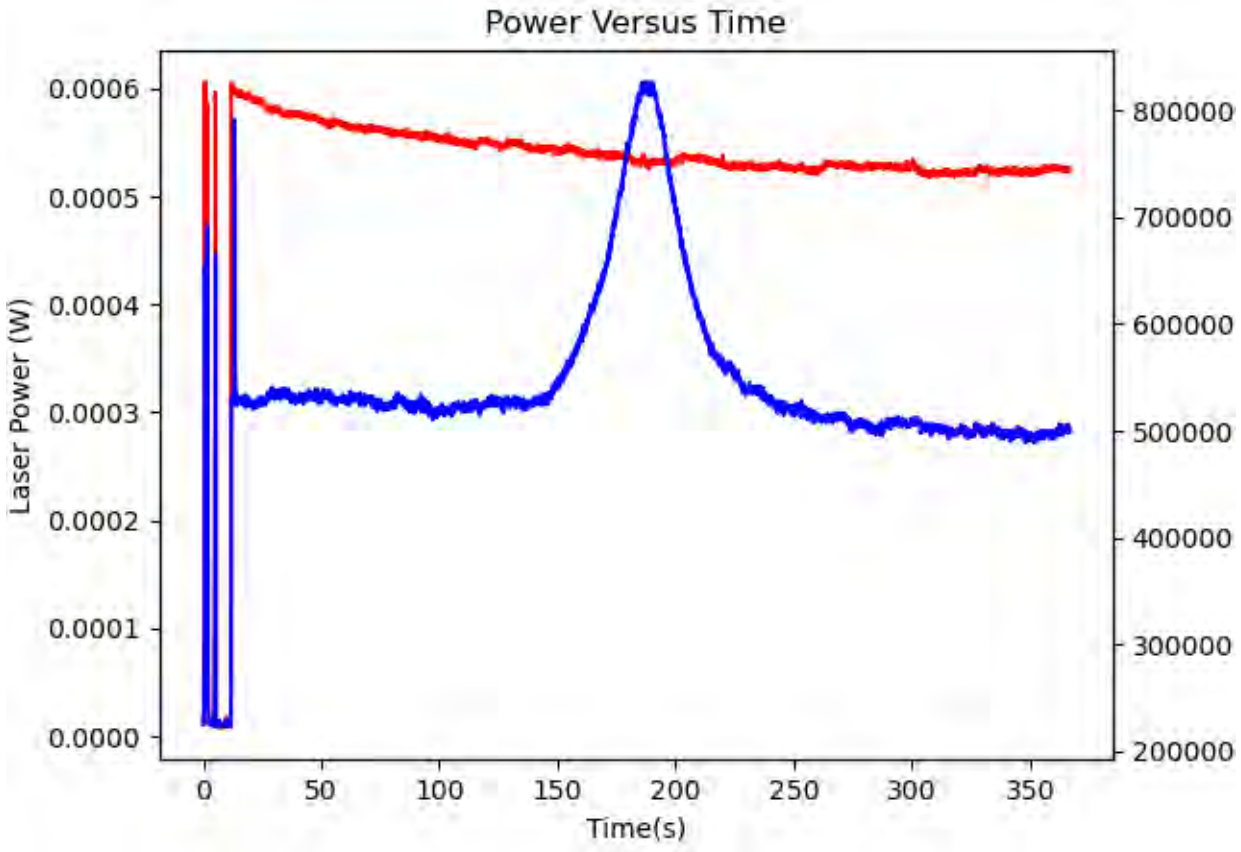

7.5.2 Characterizing the Background Decay

As the scan progresses, the power of the laser decays at what looks like exponential rate. This is an artifact that needs to be taken into account, since the background counts of the signal are modeled to be linear with the laser power:

$$f_{Background}(P) = M \cdot P + C \tag{7.1}$$

where C is the background counts with the laser off, P is the laser power, $f_{Background}$ is the background count rate, and M is the slope in kHz/mW.

Figure 7.13: Scan Wavelength Versus Time

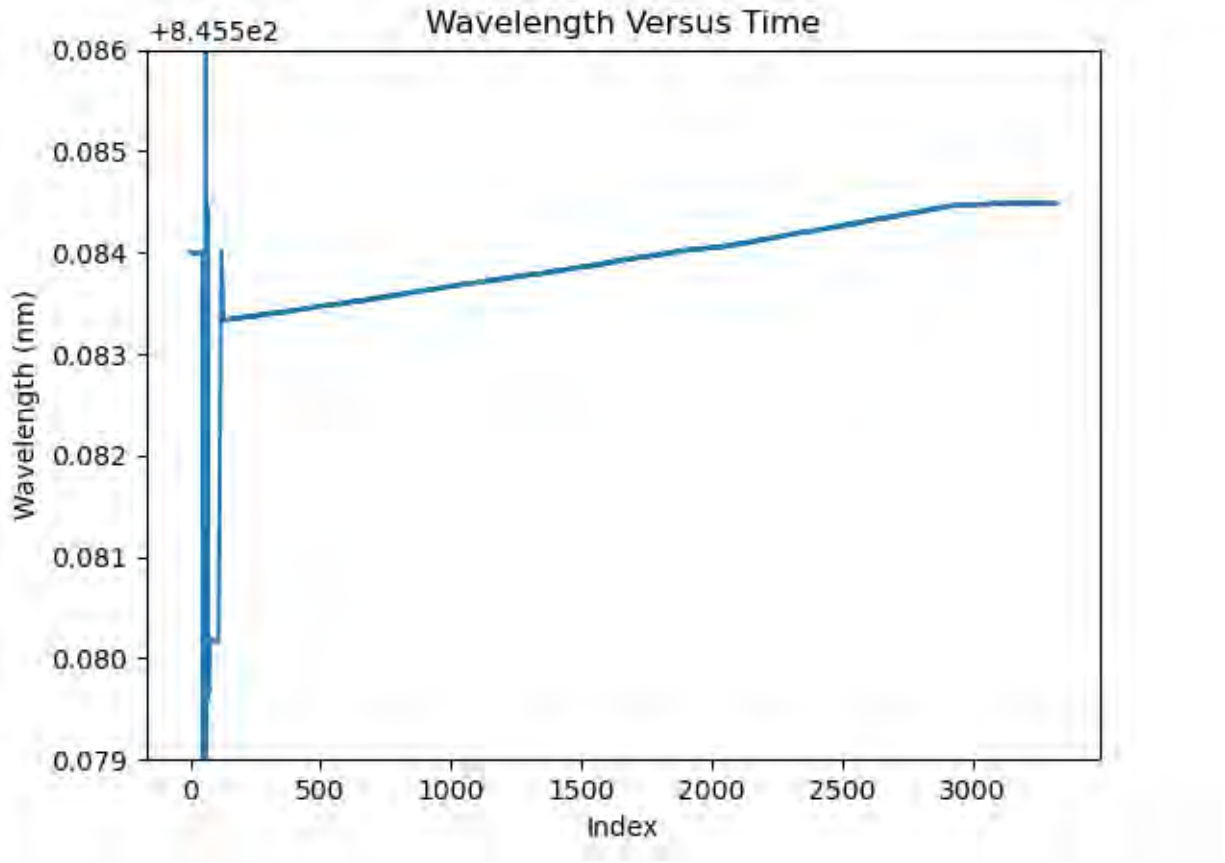

The laser power is modeled to have an exponential dependence on frequency, of the form:

$$P(\omega) = P_0 + Ae^{B\omega} \tag{7.2}$$

The laser power fluctuation varies from scan to scan. It can be relatively small:

In this case, only increasing roughly 10 μW. There are cases where it is quite significant, however:

In this case, the power rises from 2.1 mW to 2.8 mW - an increase of 700 μW, 33% of the power level. This causes a variation in the count rate due to the power level, as can be seen below:

Figure 7.14: Small Power Fluctuation

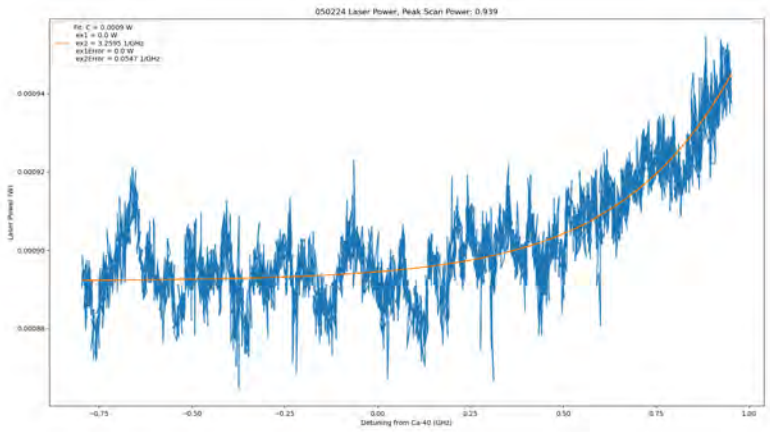

Clearly, the relation between the power and background level is very correlated. Consider now the effect this drift has on the counts. If the P dependence on ω is substituted in:

$$f_{Background}(\omega) = M \cdot P_0 + M \cdot Ae^{B\omega} + C \tag{7.3}$$

many of these variables can be aborbed into a single parameter. Thus,

$$f_{Background}(\omega) = C' + M'e^{B\omega} \tag{7.4}$$

It should be noted that the parameter B remains the same between the power dependence, and the count rate dependence. Thus, by fitting to the power dependence, the exponential decay for the background counts can be derived. The actual count rate as a function of detuning frequency can be seen below:

Figure 7.15: Large Power Fluctuation

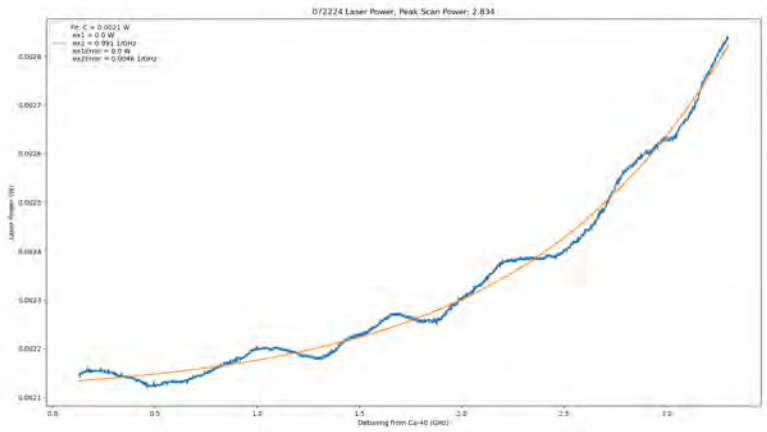

7.5.3 Signal Scan Analysis

The shape of the peak caused by the fluorescence closely matches a Lorentzian profile. The equation fit to the total count rate line shape has the form:

$$f(\omega) = C + De^{B\omega} + \frac{A}{\pi}\frac{\frac{\Gamma}{2}}{(\omega - b)^2 + (\frac{\Gamma}{2})^2} \tag{7.5}$$

where the value of B is taken from the value derived from the power decay. Using this formula, the background counts for the scan can be considered as

$$f_{Background}(\omega) = C + De^{B\omega} \tag{7.6}$$

and the signal curve as

$$f_{Signal}(\omega) = \frac{A}{\pi}\frac{\frac{\Gamma}{2}}{(\omega - b)^2 + (\frac{\Gamma}{2})^2} \tag{7.7}$$

The parameter of interest from scan to scan for the signal curve is the integrated count

Figure 7.16: Raw Scan Data with Large Power Fluctuation

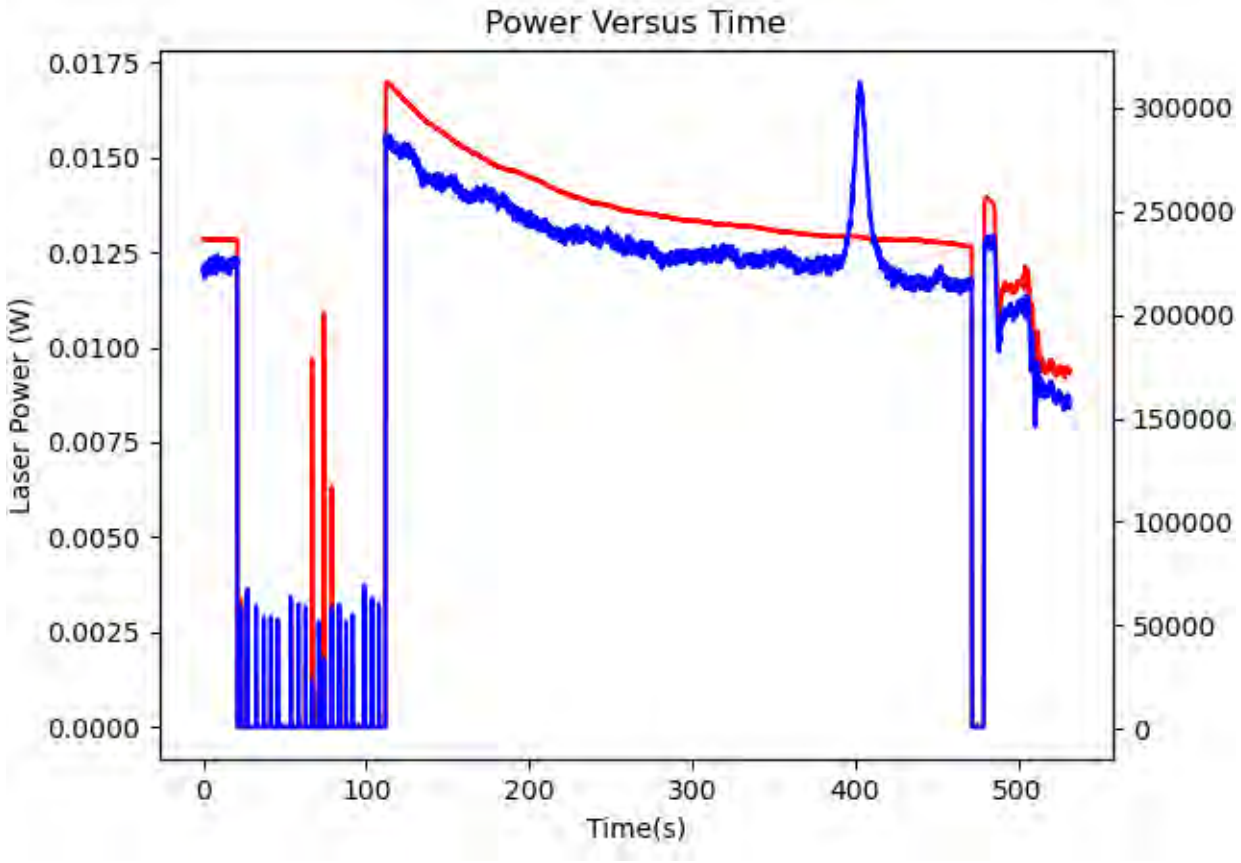

rate under the signal. Conveniently, the Lorentzian function is such that

$$I_{Signal} = \int_{-\infty}^{\infty} f_{Signal}(\omega)d\omega = \frac{A}{\pi}\int_{-\infty}^{\infty} \frac{\frac{\Gamma}{2}}{(\omega - b)^2 + (\frac{\Gamma}{2})^2}d\omega = \frac{A}{\pi}\pi = A \tag{7.8}$$

So, by fitting to the Lorentzian, the area can be easily derived as the value taken by A.

7.5.4 Uncertainty Quantification

To perform the fits, the uncertainty for each count rate and power data point had to be known. For the count rate, this was attempted in two different ways: either with Poisson

Figure 7.17: Exponential and Lorentzian Fit to Scan Data

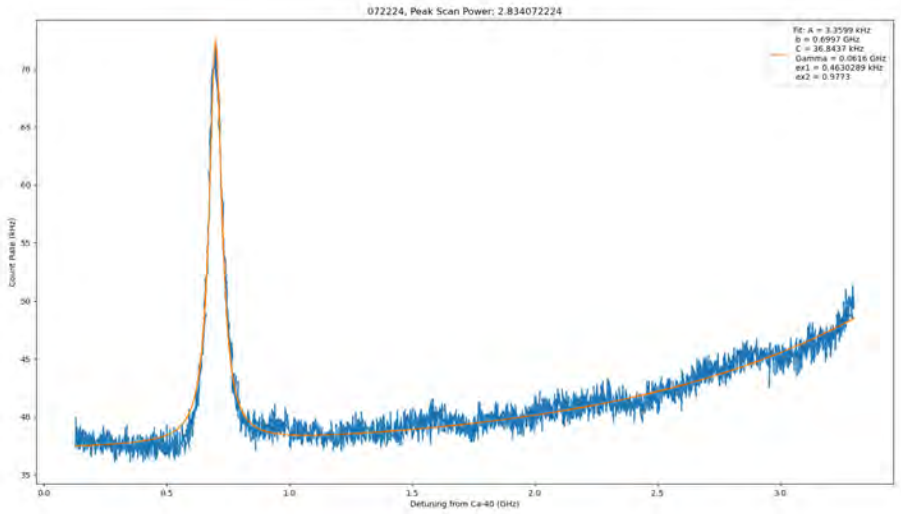

statistics, where for the count rate taken by

$$f = \frac{N}{\Delta T} \tag{7.9}$$

The uncertainty was found by

$$\sigma_F = \frac{\sqrt{N}}{\Delta T} \tag{7.10}$$

The other method was to take the standard deviation of the first 50 data points in a count file, where the count rate was assumed to be flat. The defined background counts would look like this:

with a histogram that looks like this:

By taking the standard deviation of these points, a reasonable expression for the variation in the counts due to statistics can be derived. This analysis performed on the 07/22/2024

Figure 7.18: Data Points Associated with Background

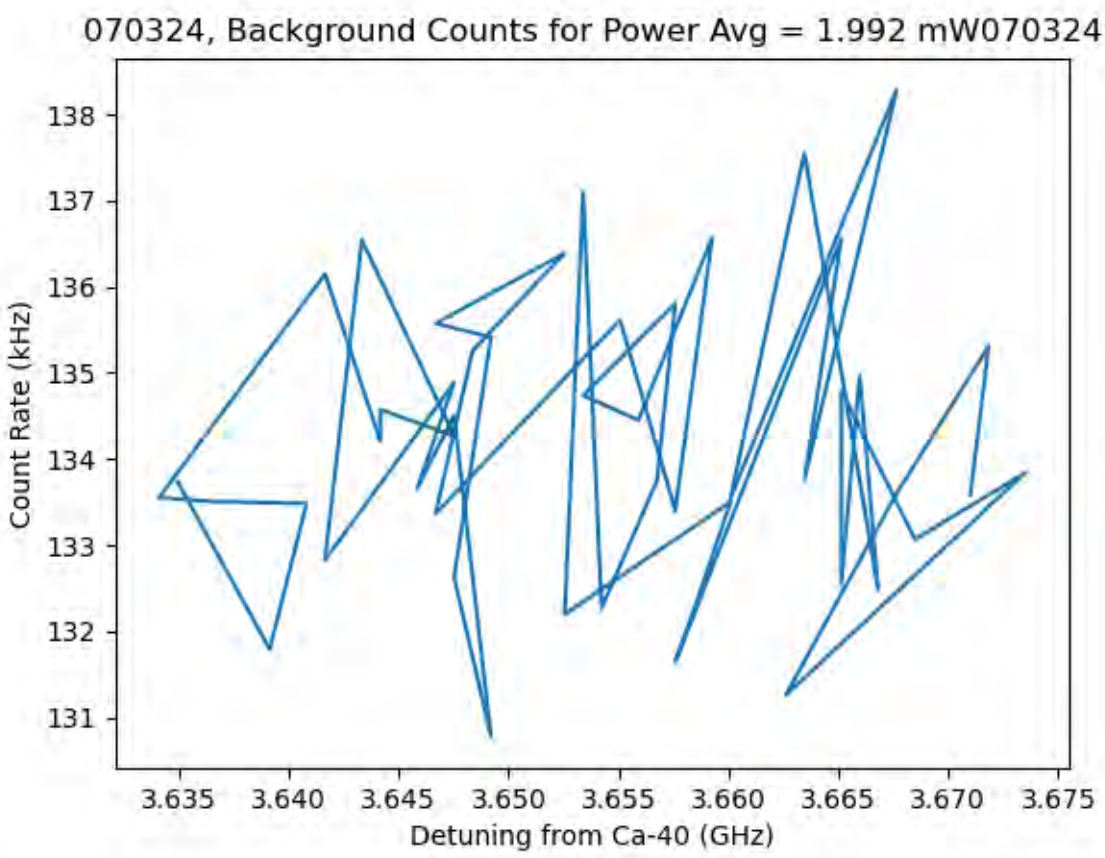

Figure 7.19: Histogram Associated with Background

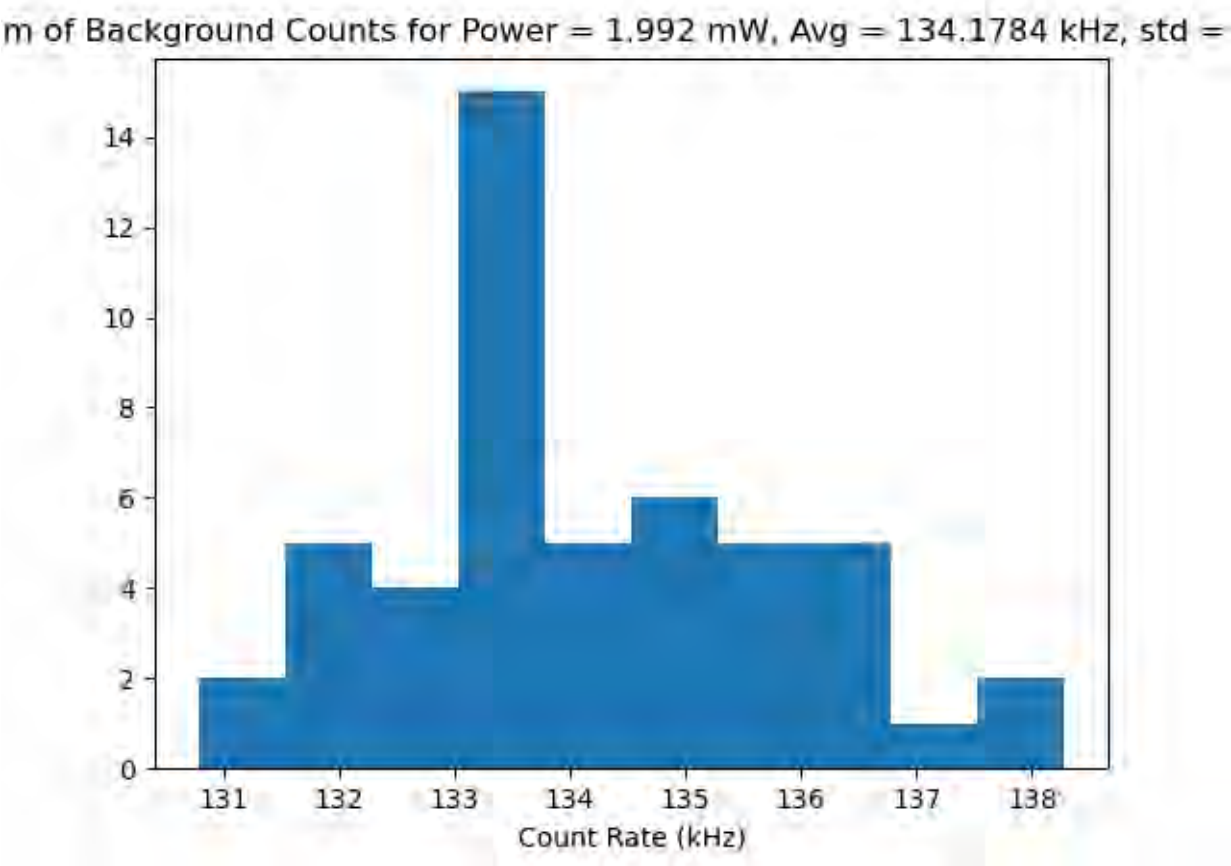

Figure 7.20: Fit to Area Versus Average Laser Power

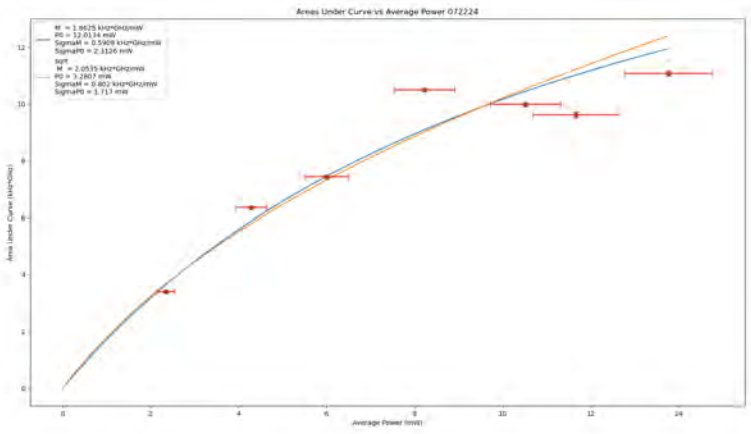

data looked like:

In addition to the uncertainties for the individual count rate points, the error in the power readings had to be accounted for. Not only did each individual power data point have uncertainty, which was necessary to know for the fit to exponential data for the count rate exponential decay parameter, but there also had to be some kind of quantization to account for the variation in overall power during the scan. For fitting the power to the exponential, the uncertainty in the data was characterized by taking the overall standard deviation of the laser power data set. As for characterizing the power for each scan, there were two ways to do this: one was to simply to take the mean and standard deviation of the laser power as the power level, and the associated uncertainty, as shown in the previous plot. The other way was to find the power at the frequency where the the peak height was found to be, use that as the power for the curve, and take the standard deviation of the 50 data points around it to use as an uncertainty. The resulting plots looked like this:

With two methods of determining the uncertainty of the count rates, and two methods of defining the power of the scan, this resulted in 4 different plots to analyze, the fourth of

Figure 7.21: Fit to Area Versus Peak Laser Power

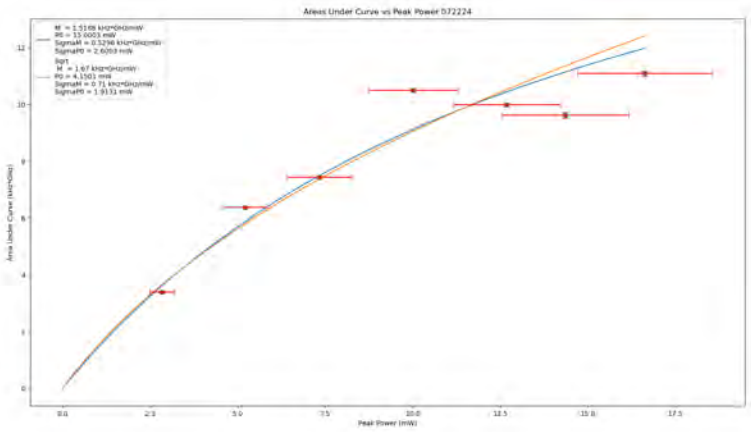

which for 07/22/2024 is shown here:

Figure 7.22: Poisson Fit to Area Versus Peak Laser Power

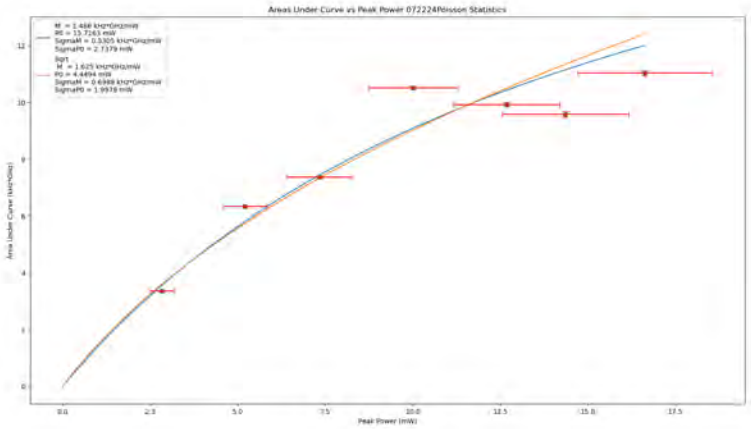

7.5.5 Results of Background Study

For each scan, the background could be parameterized from this analysis. Ideally, the background counts should be linear with the power of the laser. The background counts can be parameterized by using the constant background offset C, with the uncertainty being that

of the total background, found by the formula:

$$\sigma_{Background} = \sqrt{\sigma_C^2 + \sigma_D^2 e^{2B\omega_p} + \sigma_B^2 D^2 \omega_p^2 e^{2B\omega_p}} \tag{7.11}$$

where B, C, and D are the parameters from the equation from $f_{Background}(\omega)$ and ω_p is the frequency of the laser at the peak height. The background parameters C with this error were plotted as a function of peak power, and linear fits taken. They looked like:

Figure 7.23: Background Counts Plotted Versus Power at Signal Height on 07/22/2024

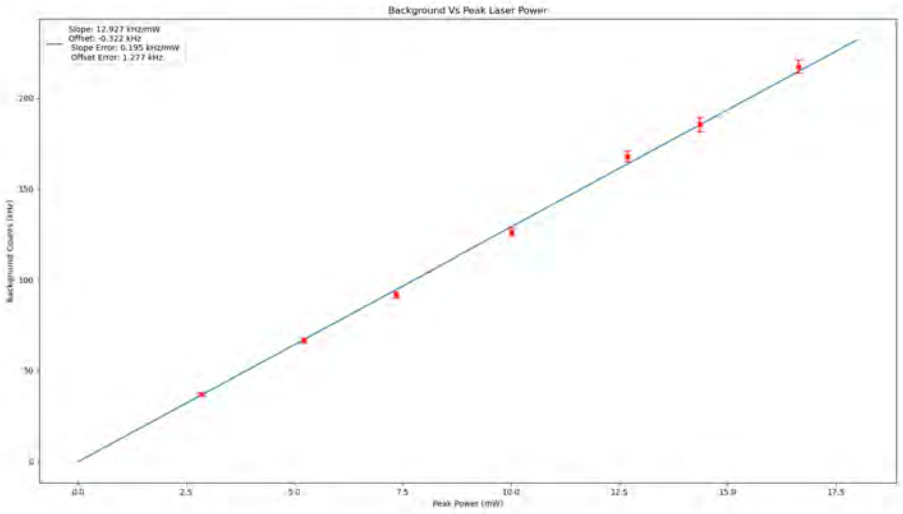

Seven studies of the background were taken, two of them dedicated signal scans with the oven off. The background and uncertainty of the background scans was parameterized by simply taking the mean and standard deviation of the data taken. A plot was made of the linear slopes of these 7 studies:

To compare these studies, it's important to remember that the oven temperature should have no effect on the background. The study done on 05/02/2024 was done with an obstruction that likely caused a large amount of extra light to scatter throughout the 6-way

Date	Oven Temp	Background Slope	Setup	Blackout Tape Installed
-	C	kHz/mW	-	y/n
05/02/2024	457	1170 ± 40	setup 1	n
05/10/2024	Room Temp	465.4 ± 2.7	setup 2	n
05/10/2024	380	449.4 ± 24.8	setup 2	n
07/03/2024	Room Temp	93.28 ± .85	setup 3	y
07/03/2024	457	29.6 ± 3.9	setup 4	y
07/08/2024	338	49.07 ± .25	setup 4	y
07/22/2024	338	12.93 ± .20	setup 5	y

cross. This gives an explanation as to why it was so much higher than all the other slopes. The two studies done on 05/10/2024 are very well in agreement with each other. Once the blackout tape was installed, the background counts went down significantly. The first scan done on 07/03/2024 was done with setup 3, and was misaligned through the 6-way cross. This could have caused internal reflections that increased the background, since the laser wasn't straight going through. It was realigned for setup 4, and the background slope went down significantly. There was a slight increase between 07/03/2024 and 07/08/2024 - This is harder to explain, though it could simply be that the optics shifted around somewhat. Finally, for setup 5 on 07/22/2024, the laser was more tightly focused going through the 6-way cross, and it resulted in the lowest background slope that was seen. It can be concluded that the blackout tape had a significant effect, reducing the background slope by an order of magnitude. It also is clear that alignment of the laser through the 6-way cross has a definite effect as well. It should also be noted that, on 05/10/2024, the background slope was reproducable when everything was kept the same.

7.5.6 Dependence of Area on Scan Rate

For these studies, the scan rate parameter used was either 2 or 5 MHz/s. Since the analysis technique finds the area under the count rate curve with respect to wavelength, and not time, the scan rate should not have any observable effect. However, on a scan from 07/03/2024, 3 scans were taken at 5 MHz/s, but another scan taken at 2 MHz/s gave a point that seemed very much like on outlier for the data. When added to the data taken at 5 MHz/s, the following plot can be made:

Figure 7.24: Data from 07/03/2024 with 2 MHz/s Scan Rate Area Plotted

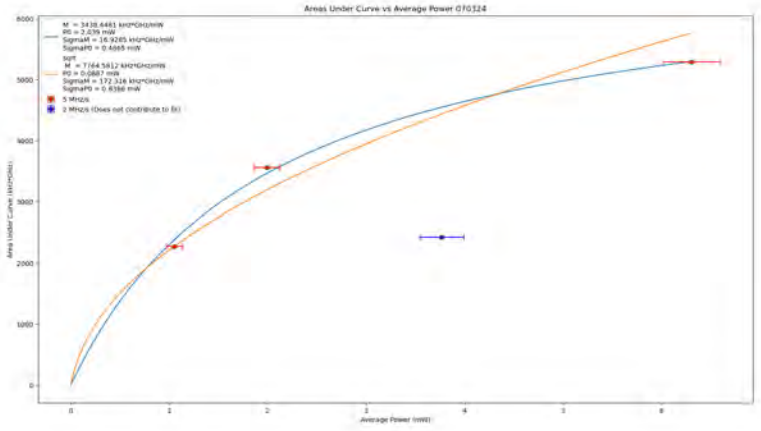

The area of the curve done at 2 MHz/s, shown in blue, seems like a significant outlier. The other evidence for there being some dependence on scan rate can be seen in the difference in low power slopes from the studies on 05/02/2024 and 07/03/2024:

Table 7.14

Date	Temperature	Laser Beam Profile	Scan Rate	Low Power Slope
-	C	-	MHz/s	GHz · kHz / mW
05/02/2024	457	setup 1	2	785.3 ± 64.6
07/03/2024	457	setup 4	5	3503 ± 365

The main difference was an obstruction present in setup 1 that was not present in setup 4, which should have an effect on the background but not the signal. The other was the scan rate. Further study should be made to see if this scan rate does or does not play a part in the signal size.

7.5.7 Area Vs. Power Analysis

The dependence of area under the curve, for low power, is essentially linear. As the power increases, the area get saturated, and the curve flattens. In order to perform this analysis, the signal areas versus powers were fitted to two different functions. The first was:

$$A(P) = M\frac{P}{1+\frac{P}{P_0}} \tag{7.12}$$

and the second:

$$A(P) = M\frac{P}{\sqrt{1+\frac{P}{P_0}}} \tag{7.13}$$

The fitting made sure to account for the uncertainties in both X and Y. The scipy.ODR package was used for the fitting, which is essentially a python wrapper for a FORTRAN code known as ODRPACK. The general idea behind the code can be found in [55]

7.5.8 Results

Overall, the fit to the $M\frac{P}{1+\frac{P}{P_0}}$ function worked much better. For each study performed, a table such as below was made:

The tables for all 5 studies are in the appendix. The parameter M was the parameter

Table 7.15: Fitting Results for 07/22/2024 Data

07/22/2024	m, Fit to $\frac{mP}{1+\frac{P}{P0}}$	m, Fit to $\frac{mP}{\sqrt{1+\frac{P}{P0}}}$
-	GHz · kHz / mW	GHz · kHz / mW
Averaged Power, Flat Statistics	1.863 ± .591	2.054 ± .802
Peak Power, Flat Statistics	1.519 ± .530	1.670 ± .710
Averaged Power, Poisson Statistics	1.822 ± .592	1.998 ± .789
Peak Power, Poisson Statistics	1.486 ± .531	1.625 ± .699

which determined the low-power slope. This was important to characterize, so that it could be compared to simulation. The m_0 and P_0 parameters are the initital guesses for the ODR fit. To get an idea of the systematic uncertainty for the M parameter, the standard deviation of the 4 different analysis measurements was taken. The resulting systematic uncertainty is reported in the summary table. This value of M, combined with simulated values of M dependent on atomic flux, would allow us to derive a reasonable estimate for our total atomic flux.

7.6 Simulation

Getting a value for atomic flux from fluorescence signal is not simple. This is because the relationship is extremely geometrically dependent. At a basic level, the relationship between atomic flux and low power slope looks something like:

$$M = G \cdot \Phi \tag{7.14}$$

where G is a linear geometric factor. Simulation is required to determine this geometric factor.

7.6.1 Single Atom Fluorescence Rate

The necessity of a computer for this simulation is due to the complicated nature of the region of fluorescence. At each point in space, there is a spatially-dependent atomic flux, atomic velocity, laser intensity, and solid angle for photon detection

The fluorescence works by exciting the calcium atoms from the ground state to the excited state. To calculate the single-atom fluorescence rate, one has to account for spontaneous emission, absorption, and stimulated emission. A simple two-level system is used.

Spontaneous emission occurs when an atom in the excited state decays back to the ground state, without the aid of lasers. Consider a group of atoms with a ground population fraction a(t) and an excited state population fraction b(t). The rate of change due to this can be described by:

$$\frac{da}{dt} = \frac{db}{dt} = Ab(t) \tag{7.15}$$

where A is the Einstein A coefficient for the state.

Absorption occurs when an atom absorbs a photon, say from a laser, and reaches an excited state. The rate of absorption depends on the laser power. It can be described by the function:

$$R(\mathbf{r}, \nu_\gamma) = \int_0^\infty \phi(\nu, \nu_\gamma, FWHM, \mathbf{r})\sigma(\nu)d\nu \tag{7.16}$$

where $\phi(\nu, \mathbf{r})$ is the number of photons per unit area, per time, per frequency, and

$$\sigma(\nu) = (\frac{h\nu}{c})B_a L(\nu) \tag{7.17}$$

is the absorption cross section. This is dependent on the Einstein absorption B-coefficient

$$B_a = \frac{c^3}{8\pi h\nu^3}\frac{g_b}{g_a}A = \frac{g_b}{g_a}B_b \tag{7.18}$$

where g_b and g_a are the number of degenerate levels states a and b, equivalent to 2J+1. The function $L(\nu)$ is described by:

$$L(\nu) = \frac{1}{2\pi}\frac{\frac{A}{2\pi}}{(\nu-\nu_a)^2 + \frac{A^2}{16\pi^2}} \tag{7.19}$$

where ν_a is the frequency of the atomic transition.

As for $\phi(\nu, \mathbf{r})$, the function can be split into an expression:

$$\phi(\nu, \nu_\gamma, FWHM, \mathbf{r}) = \frac{P_\gamma}{h\nu}\mathbf{S}(\mathbf{r}) \times \mathbf{G}(\nu, \nu_\gamma, FWHM) \tag{7.20}$$

where $\mathbf{S}(\mathbf{r})$ is the normalized fraction of photons per unit area, and $\mathbf{G}(\nu, \nu_\gamma, FWHM)$ is the normalized fraction of photons per unit frequency.

A gaussian beam is assumed, and the distribution of frequencies within the laser is assumed to have a gaussian distribution. Thus,

$$\mathbf{S}(\mathbf{r}) = \frac{I(\mathbf{r})}{P_\gamma} = \frac{2}{\pi w^2(z)}e^{-\frac{2\rho^2}{w^2(z)}} \tag{7.21}$$

where P_γ is the laser power, $w(z)$ is the beam radius at position z along the laser beam, ρ is the radial distance from $\mathbf{r}$ to the laser beam, and $I(\mathbf{r})$ is the laser beam intensity at position $\mathbf{r}$.

As for the frequency distribution,

$$\mathbf{G}(\nu, \nu_\gamma, FWHM) = \frac{2\sqrt{ln(2)/\pi}}{FWHM} e^{-rln(2)\frac{(\nu-\nu_\gamma)^2}{FWHM^2}} \tag{7.22}$$

where ν_γ is the set laser frequency, and FWHM is the Full-Width Half-Max of the laser frequency distribution.

In the region where the power is low - as in, where the linear nature of the low power slope dominates - the single atom fluorescence rate is roughly equivalent to the excitation rate.

7.6.2 Doppler Broadening

In addition to the geometric factor caused by the shape of the beam profile, there is an additional geometric factor caused by the angular distribution of atoms coming out of the nozzle.

Atoms moving with a transverse velocity component to the laser will see the laser frequency ν either red shifted or blue shifted by

$$\nu_a = \nu(1 - cos(\alpha)\frac{v}{c}) \tag{7.23}$$

where v is the velocity coming out of the nozzle, and α is the angle of the atom coming out of the oven with respect to an atom coming out straight. It can be characterized by

$$cos(\alpha) = \frac{\mathbf{r} \cdot \hat{\mathbf{x}}}{||\mathbf{r}||} \tag{7.24}$$

Thus, the position of the atom matters not only for the laser intensity at a given position, but also for the direction of travel for an atom at a given position. Furthermore, the

magnitude of the velocity also matters - an atom moving with a higher velocity will see a greater frequency shift at a given position. The velocity distribution of the atoms coming out of the oven is assumed to follow a maxwell-boltzmann distribution:

$$g(v) = \sqrt{\frac{2}{\pi}}(\frac{m}{k_b T})^{3/2} v^2 e^{-(\frac{v}{v_p})^2} \tag{7.25}$$

where

$$v_p = \sqrt{\frac{2k_b T}{m}} \tag{7.26}$$

This has to be characterized in the single-atom fluorescence rate by a new modification to the integral:

$$R(\nu_\gamma, \nu_a, \mathbf{r}) = \int_0^\infty \int_0^\infty \phi(\nu, \nu_\gamma, FWHM, \mathbf{r}) \sigma_D(\nu, \nu_a, \mathbf{r}) g(v) d\nu dv \tag{7.27}$$

7.6.3 Atomic Flux Dependence on Position

The last positional dependence that has to be integrated over is the atomic flux, with has an angular distribution out of the nozzle. The nozzle can be characterized by:

$$\gamma = \frac{2a}{L} \tag{7.28}$$

where a is the nozzle radius, and L is the nozzle length. The angular dependence out of the nozzle is also affected by collisions between the atoms in the nozzle. The Knudsen number, K_{nL}, is used to characterize the density of atoms[56]

$$K_{nL} = \frac{\lambda}{l} \tag{7.29}$$

where λ is the mean free path of atoms in the channel, and l is a typical distance traveled by the atoms between bounces off the nozzle. The value of this parameter determine if the flow is in the "molecular flow" regime, or if atomic collisions become significant. The nozzle used for our ABF studies was 83 mm in length, and 2mm in diameter. This resulted in a ratio of

$$\gamma = .0241 \tag{7.30}$$

For $\gamma << 1$, as is the case here, the Knudsen number can be expressed by:

$$K_{nL} = \frac{\lambda}{2a} \tag{7.31}$$

where a is the radius of the nozzle. The mean free path of the atoms - the average distance between each atom - can be described by:

$$\lambda = \frac{\sigma}{n} \tag{7.32}$$

where σ is the cross section of interaction, and n is the number density of the atoms inside the nozzle. The cross section σ is crudely modeled using the hard sphere approximation, where the atoms are imagined as simply hard spheres of a given radius. The cross section for such an interaction is

$$\pi r_{VDW} \tag{7.33}$$

where r_{VDW} is the Van Der Walls radius of the atom. As for the number density, it can be found with the ideal gas law:

$$PV = n_m RT \tag{7.34}$$

where P is the pressure, V is the volume, n_m is the number of moles, R is the ideal gas constant, and T is the temperature. The number density can thus be found:

$$n = \frac{N}{V} = \frac{n_m A_v}{V} = \frac{P A_v}{RT} \tag{7.35}$$

where A_v is Avagadro's number. The number density n is thus dependent on the pressure and temperature. The pressure itself is dependent upon the temperature and the substance being used. The vapor pressure of the substance is used as the value for P, for which the empirical formula is like:

$$P(T) = 10^{5.006 + A + \frac{B}{T} + C log_{10}(T) + \frac{D}{T^3}} [\text{Pa}] \tag{7.36}$$

with the coefficients A, B, C, and D dependent on the substance. This makes the Knudsen number K_n dependent upon 5 parameters for each substance, a table of some of which are below:

Element	A	B	C	D	r_{VDW}	Sources
-	-	K	-	K^3	pm	-
Ca	10.127	-9517	-1.403	0	231	[57], [58]
Ba	4.007	-8163	0	0	268	[57], [58]
Yb	9.111	-8111	-1.0849	0	175 (empirical)	[57], [59]

A plot can then be made of the Knudsen number as a function of temperature for different

elements:

Figure 7.25: Knudsen Number as Function of Tempereature

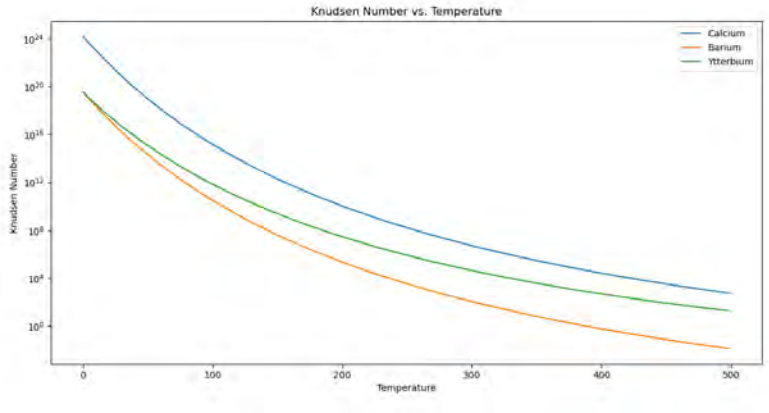

The molecular flow regime can be roughly considered when $K_{nL} > 10$. As can be seen, the curve for Calcium is well above 10 for temperatures between 0 and 500 C. This means collisions between the atoms can be assumed negligible. The atomic flux as a function of time can be described by the formula:

$$\Phi_a(\mathbf{r}) = \frac{dN_a}{dt}\frac{j(\theta)}{r^2} \tag{7.37}$$

where $j(\theta)$ is the angular distribution, r^2 the magnitude squared from the nozzle output, and

$$\frac{dN_a}{dt} = \frac{n_0 v_a a^2}{4} \tag{7.38}$$

where n_0 is the number density, the same one used to determine the Knudsen number, v_a is the velocity along the z direction, and a is the nozzle radius. The only thing left undefined for the atomic flux is the angular distribution $j(\theta)$.

In the molecular flow regime, the angular distribution equation can be described by the

following parameters:

$$p = \frac{\tan\theta}{\gamma} \tag{7.39}$$

$$R(p) = \cos^{-1}(p) - p\sqrt{1-p^2} \tag{7.40}$$

$$\zeta_0 = \frac{1}{2} - \frac{1}{3\gamma^2}\frac{1-2\gamma^3+(2\gamma^2-1)\sqrt{1+\gamma^2}}{\sqrt{1+\gamma^2}-\gamma^2\sinh^{-1}(1/\gamma)} \tag{7.41}$$

$$\zeta_1 = 1 - \zeta_0 \tag{7.42}$$

where γ is the nozzle parameter, ζ_0 is the channel exit collision parameter and ζ_1 is the channel entrance collision parameter. With these equations, the angular distribution can be described by:

$$j_{p\leq 1}(\theta) = \zeta_0 cos\theta + \frac{2}{\pi}\cos\theta((1-\zeta_0)R(p) + \frac{2}{3}(\zeta_1-\zeta_0)\frac{\cos^2\theta}{\sin\theta}) \tag{7.43}$$

and

$$j_{p\geq 1}(\theta) = \zeta_0\cos\theta + \frac{4\gamma}{3\pi}(\zeta_1-\zeta_0)\frac{\cos^2\theta}{\sin\theta} \tag{7.44}$$

Armed with these equations, the value of $\Phi_a(\mathbf{r})$ as a function of position can be modeled for Calcium.

7.6.4 Total Flux from Single Atom Fluorescence Rate

By integrating over the relevant positions in a volume, the geometric factor between the fluorescence counts and the fluorescence spectrum can be derived. The incident power on a photodetector for a given laser frequency can be expressed as:

$$P_d^q(\nu_\gamma) = \int\int h\nu_\gamma \frac{\Phi_a(\mathbf{r})}{v_a} F^q(\nu_\gamma, \mathbf{r}) dV_a \frac{dA_d}{4\pi|\mathbf{d}-\mathbf{r}|^2} \tag{7.45}$$

where q is an index representing the light polarization, $F(\nu_\gamma, \mathbf{r})$ is the single atom fluorescence rate, $\mathbf{d}$ is the position of the center of the photodetector surface, v_a is the velocity component of the atoms in the z direction, and $\Phi_a(\mathbf{r})$ is the atomic flux. The integral is over V_a, the volume of the interaction region, and dA_d, the area of the photodetector. This integral can be better made sense of by looking at it piece by piece:

$$h\nu_\gamma$$

is the energy of the photons being fluoresced

$$\frac{\Phi_a(\mathbf{r})}{v_a}$$

is the volumetric density of the atoms at a position

$$F(\nu_\gamma, \mathbf{r})$$

is the number of photons scattered per atom at a given position, and

$$\int \frac{dA_d}{4\pi|\mathbf{d}-\mathbf{r}|^2}$$

is the fraction of the fluoresced photons that actually hit the detector from a given position.

by multiplying these together, what is derived is:

$$\frac{\text{Energy}}{\text{Photon}} \times \frac{\text{Atoms}}{\text{Volume}} \times \frac{\text{Photons}}{\text{Atom}} \times \frac{\text{DetectorArea}}{\text{SphereSurfaceArea}} = \frac{\text{Energy}}{\text{Volume}}$$

Then, once integrated over the volume, the expression is derived for the total energy fluoresced onto a detector for a given frequency.

To simplify the integral, the assumption is made that the distance from each position in the interaction region to the detector follows the simple formula:

$$\int \frac{dA_d}{4\pi|\mathbf{d}-\mathbf{r}|^2} = \frac{A_d}{4\pi|\mathbf{d}-\mathbf{r}|^2} \tag{7.46}$$

The assumption is also made that the laser light is unpolarized. Once this integral is complete, it outputs data that can be converted back into number of photons, by dividing by the energy of each individual photon, $E_\gamma = h\nu$. By integrating over this, a simulated integrated count rate over a scan can be derived. The last step is to account for the efficiency of the detector, and the fraction of photons that make it through the filter. The specifications for the Thorlabs SPDMA and Edmund Optics 422 nm filter are used. We use a value of 25% detection efficiency for the SPDMA, which is halfway between the maximum and minimum efficiencies of the detector at 422 nm, depending on the gain setting.

In the future, careful calibration will be needed to determine more precisely the efficiency

Figure 7.26: Results of Simulation

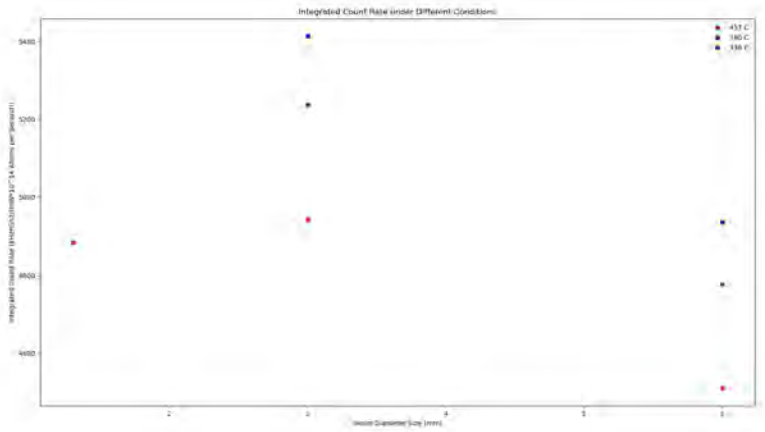

of the SPDMA. As for the 422 nm filter, the efficiency chosen was chosen to be 89.4%. With these values, it is easy to convert from the photons incident on the photodetector to the actual counts measured:

$$\text{CountsMeasured} = (.894)(.25)\text{IncidentPhotons} \tag{7.47}$$

7.6.5 Simulation Results

These simulations were done under a wide variety of conditions. Specifically, the temperature was varied, to see if it had any effect on the count rate per milliwatt. In addition, the diameter of the beam was varied. The count was integrated under different conditions of temperature and beam size, and the following plot was made of the results:

The simulated data is reported here:

Table 7.16: Simulated Integrated Area for Various Settings

Simulated Oven Temperature	Simulated Beam Diameter	Simulated Integrated Area
C	mm	$\frac{kHz \times GHz}{mW \times 10^{14} \text{AtomsperSecond}}$
338	3	5413.4
338	6	4937.9
380	3	5237.0
380	6	4777.0
457	1.3	4884.3
457	3	4942.8
457	6	4510.7

7.7 Analysis of Atomic Flux

With the measured data taken, and the simulated relation between low power slope and total atomic flux in hand, a value could be derived for the atomic flux as a function of temperature. In order to gauge the reliability of this value, it had to be compared to a simple model for the atomic flux coming out of the oven.

7.7.1 Simple Model for Predicting Atomic Flux out of Oven for Metallic Calcium

A simple model of total atomic flux versus temperature could be made using the formula (7.38). This requires the number density, area of the nozzle, and integral over the speed of the atoms. It can be written:

$$\frac{dN_a}{dt}(T) = \frac{a^2}{4}\frac{PA_v}{RT}\int_0^\infty g(v,T)v dv \tag{7.48}$$

where a is the nozzle radius, P is the vapor pressure calculated previously, A_v is Avagadros number, R is the ideal gas constant, T is the temperature in Kelvin, and

$$g(v,T) = \sqrt{\frac{2}{\pi}}(\frac{m}{k_b T})^{3/2} v^2 e^{-(\frac{v}{v_p})^2} \tag{7.49}$$

is the Maxwell-Boltzmann distribution. Armed with this model, a value for the atomic flux can be predicted from a given oven temperature T. The atomic flux as a function of the temperature looks like:

Figure 7.27: Simple Model of Atomic Flux from Oven Temperature

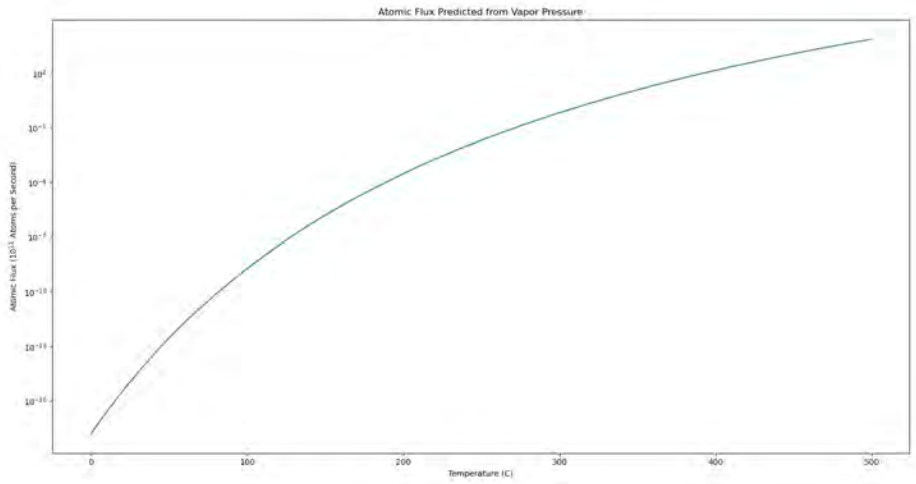

It can now be compared to the data that was taken.

7.7.2 Atomic Flux Calculated from Measurement and Simulation

Once again, the low power slope measured from fluorescence scans can be compared to the atomic flux by the equation:

$$M = G \times \Phi$$

where G is a geometric factor determined by simulation. To compare the fluorescence

study to the simple model, all the low power slopes from the study were considered. There were 2 measurements for 338 C, 1 measurement for 380 C, and 2 measurements for 457 C. This resulted in 5 measurements. After this, there were different scaling factors, dependent upon the temperature and beam size. There were 3 scaling factors for 457 C, 2 scaling factors for 380 C, and 2 scaling factors for 338 C.Each measurement had every scaling factor applied to it. This corresponded to 4 atomic flux data points for 338 C, 2 for 380 C, and 6 for 457 C. The uncertainty in the low power slope was also converted to atomic flux, using the same scaling factor. The resulting data points can be seen in the following table:

Table 7.17: Measured Atomic Flux Data

Temperature	Atomic Flux	Uncertainty
C	10^{11} Atoms per Second	10^{11} Atoms per Second
338	.350	.019
338	.384	.021
338	.309	.032
338	.339	.035
380	18.346	.561
380	20.113	.615
457	160.780	13.226
457	158.878	13.070
457	174.097	14.322
457	717.196	74.729
457	708.708	73.845
457	776.598	80.919

This was plotted versus the vapor pressure model curve:

This plot used the statistical uncertainties scaled in the same way as the atomic flux. In order to collapse all the data points into a single measurement, the average of the data at each temperature was taken, as well as the standard deviation. The average was used as a single data point for the temperature, and the standard deviation as the systematic uncertainty. The following plot was made, with the averaged data point, as well as the max-

Figure 7.28: Predicted Vs. Measured Atomic Flux

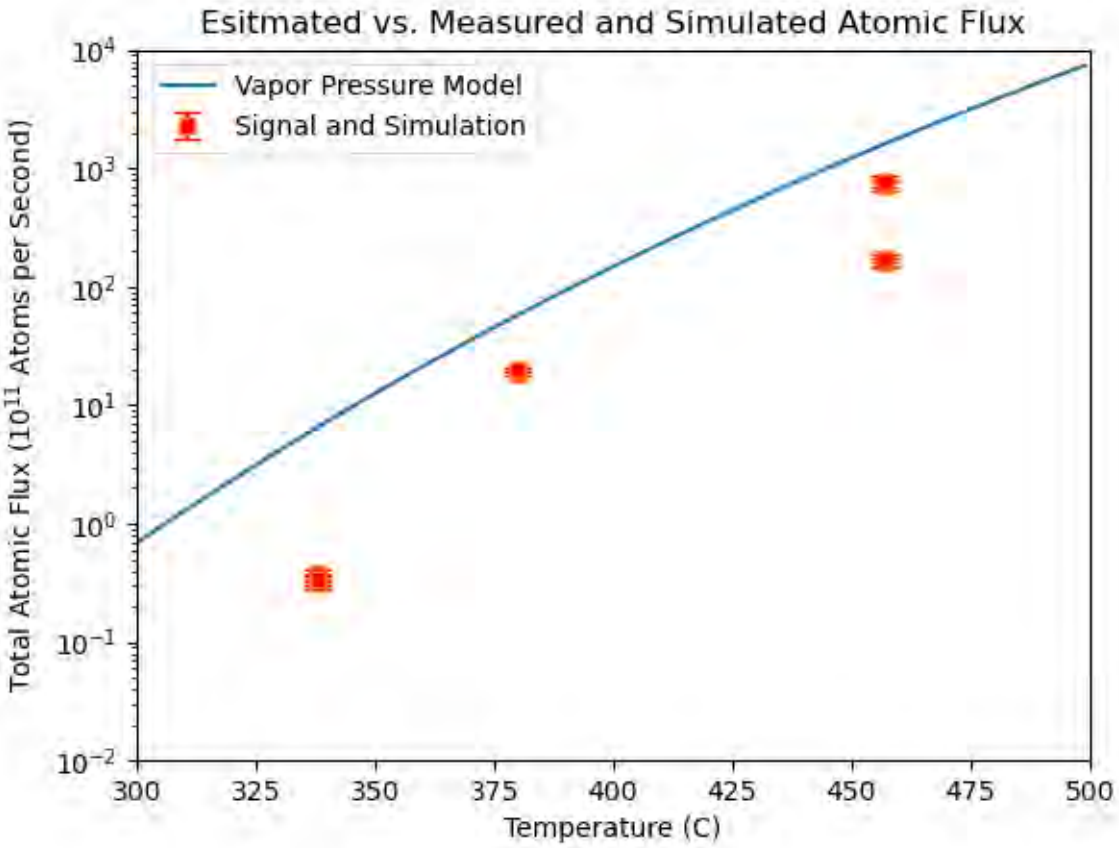

imum uncertainty from either the systematic uncertainty or any of the individual statistical uncertainties:

Figure 7.29: Predicted Vs. Measured Atomic Flux with Maximum Uncertainty

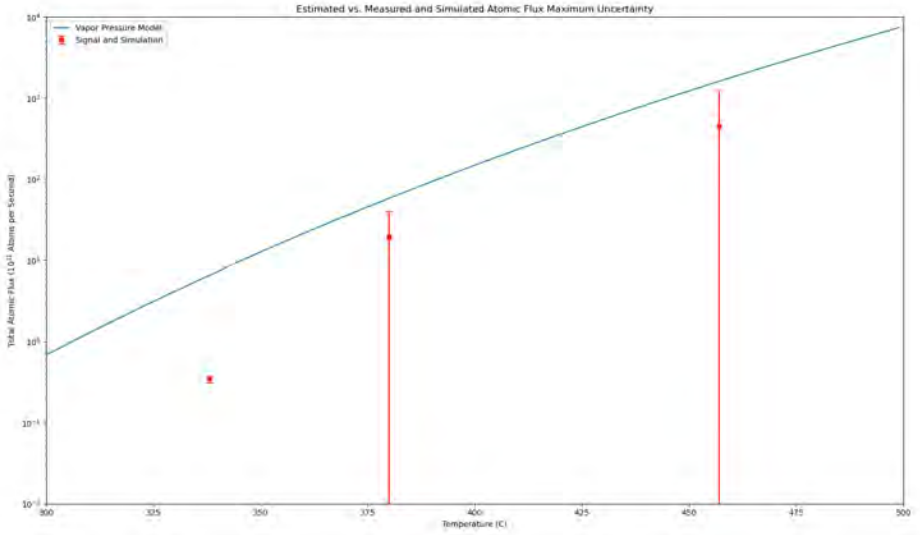

The residuals are given below:

7.7.3 Comparison of Atomic Flux Measurements with Vapor Pressure Prediction

A table of the data points, the maximum uncertainty, and the number of sigma away from the predicted total atomic flux are below:

Table 7.18: Final Measurement Data Points

Temperature	Predicted Atomic Flux	Measured Atomic Flux	# of σ Away from Predicted Atomic Flux
C	10^{11} Atoms per Second	10^{11} Atoms per Second	-
338	6.542	.345 $\pm$ .035	-178.9
380	57.826	19.230 $\pm$ 20.113	-1.92
457	1609.300	449.376 $\pm$ 776.598	-1.45

Figure 7.30: Predicted Vs. Measured Atomic Flux with Maximum Uncertainty Residuals

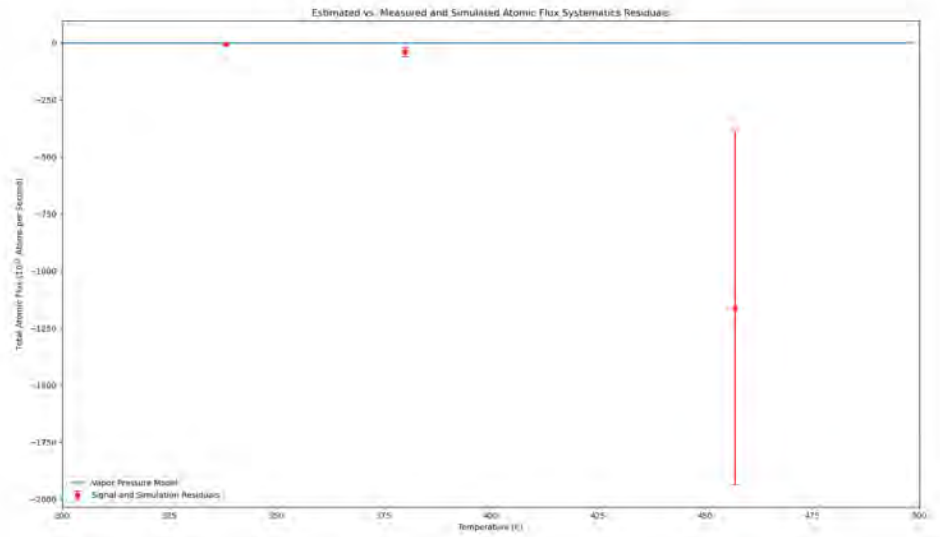

All of the data points fell below the prediction made with the vapor pressure. This suggests that the simple vapor pressure model overestimated the number of atoms coming out of the oven. This is a good sign, since ideally the sensitivity in our oven should be maximized, to better characterize the atomic flux of various chemical processes. The biggest uncertainty came from the 457 C measurements. This was due to the fact that of the two studies done at this temperature, two quite different values for the low power slope were measured. There were significant changes between these two measurements, however. Not only was black acktar tape installed between these measurements, but the laser had to be realigned between the two studies, meaning that the laser alignment was not exactly in the same place. Finally, the scans were done at two different scan rates. While theory indicates that this should not have changed the area, there is evidence to suggest that this does have a slight effect. Ultimately, the 457 and 380 C studies were within two sigma of the vapor pressure curve, making this not particularly significant for determining whether the

vapor pressure curve is a good approximation. The 338 C data point, however, is extremely significant. It is over 100σ away from the predicted value - very much an outlier. In addition, this point is the result of two separate studies - the only difference between the two being the swap between setups 4 and 5. To account for uncertainty in the beam size, two different scaling factors were applied to each of the low power slopes derived from the studies. These scaling factors were different, in that the simulated beam size was chosen to be different. The variation due to the differences in scaling factors and measured low power slopes was characterized by taking the systematic uncertainty of the resulting atomic fluxes, and the uncertainty seen is the maximum uncertainty, either systematic or statistical, associated with any of the data points. The fact that this uncertainty is still so small, and the difference in prediction and measurement so large, suggests there is something going on here. Perhaps, as the atomic flux gets lower, the vapor pressure approximation begins to break down. Whatever the case, it seems that the lowest atomic flux that was measured was $\approx 3 \times 10^{10}$ atoms per second, at a temperature where it was predicted to have $\approx 6 \times 10^{11}$ atoms per second. This is encouraging, since the sensitivity goal of the apparatus is to measure atomic flux on the order of 10^8 atoms per second. It now needs to be seen whether this atomic flux is possible at the moment.

7.7.4 Characterizing Atomic Flux Sensitivity

Getting an idea of the smallest atomic flux measurable by the apparatus requires comparing the fluorescence count rate uncertainty - in essence, the noise from the background - with the signal area. To do this, the gamma parameter from the Lorentzian was taken. The signal area associated with background noise was considered as a Lorentzian, of the same Γ width parameter, with a maximum height equal to the fluorescence count rate uncertainty σ. The

equation to get the area from these two parameters is:

$$\frac{\pi}{2}\Gamma\sigma = A \tag{7.50}$$

A table of the relevant data from the scans is below:

Table 7.19: Area Associated with Uncertainty in Count Rate for Scans at 338 C

Date of Scan	Count Rate Uncertainty	Lorentzian Fit Gamma	Uncertainty Area	Average Power	Average Power Uncertainty
07/08/2024	2.63	0.066	0.273	4.84	.056
07/08/2024	2.06	0.073	0.236	3.88	.022
07/08/2024	1.37	0.054	0.116	1.98	.016
07/08/2024	0.93	0.067	0.098	1.07	.020
07/08/2024	2.79	0.078	0.342	7.04	.052
07/22/2024	1.77	0.077	0.214	13.76	1.00
07/22/2024	1.70	0.072	0.192	11.66	.98
07/22/2024	2.11	0.077	0.255	10.52	.80
07/22/2024	1.39	0.085	0.186	8.22	.69
07/22/2024	1.02	0.071	0.114	6.00	.50
07/22/2024	0.97	0.073	0.111	4.82	.35
07/22/2024	0.76	0.063	0.075	2.34	.19

From there, since the background noise should increase linearly with the power, a linear fit can be done to a plot of the average powers with their uncertainties, versus the associated signal area. For the scans on 07/08/2024 and 07/22/2024, the plots looks like:

Note the swapping of the X and Y axes, this is to take advantage of the uncertainties associated with the power into the fit. By taking the reciprocal of the slope, the actual slope of $\frac{GHz \times kHz}{mW}$ can be found.

Table 7.20: Slopes Associated with Background Uncertainties

Date	Raw Slope	Slope Reciprocal
-	$\frac{mW}{GHz \times kHz}$	$\frac{GHz \times kHz}{mW}$
07/08/2024	20.37	.049
07/22/2024	58.84	.017

from there, each of the two slope reciprocals can be multiplied by one of the geometric factors, to determine the atomic flux associated with a background measurement:

Figure 7.31: Linear Fit to Background Areas from 07/08/2024

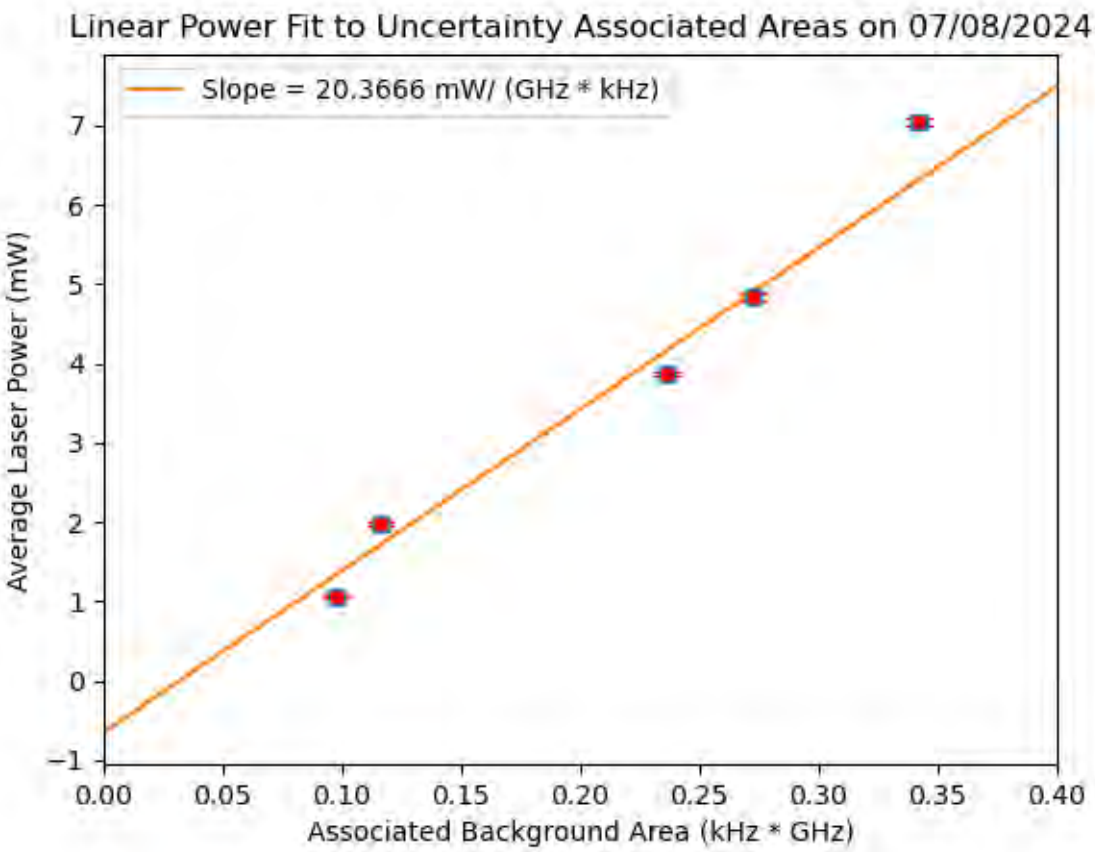

Figure 7.32: Linear Fit to Background Areas from 07/22/2024

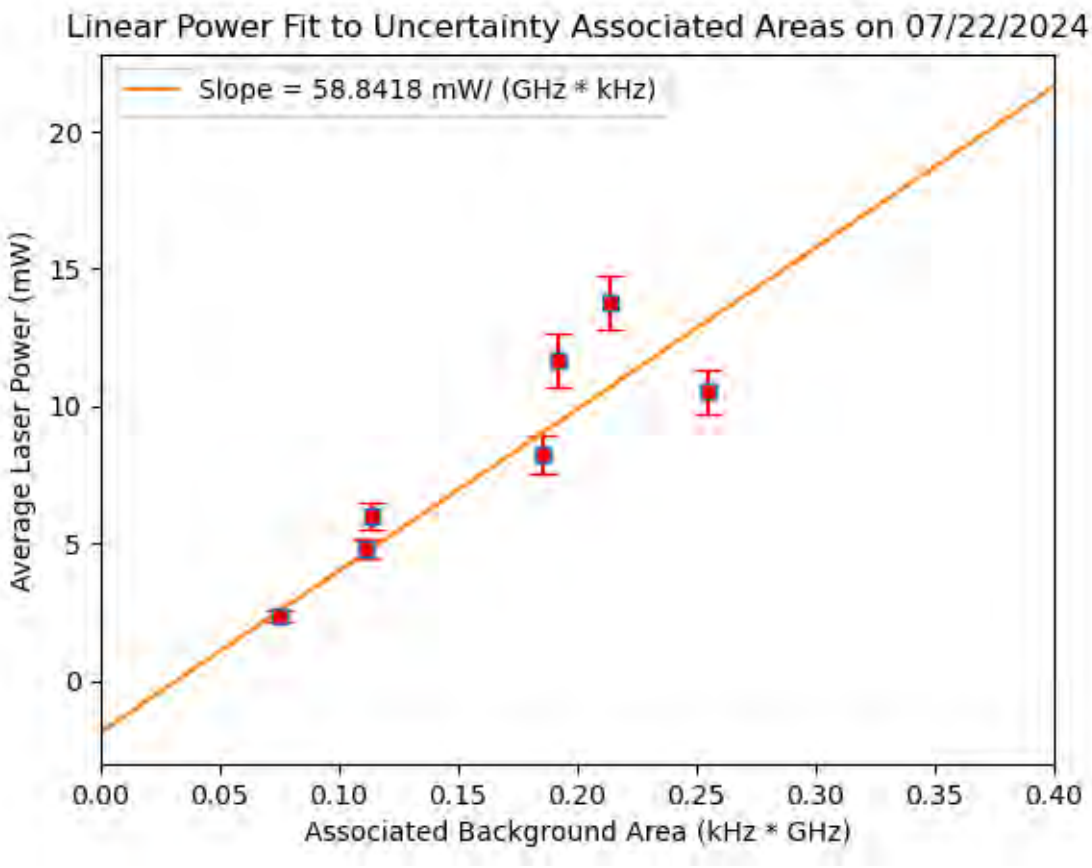

Table 7.21: Slopes Associated with Background Uncertainties

Background Power Slope $\frac{GHz \times kHz}{mW}$	Geometric Factor $\frac{kHz \times GHz}{mW \times 10^{11}\text{AtomsperSecond}}$	Atomic Flux $10^{11}\text{AtomsperSecond}$
.049	5.4134	.00905
.049	4.9379	.00992
.017	5.4134	.00314
.017	4.9379	.00344

Taking the maximum value of these, it appears that the signal associated with the background noise is 9.92×10^8 atoms per second - multiplying by a factor of 5, so that the area of the signal is clearly visible versus the background, the minimum signal currently observable is something like:

$$\Phi_{min} \approx 5 \times 10^9 \text{AtomsPerSecond}$$

In order to reach the goal of 10^8 atom per second sensitivity, a further order of magnitude in background reduction is needed. Methods with which this might be realized are now discussed.

7.8 Future Improvements

To reach the desired atomic flux of 10^8 atoms per second, another order of magnitude of sensitivity improvement is needed. This can be achieved mainly through background reduction. The maximum signal sensitivity analysis used, of the two studies at 338 C, the one with the maximum noise associated. It can be seen from the background study that by simply using a more focused beam, the background was reduced by a factor of 4. By utilizing a single-mode fiber, the beam intensity profile could be better controlled, and kept

constant. This would aid in the reproducibility of studies, and likely allow for even smaller beam profiles to be used. It can be seen from the analysis of the previous section that the tighter beam resulted in an improvement of sensitivity by a factor of 3. It is also true that laser stability issues were observed towards the end of these studies. Repairing the laser, specifically the Lighthouse Photonics Sprout pump laser, might reduce the exponential drift in power seen during the scans, which was especially profound in the scans on 07/22/2024. Finally, if further sensitivity is needed, the installation of a lens on the inside of the 6-way cross would increase the fluorescence signal seen, though it would make the simulation more complicated to run.

Chapter 8. Conclusion

8.1 Overview

Permanent EDM searches serve as a clean way to probe unknown sources of CP violation in the universe. EDM searches on diamagnetic atoms in particular are sensitive to CP violation in the hadronic sector. Radium-225 is particularly sensitive to new physics in this sector, due to the octopole deformation in its nucleus. This atom is a radioactive rare isotope, and procuring it has been difficult. For this reason, substituting it with Radium-223 was attempted, and efforts are ongoing to test the efficiency of various ways of making an atomic beam harvested from the FRIB. Once in an atomic beam, the Radium atoms are laser cooled and trapped, and transported to in between a pair of electrodes for a spin precession measurement. This measurement forms the basis of the EDM measurement, and its sensitivity is directly proportional to the electric field applied. The statistical sensitivity of the experiment also heavily relies on the electric field being perfectly reversible in polarity. For this reason, efforts are also ongoing to increase electric field strength, while also making it more reversible.

I started my graduate career in research working at MSU on conditioning electrodes to accept higher electric fields with low discharge rates. I then moved to Argonne National Laboratory, where I became acquainted with laser cooling and trapping Radium-226. It was here that I became very comfortable working with lasers, including their maintenance and repair. At the time, Radium-223 was proposed as an interim substitute for Radium-225. For this to work, previously unknown energy levels for this isotope would have to be measured.

I managed to fluoresce the primary trapping transition while in a beam, though efforts were unsucessful at fully trapping Radium-223 in the oven load, and the supply of Radium-223 was cut shortly thereafter.

With the skills I'd developed at ANL in hand, I moved back to MSU to setup the apparatus for efficiency measurements of isotopes harvested from MSU's radioactive beam dump. This involved having a custom effusive oven fabricated in a machine shop, and then assembling an apparatus for beam fluorescence. I also had to get the lasers in the lab working again, after they were in a state of disrepair following the COVID lockdowns. This was done with the expertise I gained at ANL, as well as with new skills I had to acquire, such as writing custom software to allow two incompatible laser elements to talk to each other. I also had to write the software necessary for the experiment to run, develop procedures for loading the oven, and debug the system when it was going wrong.

Using this apparatus, I was able to fluoresce a beam of metallic Calcium. I then performed spectroscopic studies to determine that the lowest atomic flux able to be measured with the system is 5×10^9 atoms per second. This information will aid in future studies of isotope beam production, in order to ensure radium flows out of our oven as efficiently as possible.

In addition, I assisted with designing and testing the components necessary for a new HV swiching system. This system aims to use a unipolar 60 kV power supply to not only achieve higher voltages, but also improve field reversiblity through a system of mechanical relays. I selected the power supply to use, as well as the mechanical relays and solid state relay to use. I also did preliminary designs for the HV cage, planned out how to use hardware logic for safety, and assembled an HV divider that will enable measurement of the applied voltages to verify the same voltage to 1 part per million, rather than 7000 parts per million.

In order to get a better idea as to the effect of these upgrades, I performed calculations

to determine the size of systematic errors in the experiment. I was able to successfully reproduce a known calculation for the vector shift due to holding ODT power for Cesium-133, and began work to adapt this code to Mercury-199 as well. Once this code is working, adapting it to Radium should be quite easy, due to the similar electronic structure.

These upgrades will assist with the plan to improve the sensitivity of the RaEDM experiment from 1.4E-23 e cm to a measurement on the order of 1E-26 e cm. Previous data runs utilized an applied E field of $\pm$6.7kV/mm. Electrodes conditioned at MSU were able to reach field strengths of 20 kV/mm with minimal discharges. With the new HV apparatus being assembled at MSU, continued electrode conditioning should hopefully allow for electrodes to be conditioned to up to 50 kV/mm. Such an improvement in E field strength would on its own result in an order of magnitude sensitivity improvement in this EDM search. In addition, the 3 order of magnitude improvement in the sensitivity should reduce the systematic uncertainty in turn. The ABF apparatus built at MSU will open up the ability to test various forms of Radium for use in our experiment, and optimize the efficiency with which we are able to use Radium harvested from the FRIB beam dump. Being able to finally use Radium-225 again will allow the experiment to actually continue. Furthermore, additional upgrades ongoing at ANL, such as the Blue Slower Upgrade and Quantum Non-Demoltion, will further increase sensitivity. Many of the necessary transitions for the upgraded optical cycling scheme have been fluoresced, and once in place, this upgrade should improve the amount of atoms measured 60 fold. With the Quantum Non-Demolition, thousands of times more atoms should be able to be scattered during the shadow imaging measurement, improving the clarity of the image. These elements together will all contribute to a new sensitivity of 1E-26 e cm.

BIBLIOGRAPHY

[1] B. Graner, Y. Chen, E. G. Lindahl, and B. R. Heckel, "Reduced limit on the permanent electric dipole moment of ^{199}Hg," *Phys. Rev. Lett.*, vol. 116, p. 161601, Apr 2016.

[2] B.-N. Lu, J. Zhao, Z. En-Guang, and S.-G. Zhou, "Potential energy surfaces of actinide and transfermium nuclei from multi-dimensional constraint covariant density functional theories," *EPJ Web of Conferences*, vol. 38, 03 2013.

[3] S. K. Lamoreaux and E. N. Fortson, "Calculation of a linear Stark effect on the 254-nm line of Hg," *Physical Review A*, vol. 46, no. 11, pp. 7053–7059, 1992.

[4] T. A. Zheng, Y. A. Yang, S.-Z. Wang, J. T. Singh, Z.-X. Xiong, T. Xia, and Z.-T. Lu, "Measurement of the electric dipole moment of ^{171}Yb atoms in an optical dipole trap," *Phys. Rev. Lett.*, vol. 129, p. 083001, Aug 2022.

[5] K. Kehagia, C. Potiriadis, S. Bratakos, V. Koukouliou, and G. Drikos, "Determination of 226ra in urine samples by alpha spectrometry," *Radiation Protection Dosimetry*, vol. 127, pp. 293–296, 09 2007.

[6] M. Alfred, "An overview of targeted alpha therapy with ¡sup¿225¡/sup¿actinium and ¡sup¿213¡/sup¿bismuth," *Current Radiopharmaceuticals*, vol. 11, no. 3, pp. 200–208, 2018.

[7] A. A. Penzias and R. W. Wilson, "A Measurement of Excess Antenna Temperature at 4080 Mc/s.," , vol. 142, pp. 419–421, July 1965.

[8] R. H. Dicke, P. J. E. Peebles, P. G. Roll, and D. T. Wilkinson, "Cosmic Black-Body Radiation.," , vol. 142, pp. 414–419, July 1965.

[9] R. H. Cyburt, B. D. Fields, K. A. Olive, and T.-H. Yeh, "Big bang nucleosynthesis: Present status," *Reviews of Modern Physics*, vol. 88, Feb. 2016.

[10] N. Aghanim, Y. Akrami, M. Ashdown, J. Aumont, C. Baccigalupi, M. Ballardini, A. J. Banday, R. B. Barreiro, N. Bartolo, S. Basak, R. Battye, K. Benabed, J.-P. Bernard, M. Bersanelli, P. Bielewicz, J. J. Bock, J. R. Bond, J. Borrill, F. R. Bouchet, F. Boulanger, M. Bucher, C. Burigana, R. C. Butler, E. Calabrese, J.-F. Cardoso, J. Carron, A. Challinor, H. C. Chiang, J. Chluba, L. P. L. Colombo, C. Combet, D. Contreras, B. P. Crill, F. Cuttaia, P. de Bernardis, G. de Zotti, J. Delabrouille, J.-M. Delouis, E. Di Valentino, J. M. Diego, O. Dor, M. Douspis, A. Ducout, X. Dupac, S. Dusini, G. Efstathiou, F. Elsner, T. A. Enlin, H. K. Eriksen, Y. Fantaye, M. Farhang, J. Fergusson, R. Fernandez-Cobos, F. Finelli, F. Forastieri, M. Frailis, A. A. Fraisse, E. Franceschi, A. Frolov, S. Galeotta, S. Galli, K. Ganga, R. T. Gnova-Santos, M. Gerbino, T. Ghosh, J. Gonzlez-Nuevo, K. M. Grski, S. Gratton, A. Gruppuso, J. E. Gudmundsson, J. Hamann, W. Handley, F. K. Hansen, D. Herranz, S. R.

Hildebrandt, E. Hivon, Z. Huang, A. H. Jaffe, W. C. Jones, A. Karakci, E. Keihnen, R. Keskitalo, K. Kiiveri, J. Kim, T. S. Kisner, L. Knox, N. Krachmalnicoff, M. Kunz, H. Kurki-Suonio, G. Lagache, J.-M. Lamarre, A. Lasenby, M. Lattanzi, C. R. Lawrence, M. Le Jeune, P. Lemos, J. Lesgourgues, F. Levrier, A. Lewis, M. Liguori, P. B. Lilje, M. Lilley, V. Lindholm, M. Lpez-Caniego, P. M. Lubin, Y.-Z. Ma, J. F. Macas-Prez, G. Maggio, D. Maino, N. Mandolesi, A. Mangilli, A. Marcos-Caballero, M. Maris, P. G. Martin, M. Martinelli, E. Martnez-Gonzlez, S. Matarrese, N. Mauri, J. D. McEwen, P. R. Meinhold, A. Melchiorri, A. Mennella, M. Migliaccio, M. Millea, S. Mitra, M.-A. Miville-Deschnes, D. Molinari, L. Montier, G. Morgante, A. Moss, P. Natoli, H. U. Nrgaard-Nielsen, L. Pagano, D. Paoletti, B. Partridge, G. Patanchon, H. V. Peiris, F. Perrotta, V. Pettorino, F. Piacentini, L. Polastri, G. Polenta, J.-L. Puget, J. P. Rachen, M. Reinecke, M. Remazeilles, A. Renzi, G. Rocha, C. Rosset, G. Roudier, J. A. Rubio-Martn, B. Ruiz-Granados, L. Salvati, M. Sandri, M. Savelainen, D. Scott, E. P. S. Shellard, C. Sirignano, G. Sirri, L. D. Spencer, R. Sunyaev, A.-S. Suur-Uski, J. A. Tauber, D. Tavagnacco, M. Tenti, L. Toffolatti, M. Tomasi, T. Trombetti, L. Valenziano, J. Valiviita, B. Van Tent, L. Vibert, P. Vielva, F. Villa, N. Vittorio, B. D. Wandelt, I. K. Wehus, M. White, S. D. M. White, A. Zacchei, and A. Zonca, "Planck2018 results: Vi. cosmological parameters," *Astronomy amp; Astrophysics*, vol. 641, p. A6, Sept. 2020.

[11] R. Jora, "Baryon asymmetry in the standard model revisited," 2018.

[12] L. Landau, "On the conservation laws for weak interactions," *Nuclear Physics*, vol. 3, no. 1, pp. 127–131, 1957.

[13] J. H. Christenson, J. W. Cronin, V. L. Fitch, and R. Turlay, "Evidence for the 2π decay of the k_2^0 meson," *Phys. Rev. Lett.*, vol. 13, pp. 138–140, Jul 1964.

[14] T. D. Lee and C. N. Yang, "Question of parity conservation in weak interactions," *Phys. Rev.*, vol. 104, pp. 254–258, Oct 1956.

[15] C. S. Wu, E. Ambler, R. W. Hayward, D. D. Hoppes, and R. P. Hudson, "Experimental test of parity conservation in beta decay," *Phys. Rev.*, vol. 105, pp. 1413–1415, Feb 1957.

[16] R. L. Garwin, L. M. Lederman, and M. Weinrich, "Observations of the Failure of Conservation of Parity and Charge Conjugation in Meson Decays: the Magnetic Moment of the Free Muon," *Physical Review*, vol. 105, no. 4, pp. 1415–1417, 1957.

[17] L. I. Schiff, "Measurability of nuclear electric dipole moments," *Phys. Rev.*, vol. 132, pp. 2194–2200, Dec 1963.

[18] V. V. Flambaum and J. S. M. Ginges, "The nuclear Schiff moment and time invariance violation in atoms," *arXiv*, 2001.

[19] V. Spevak, N. Auerbach, and V. V. Flambaum, "Enhanced T-odd, P-odd electromagnetic moments in reflection asymmetric nuclei," *Physical Review C*, vol. 56, no. 3, pp. 1357–1369, 1997.

[20] T. Chupp and M. Ramsey-Musolf, "Electric Dipole Moments: A Global Analysis," *arXiv*, 2014.

[21] T. S. Roussy, L. Caldwell, T. Wright, W. B. Cairncross, Y. Shagam, K. B. Ng, N. Schlossberger, S. Y. Park, A. Wang, J. Ye, and E. A. Cornell, "An improved bound on the electrons electric dipole moment," *Science*, vol. 381, no. 6653, pp. 46–50, 2023.

[22] V. Andreev, D. G. Ang, D. DeMille, J. M. Doyle, G. Gabrielse, J. Haefner, N. R. Hutzler, Z. Lasner, C. Meisenhelder, B. R. OLeary, C. D. Panda, A. D. West, E. P. West, and X. Wu, "Improved limit on the electric dipole moment of the electron," *Nature*, vol. 562, no. 7727, pp. 355–360, 2018.

[23] C. Abel, S. Afach, N. J. Ayres, C. A. Baker, G. Ban, G. Bison, K. Bodek, V. Bondar, M. Burghoff, E. Chanel, Z. Chowdhuri, P.-J. Chiu, B. Clement, C. B. Crawford, M. Daum, S. Emmenegger, L. Ferraris-Bouchez, M. Fertl, P. Flaux, B. Franke, A. Fratangelo, P. Geltenbort, K. Green, W. C. Griffith, M. van der Grinten, Z. D. Grujić, P. G. Harris, L. Hayen, W. Heil, R. Henneck, V. Hélaine, N. Hild, Z. Hodge, M. Horras, P. Iaydjiev, S. N. Ivanov, M. Kasprzak, Y. Kermaidic, K. Kirch, A. Knecht, P. Knowles, H.-C. Koch, P. A. Koss, S. Komposch, A. Kozela, A. Kraft, J. Krempel, M. Kuźniak, B. Lauss, T. Lefort, Y. Lemière, A. Leredde, P. Mohanmurthy, A. Mtchedlishvili, M. Musgrave, O. Naviliat-Cuncic, D. Pais, F. M. Piegsa, E. Pierre, G. Pignol, C. Plonka-Spehr, P. N. Prashanth, G. Quéméner, M. Rawlik, D. Rebreyend, I. Rienäcker, D. Ries, S. Roccia, G. Rogel, D. Rozpedzik, A. Schnabel, P. Schmidt-Wellenburg, N. Severijns, D. Shiers, R. Tavakoli Dinani, J. A. Thorne, R. Virot, J. Voigt, A. Weis, E. Wursten, G. Wyszynski, J. Zejma, J. Zenner, and G. Zsigmond, "Measurement of the permanent electric dipole moment of the neutron," *Phys. Rev. Lett.*, vol. 124, p. 081803, Feb 2020.

[24] D.-T. Wong, M. Hassan, J. Burdine, T. Chupp, S. Clayton, C. Cude-Woods, S. Currie, T. Ito, C.-Y. Liu, M. Makela, C. Morris, C. OShaughnessy, A. Reid, N. Sachdeva, and F. Uhrich, "Characterization of the new ultracold neutron beamline at the lanl ucn facility," *Nuclear Instruments and Methods in Physics Research Section A: Accelerators, Spectrometers, Detectors and Associated Equipment*, vol. 1050, p. 168105, May 2023.

[25] Y. A. Yang, T. A. Zheng, S.-Z. Wang, W.-K. Hu, C.-L. Zou, T. Xia, and Z.-T. Lu, "Quantum nondemolition measurement of the spin precession of laser-trapped ^{171}Yb atoms," *Phys. Rev. Appl.*, vol. 19, p. 054015, May 2023.

[26] T. Zheng, Y. Yang, S.-Z. Wang, J. Singh, Z.-X. Xiong, T. Xia, and Z.-T. Lu, "Measurement of the electric dipole moment of ^{171}yb atoms in an optical dipole trap," *Physical Review Letters*, vol. 129, Aug. 2022.

[27] F. Allmendinger, I. Engin, W. Heil, S. Karpuk, H.-J. Krause, B. Niederländer, A. Offenhäusser, M. Repetto, U. Schmidt, and S. Zimmer, "Measurement of the permanent electric dipole moment of the ^{129}Xe atom," *Phys. Rev. A*, vol. 100, p. 022505, Aug 2019.

[28] D. Cho, K. Sangster, and E. A. Hinds, "Search for time-reversal-symmetry violation in thallium fluoride using a jet source," *Phys. Rev. A*, vol. 44, pp. 2783–2799, Sep 1991.

[29] O. Grasdijk, O. Timgren, J. Kastelic, T. Wright, S. Lamoreaux, D. DeMille, K. Wenz, M. Aitken, T. Zelevinsky, T. Winick, and D. Kawall, "Centrex: a new search for time-reversal symmetry violation in the 205tl nucleus," *Quantum Science and Technology*, vol. 6, p. 044007, sep 2021.

[30] A. Sunaga, Y. Takahashi, A. Vutha, and Y. Takahashi, "Measuring the nuclear magnetic quadrupole moment of optically trapped ytterbium atoms in the metastable state," *New Journal of Physics*, vol. 26, p. 023023, feb 2024.

[31] D. DeMille, N. R. Hutzler, A. M. Rey, and T. Zelevinsky, "Quantum sensing and metrology for fundamental physics with molecules," *Nature Physics*, vol. 20, pp. 741–749, May 2024.

[32] P. A. Butler, "Pear-shaped atomic nuclei," *Proceedings of the Royal Society A: Mathematical, Physical and Engineering Sciences*, vol. 476, no. 2239, p. 20200202, 2020.

[33] N. Auerbach, V. V. Flambaum, and V. Spevak, "Collective t- and p-odd electromagnetic moments in nuclei with octupole deformations," *Phys. Rev. Lett.*, vol. 76, pp. 4316–4319, Jun 1996.

[34] J. Dobaczewski and J. Engel, "Nuclear Time-Reversal Violation and the Schiff Moment of Ra225," *Physical Review Letters*, vol. 94, no. 23, p. 232502, 2005.

[35] S. Ban, J. Dobaczewski, J. Engel, and A. Shukla, "Fully self-consistent calculations of nuclear Schiff moments," *Physical Review C*, vol. 82, no. 1, p. 015501, 2010.

[36] M. Bishof, R. H. Parker, K. G. Bailey, J. P. Greene, R. J. Holt, M. R. Kalita, W. Korsch, N. D. Lemke, Z.-T. Lu, P. Mueller, T. P. O'Connor, J. T. Singh, and M. R. Dietrich, "Improved limit on the ^{225}Ra electric dipole moment," *Phys. Rev. C*, vol. 94, p. 025501, Aug 2016.

[37] T. Rabga, *Upgrades for an Improved Measurement of the Permanent Electric Dipole Moment of Radium*. PhD thesis, 2020. Copyright - Database copyright ProQuest LLC; ProQuest does not claim copyright in the individual underlying works; Last updated - 2023-06-21.

[38] M. Kalita, M. Bishof, K. Bailey, M. Dietrich, J. Greene, R. Holt, W. Korsch, Z.-T. Lu, N. Lemke, P. Mueller, T. O'Connor, R. Parker, and J. Singh, "Search for a permanent electric dipole moment (edm) of ^{2}25$raatom,''$ 052015.

[39] R. H. Parker, M. R. Dietrich, M. R. Kalita, N. D. Lemke, K. G. Bailey, M. Bishof, J. P. Greene, R. J. Holt, W. Korsch, Z.-T. Lu, P. Mueller, T. P. O'Connor, and J. T. Singh, "First measurement of the atomic electric dipole moment of ^{225}Ra," *Phys. Rev. Lett.*, vol. 114, p. 233002, Jun 2015.

[40] N. D. Scielzo, J. R. Guest, E. C. Schulte, I. Ahmad, K. Bailey, D. L. Bowers, R. J. Holt, Z.-T. Lu, T. P. O'Connor, and D. H. Potterveld, "Measurement of the lifetimes of the lowest $^3p_1$ state of neutral ba and ra," *Phys. Rev. A*, vol. 73, p. 010501, Jan 2006.

[41] J. D. Jackson, *Classical electrodynamics*. New York, NY: Wiley, 3rd ed. ed., 1999.

[42] J. M. Pendlebury, W. Heil, Y. Sobolev, P. G. Harris, J. D. Richardson, R. J. Baskin, D. D. Doyle, P. Geltenbort, K. Green, M. G. D. van der Grinten, P. S. Iaydjiev, S. N. Ivanov, D. J. R. May, and K. F. Smith, "Geometric-phase-induced false electric dipole moment signals for particles in traps," *Phys. Rev. A*, vol. 70, p. 032102, Sep 2004.

[43] U. Dammalapati, K. Jungmann, and L. Willmann, "Compilation of Spectroscopic Data of Radium (Ra I and Ra II)," *Journal of Physical and Chemical Reference Data*, vol. 45, p. 013101, 02 2016.

[44] K. Wendt, S. A. Ahmad, W. Klempt, R. Neugart, E. W. Otten, and H. H. Stroke, "On the hyperfine structure and isotope shift of radium," *Zeitschrift fr Physik D Atoms, Molecules and Clusters*, vol. 4, no. 3, pp. 227–241, 1987.

[45] G. Breit and L. A. Wills, "Hyperfine Structure in Intermediate Coupling," *Physical Review*, vol. 44, no. 6, pp. 470–490, 1933.

[46] J. R. Guest, N. D. Scielzo, I. Ahmad, K. Bailey, J. P. Greene, R. J. Holt, Z.-T. Lu, T. P. OConnor, and D. H. Potterveld, "Laser Trapping of Ra225 and Ra226 with Repumping by Room-Temperature Blackbody Radiation," *Physical Review Letters*, vol. 98, no. 9, p. 093001, 2007.

[47] J. Biero, "Multiconfiguration dirachartreefock calculations of the hyperfine structures of radium," *Journal of Physics B: Atomic, Molecular and Optical Physics*, vol. 38, p. 2221, jun 2005.

[48] M. V. Romalis and E. N. Fortson, "Zeeman frequency shifts in an optical dipole trap used to search for an electric-dipole moment," *Phys. Rev. A*, vol. 59, pp. 4547–4558, Jun 1999.

[49] R. A. Ready, G. Arrowsmith-Kron, K. G. Bailey, D. Battaglia, M. Bishof, D. Coulter, M. R. Dietrich, R. Fang, B. Hanley, J. Huneau, S. Kennedy, P. Lalain, B. Loseth, K. McGee,

P. Mueller, T. P. OConnor, J. OKronley, A. Powers, T. Rabga, A. Sanchez, E. Schalk, D. Waldo, J. Wescott, and J. T. Singh, "Surface processing and discharge-conditioning of high voltage electrodes for the ra edm experiment," *Nuclear Instruments and Methods in Physics Research Section A: Accelerators, Spectrometers, Detectors and Associated Equipment*, vol. 1014, p. 165738, 2021.

[50] R. Ready, H. Li, S. Kofford, R. Kwapisz, H. Dan, A. Sawhney, M. Fan, C. Holliman, X. Shi, L. Sever-Walter, A. N. Gaiser, J. R. Griswold, and A. M. Jayich, "Laser cooling of radium-225 ions," 2024.

[51] E. P. Abel, K. Domnanich, H. K. Clause, C. Kalman, W. Walker, J. A. Shusterman, J. Greene, M. Gott, and G. W. Severin, "Production, collection, and purification of 47ca for the generation of 47sc through isotope harvesting at the national superconducting cyclotron laboratory," *ACS Omega*, vol. 5, no. 43, pp. 27864–27872, 2020. PMID: 33163769.

[52] E. P. Abel, K. Domnanich, H. K. Clause, C. Kalman, W. Walker, J. A. Shusterman, J. Greene, M. Gott, and G. W. Severin, "Production, collection, and purification of 47ca for the generation of 47sc through isotope harvesting at the national superconducting cyclotron laboratory," *ACS Omega*, vol. 5, no. 43, pp. 27864–27872, 2020. PMID: 33163769.

[53] E. J. Salumbides, V. Maslinskas, I. M. Dildar, A. L. Wolf, E.-J. van Duijn, K. S. E. Eikema, and W. Ubachs, "High-precision frequency measurement of the 423-nm ca i line," *Phys. Rev. A*, vol. 83, p. 012502, Jan 2011.

[54] W. Nrtershuser, N. Trautmann, K. Wendt, and B. Bushaw, "Isotope shifts and hyperfine structure in the 4s2 1s0 4s4p1p1 4s4d 1d2 transitions of stable calcium isotopes and calcium-41," *Spectrochimica Acta Part B: Atomic Spectroscopy*, vol. 53, no. 5, pp. 709–721, 1998.

[55] J. R. D. Paul T. Boggs, "Orthogonal distance regression," *NISTIR 89-4197*, December 1989.

[56] D. R. Olander and V. Kruger, "Molecular beam sources fabricated from multichannel arrays. iii. the exit density problem," *Journal of Applied Physics*, vol. 41, pp. 2769–2776, 06 1970.

[57] V. P. I. C. B. Alcock and M. K. Horrigan, "Vapour pressure equations for the metallic elements: 2982500k," *Canadian Metallurgical Quarterly*, vol. 23, no. 3, pp. 309–313, 1984.

[58] M. Mantina, A. C. Chamberlin, R. Valero, C. J. Cramer, and D. G. Truhlar, "Consistent van der waals radii for the whole main group," *The Journal of Physical Chemistry A*, vol. 113, no. 19, pp. 5806–5812, 2009. PMID: 19382751.

[59] J. C. Slater, "Atomic radii in crystals," *The Journal of Chemical Physics*, vol. 41, pp. 3199–3204, 11 1964.